8-2015

Europan double ridge morphology as a test for hypothesized models of formation

Ashley Caroline Dameron
University of Tennessee - Knoxville, adameron@vols.utk.edu

To the Graduate Council:

I am submitting herewith a thesis written by Ashley Caroline Dameron entitled "Europan double ridge morphology as a test for hypothesized models of formation." I have examined the final electronic copy of this thesis for form and content and recommend that it be accepted in partial fulfillment of the requirements for the degree of Master of Science, with a major in Geology.

Devon M. Burr, Major Professor

We have read this thesis and recommend its acceptance:

Joshua P. Emery, William M. Dunne

Accepted for the Council:
Dixie L. Thompson

Vice Provost and Dean of the Graduate School

(Original signatures are on file with official student records.)

Europan double ridge morphology as a test for hypothesized models of formation

A Thesis Presented for the
Master of Science
Degree
The University of Tennessee, Knoxville

Ashley Caroline Dameron
August 2015

Acknowledgements

I would like to first acknowledge my advisor, Devon Burr, for her willingness to investigate the morphology of Europa with me, and for all of her guidance and incredibly helpful feedback on this work. I also want to thank my committee members, Josh Emery and Bill Dunne, for all of their input and expertise. Thank you to my peers at UT; I've enjoyed my time with you immensely. A special thanks to Chloe Beddingfield for her guidance in learning how to make DEMs in ISIS as well. A big thank you to the incredibly helpful staff at the USGS/NASA Planetary Photogrammetry Guest Facility in Flagstaff: Annie Howington-Kraus, Bonnie Redding, and Raad Saleh. Learning how to use SOCET-SET was fun, and I was grateful to have your guidance in making my SOCET-SET DEMs for this work. Thanks to Rick Snyder, my high school Earth science teacher, for sparking my interest in planetary science by mentioning Europa in class one day, and for allowing me to do a science fair project focused on it. I want to thank all of my friends back home in Missouri for your support and friendship through the years. Finally, I would like to thank my family, especially my parents, my siblings, and my nephew Dawson for their love and support; I couldn't have done this without you!

Abstract

Double ridges on the Jovian satellite Europa consist of two ridges with a central trough. Several hypotheses exist describing their formation. Explosive cryovolcanism would result in granular ice depositing as two self-symmetric ridges flanking a central fracture, lying at or below the angle of repose (AOR). Cryo-sediments deposited by tidal squeezing and low-viscosity cryolavas emplaced by effusive cryovolcanism would likely have shallow slopes, although ridge symmetry is not expected. A second group of hypotheses involves brittle deformation of the crust, namely by diapirism, shear heating, and buckling of the lithosphere due to compression. Because these models involve uplifting vertical fractures, they are expected to result in interior slopes steeper than the AOR, with shallower exteriors. Thus, these formation hypotheses can be grouped into two classes based on expected interior slopes: cryo-sedimentary mechanisms (cryovolcanism, tidal squeezing), and brittle deformation mechanisms (diapirism, compression, shear heating), with symmetry providing a secondary constraint.

To assess the viability of these formation mechanisms, I measured double ridge slopes at multiple locations distributed across Europa through analysis of data from the Galileo Solid-State Imaging camera. Two types of data were used to derive slopes and slope symmetry for 44 double ridges: elevation data from 5 digital elevation models (DEMs) (4 ridges), and ridge shadow length measurements taken on images (40 ridges). DEM slope values in the Cilix and Banded Plains (15°S, 195°W) regions typically fall below the AOR, although values above the AOR occur along one ridge. Interior-exterior slope symmetry is dominant, which favors cryo-sedimentary mechanisms because double ridges created from brittle deformation would maintain slope asymmetry after post-emplacement modification (e.g. mass wasting). Two different shadow measurement techniques were implemented to calculate interior slopes, with one

technique accounting for a gap between ridge set interiors. These slopes are also below the AOR (42° maximum for the youngest ridges). Older ridges tend to have shallower slopes, which could possibly be attributed to mass wasting. Shallow interior slopes derived from both techniques suggest that double ridges form from cryo-sedimentary mechanisms. Symmetry of ridge interiors and exteriors may also suggest that explosive cryovolcanism is the dominant shape-forming mechanism.

Table of Contents

1. Introduction 1
2. Background 5
2.1 Hypothesized Formational Mechanisms for Double Ridges 5
2.1.1 Cryo-sedimentary Mechanisms 5
2.1.2 Brittle Deformation Mechanisms 9
2.1.3 Distinguishing Between Formation Hypotheses via Slope Angles, Symmetry 12
2.2 Double Ridge Degradation 13
2.3 Previous Work: Double ridge Morphometry 16
3. Hypotheses 20
3.1 Null Hypothesis 20
3.2 Alternative Hypothesis 20
4. Data and Methods 22
4.1 Galileo SSI Data 22
4.2 Shadow Measurements 23
4.2.1 Exterior Shadow Length Technique 23
4.2.2 Interior Shadow Length Technique 27
4.2.3 Site Selection 30
4.3 Creation of stereogrammetry DEMs in ISIS 3 using Ames Stereo Pipeline 31
4.3.1 Selection of Stereo-Pair Images 31
4.3.2 Processing in ISIS 3 32
4.4 Generating Stereogrammetry DEMs in SOCET-SET 34
4.4.1 Site Selection 34
4.4.2 Processing Steps 35
4.4.3 Analyzing DEMs in ArcMap 10.1 and Excel 38
4.4.4 Comparing ASP and SOCET-SET DEMs 39
4.4.5 Statistical Analyses of Data 39
5. Results 40
5.1 Digital Elevation Models 40
5.1.1 Banded Plains region: stereo pairs with 3800r.img (SOCET-SET and ASP) 40

5.1.2 Cilix region: stereo pairs with 5013r.img (SOCET-SET and ASP) 44
5.1.3 Slope Population Statistics 46
5.1.4 Summary of Results: 46
5.2 Shadow Measurements 47
5.2.1 Argadnel Regio 48
5.2.2 Bright Plains Region 48
5.2.3 Southern Annwyn Regio (5°N, 327°W) 49
5.2.4 Other Pwyllian Ridges 50
5.2.5. Summary of Results: 51
6. Discussion 52
6.1 Comparison of ASP and SOCET-SET DEMs 52
6.2 Supported Formation Mechanisms: Cryo-sedimentary Processes 54
6.3 Possible Formation Mechanisms within Banded Plains 57
6.4 Double Ridge Morphometry Over Time 59
6.5 Influence of Mass Wasting on Inferences of Formation Mechanisms 61
6.6 Presence of Gaps between Double Ridges 62
6.7 Implications for the Subsurface 64
7. Conclusions 67
References 69
Appendix 78
Vita 127

List of Tables

Table 1. Summary of previous findings on double ridge morphometry. 19
Table 2. Two groupings for previously proposed formational mechanisms. 21
Table 3. Comparison between the interior and exterior shadow length techniques. 30
Table 4. Results from all DEMs created with SOCET-SET and ASP..... 41
Table 5. Banded Plains 2828r.img SOCET-SET DEM slope values for 26 profile lines. 81
Table 6. Banded Plains 2832r.img SOCET-SET DEM slope values for 18 profile lines. 89
Table 7. Banded Plains 2825r.img SOCET-SET DEM slope values for nine profile lines. 93
Table 8. Cilix West 7442r.img SOCET-SET DEM slope values for 18 profile lines. 97
Table 9. Cilix East 7542r.img SOCET-SET DEM slope values for five profile lines. 104
Table 10. Results from t-tests between exterior and interior slopes derived from DEMs. 105
Table 11. Results from paired t-tests between interior and exterior slope pairs for each DEM. 105
Table 12. Results from interior and exterior shadow measurement techniques for each region. 126

List of Figures

Figure 1. Europan SSI image mosaic with study areas, inset of Androgeos Linea. 2
Figure 2. Double ridge formational mechanism diagram. 6
Figure 3. Simplified diagram of double ridge cross section. 7
Figure 4. Chart of interior angle of repose (AOR) vs. expected ridge symmetry..... 14
Figure 5. Cross-section and perspective view of double ridges showing variables used in calculation of interior slope from exterior shadow measurements. 24
Figure 6. Plan view sketches for exterior shadow length measurement corrections. 26
Figure 7. Illustration of measuring double ridge trend in GIMP for corrections..... 27
Figure 8. Cross-section view of double ridge showing variables used in calculation of interior slopes from interior shadow measurements, from Kadel et al. (1998). 28
Figure 9. SOCET-SET DEMs 2825r.img, 2828r.img, and 2832r.img (~16.0°S, 194°W). 79
Figure 10. Orthoimages and slope maps accompanying DEMs in Figure 9. 80
Figure 11. Histogram of slopes derived from the SOCET-SET 2828r.img DEM..... 84
Figure 12. Topographic profile lines for the double ridge in 2828r.img. 85
Figure 13. ASP DEM 2828r.img (~16.0°S, 194°W). 86
Figure 14. Histogram of slopes derived from the ASP 2828r.img DEM. 87
Figure 15. Distribution of overlapping slopes along trend for the SOCET-SET and ASP 2828r.img DEMs..... 88
Figure 16. Histogram of slopes derived from the SOCET-SET 2832r.img DEM..... 90
Figure 17. Topographic profile lines for the double ridge in 2832r.img. 91
Figure 18. Difference plot for double ridge in SOCET-SET DEMs 2828r.img and 2832r.img. . 92
Figure 19. Histogram of slopes derived from the SOCET-SET 2825r.img DEM..... 94
Figure 20. Topographic profile lines for the double ridge in 2825r.img. 95
Figure 21. SOCET-SET DEM 7442r.img in Cilix west (2.0°N, 184.0°W)..... 96
Figure 22. Histogram of slopes derived from the SOCET-SET 7442r.img DEM..... 98
Figure 23. ASP 7442r.img DEM in Cilix west (2.0°N, 184.0°W). 99
Figure 24. Distribution of overlapping slopes along trend for the SOCET-SET and ASP 7442r.img DEMs..... 100
Figure 25. ASP 7446r.img DEM in Cilix west (1.5°N, 183.0°W). 101

Figure 26. Histogram of slopes derived from ASP 7446r.img DEM. 102
Figure 27. SOCET-SET DEM 7542r.img in Cilix east (2.0°N, 182.0°W). 103
Figure 28. Histogram of all slopes derived from SOCET-SET and ASP DEMs. 104
Figure 29. Sixteen ridges located in Argadnel Regio. 106
Figure 30. Histogram of all interior and exterior shadow length technique slopes in Argadnel Regio. 107
Figure 31. Histograms of interior and exterior shadow length slopes classified by relative age for Argadnel Regio. 108
Figure 32. Box plot of slopes for three relative ages using interior and exterior shadow length techniques in Argadnel Regio. 109
Figure 33. Difference between interior and exterior shadow length technique slopes in Argadnel Regio for three age groupings. 110
Figure 34. 10 ridges located in Bright Plains Region. 111
Figure 35. Histograms of slopes derived from both interior and exterior shadow length techniques for the Bright Plains region. 112
Figure 36. Histograms of interior and exterior technique slopes classified by relative age for Bright Plains region. 113
Figure 37. Box plot of slopes for three relative ages using interior and exterior shadow length techniques in Bright Plains region.. 114
Figure 38. Difference between interior and exterior shadow length technique slopes in Bright Plains Region for three age groupings. 115
Figure 39. Five ridges located in southern Annwyn Regio. 116
Figure 40. Histogram of interior and exterior technique slopes classified by relative age in southern Annwyn Regio. 117
Figure 41. Box plot of slopes for two relative ages using interior and exterior shadow length techniques in southern Annwyn Regio. 118
Figure 42. Difference between interior and exterior shadow length technique slopes in southern Annwyn Regio for two age groupings. 119
Figure 43. Four Pwyllian ridges located in northern latitude region. 120
Figure 44. Five Pwyllian ridges located in southern latitude region. 121

Figure 45. Histograms of interior and exterior technique slopes for Pwyllian ridges in northern latitude regions. 122
Figure 46. Histograms of interior and exterior technique slopes for Pwyllian ridges in southern latitude regions. 123
Figure 47. Histograms of interior shadow length technique slopes for Pwyllian ridges in both northern and southern latitude regions 124
Figure 48. Difference between slopes derived from interior and exterior shadow length techniques in northern and southern latitude regions. 125
Figure 49. Overall distribution of Pwyllian slopes for both exterior and interior shadow length techniques. 126

1. Introduction

Double ridges are ubiquitous surface features on the Jovian satellite Europa (Lucchitta and Soderblom, 1982; Belton et al., 1996; Greeley et al., 1998). They exist at all latitudes and consist of two higher-elevation lineations on either side of a central trough (Figure 1). They are sometimes flanked by outer marginal troughs, and individual ridges may have unique textures along their interior and exterior slopes that can be either normal or parallel to ridge strike (Head et al., 1999). In some cases, the ridged background plains material appears to continue up the exterior flanks of newer double ridges (Head et al., 1999; Greenberg and Sak, 2014). Double ridges can be ~100-300 meters in height, up to a few kilometers wide, and extend for thousands of kilometers (Head et al., 1999; Dombard et al., 2013). Although double ridges are one of the most common linear features seen on Europa, our current understanding of double ridge morphology is incomplete. For example, characteristics such as interior and exterior slopes have been quantified, but these values differ between studies, affecting determination of the cause of double ridge initiation and development (Kadel et al., 1998; Bader et al., 2008; Coulter and Kattenhorn, 2010).

The ability to resolve double ridges has improved markedly over time. Voyager 1 and 2 images returned in the 1970s portrayed the europan surface as relatively smooth, with few surface features. More recent, higher-resolution Galileo data reveal these lineations in finer detail, along with Europa's varying surface albedo and scarce impact craters (Greeley et al., 1998). This relative dearth of impact features indicates recent resurfacing in europan history, while also suggesting an average surface age of 40-90 Myr (Greeley et al., 2004; Bierhaus et al., 2009). On the basis of morphological analysis, several mechanisms have been proposed for this recent resurfacing, including cryovolcanism, tectonism, and diapirism (Head et al. 1999; Fagents,

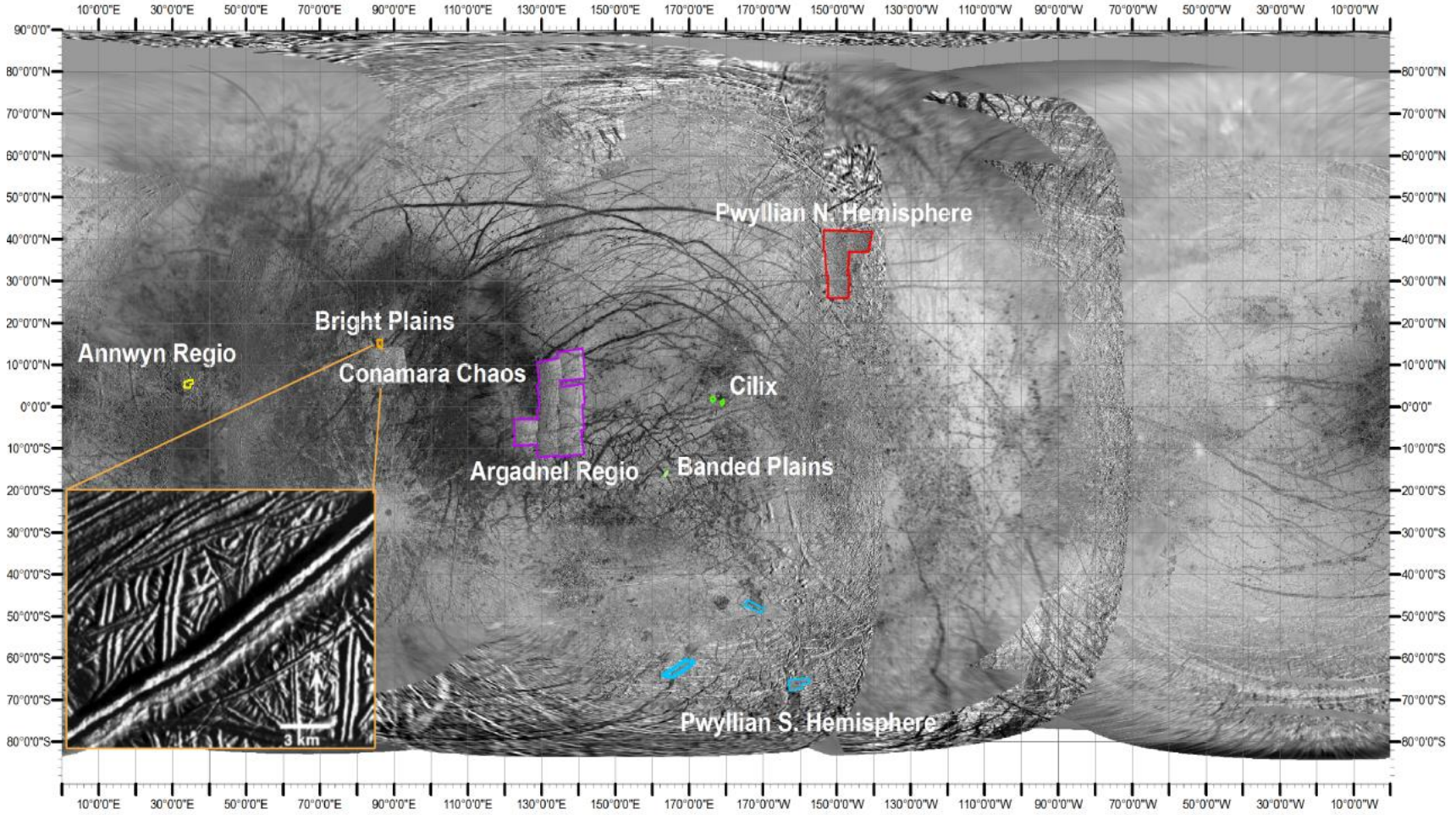

Figure 1. Europan 200m Galileo SSI image mosaic, showing ubiquitous surface lineations (courtesy of USGS Astrogeology). An inset of Androgeos Linea, a prominent double ridge in the Bright Plains region, is also included to show double ridge morphology (from Greeley et al., 1998). Study areas for this work are labeled in white. DEMs are located within the Cilix and Banded Plains regions (locations in green), whereas areas where shadow measurements were taken are in the other outlined regions.

2003). More recently, a new analysis supports the occurrence of lithospheric subduction on Europa that may have implications for the driving forces and necessary conditions for double ridge formation (Kattenhorn and Prockter, 2014).

Along with the heavily-lineated surface shown in Galileo Solid-State Imaging (SSI) camera images, Galileo spacecraft gravity data and magnetic field measurements also suggest that Europa has a liquid water ocean some 100km thick, surrounded by an icy outer crust above and underlain by a silicate mantle below (Anderson et al., 1998b; Khurana et al., 1998; Kivelson et al., 2000). The thickness of Europa's outer ice shell, which is dependent upon Europa's thermal state (Ojakangas and Stevenson, 1989), is highly contested. Both thin-shell (a few km) and thick-shell (tens of km) models exist; impact crater simulations predict a lower limit on ice shell thickness of 3-4 km (Turtle and Pierazzo, 2001), whereas modeling of ice diapirism predicts an upper limit of a few tens of km (Rathbun et al., 1998). Permutations of the two crustal thickness models have also been suggested, in which localized pockets of liquid H_2O exist within the icy shell (Pappalardo et al., 1999; Schmidt et al., 2011). With its hypothesized subsurface ocean, Europa is considered to be a prime candidate for the search for biological activity beyond Earth (Kargel et al., 2000). Information about the subsurface and the processes that may connect it with the surface are of great interest for future Europa missions, which could involve drilling through this outer layer of brittle ice to the ocean below (Weiss et al., 2011).

Double ridge formation could provide some constraints on the depth to this liquid ocean. Multiple hypotheses, with both tectonic and sedimentary processes, have been proposed for double ridge formation, with each mechanism giving different implications for the environment beneath the icy outer shell. These hypotheses all involve the exploitation of a preexisting vertical fracture, although the proposed ridge topography varies between mechanisms differ. The goal of

this work is to use these expected differences in morphometry – specifically, differences in slope angles and degree of symmetry – to test between two groups of these models.

Testing between these two groups of hypotheses for double ridge formation will enable a more comprehensive understanding of the europan subsurface processes that create or modify them. It will also help elucidate modification mechanisms and rates for the young lithospheric surface. Lastly, it will provide input for understanding the rates of communications between the subsurface ocean and surface environment. Although I do not evaluate individual formation mechanisms in this work, I am able to test between the two mutually exclusive groups of formation mechanisms. In the Background section, I first review the hypothesized formation mechanisms as presented in the literature and, on that basis, present my bipartite grouping of double ridge formation mechanisms according to ridge slope angle and symmetry. I then explain my techniques for deriving slope values. Next, I present my results and explain which group of formation mechanisms they are more consistent with. Finally, I discuss the implications of this work for Europa.

2. Background

2.1 Hypothesized Formational Mechanisms for Double Ridges

As reviewed by Dombard et al. (2013), six hypotheses currently exist for double ridge formation (Figure 2). These hypotheses all require a pre-existing vertical fracture, expected to have formed in response to a prior crustal stress state (Greeley et al., 2004). The type of subsurface material - whether liquid H_2O or warm ice - below the brittle surface ice layer depends on the hypothesis.

2.1.1 Cryo-sedimentary Mechanisms

Explosive cryovolcanism

Cryovolcanism involves the eruption of aqueous materials onto planetary surfaces. Although the composition of the materials differs from that of silicate magmas erupted in terrestrial volcanism, these aqueous mixtures are posited to exhibit similar rheological properties under the extreme conditions on icy satellites (Kargel et al., 1991). Explosive eruptions are visible on the saturnian satellite Enceladus, with water vapor plumes and icy particles extruding from its south polar region (Porco et al., 2006). Explosive cryovolcanism on Europa would similarly involve the eruption of H_2O droplets, which would freeze during their ballistic trajectories (Fagents et al., 1998; Kadel et al., 1998). This process has been compared qualitatively to fissure eruptions on Earth, due to the qualitative similarity of patchy, lower-albedo features seen along these terrestrial features as well as along ridges such as Rhadamanthys Linea on Europa, although the features compared are at vastly different scales (Fagents et al., 2000). Granular ice produced from these europan eruptions would be deposited on the surface at its angle of repose (AOR) (Kadel et al., 1998). Because the material forming the

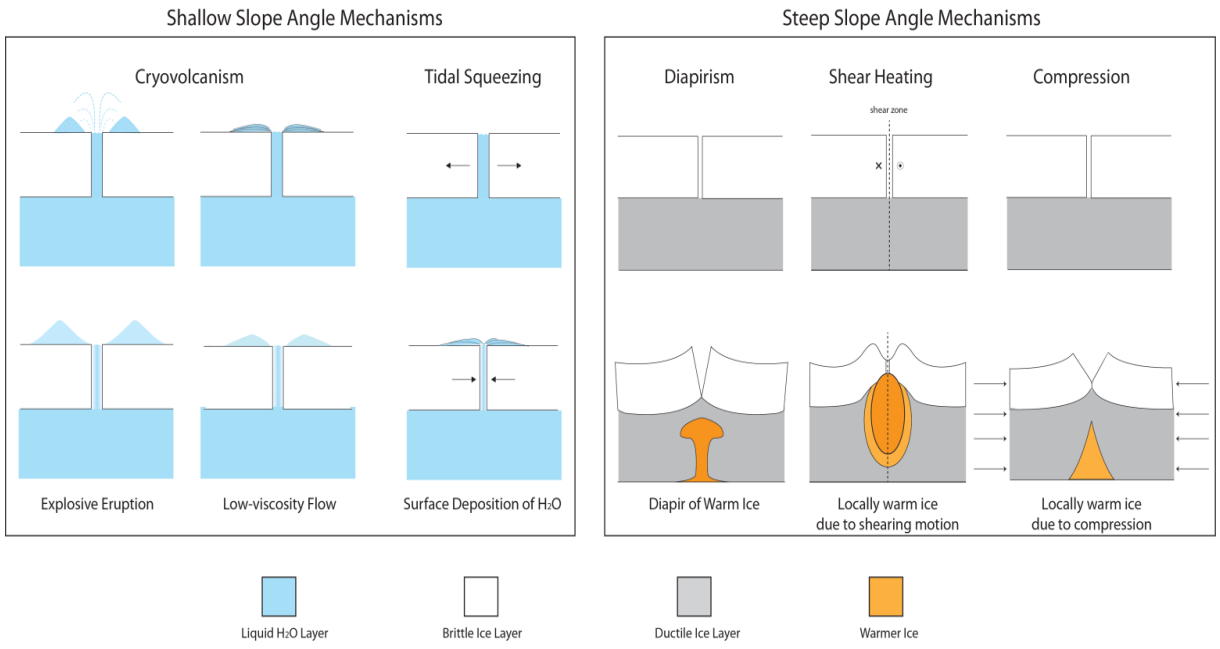

Figure 2. Double ridge formation mechanisms. The diagram shows two time-steps (arranged vertically) for each ridge formation mechanism. The top row shows the surface prior to ridge formation, and the bottom row shows the final surface expression of each formational mechanism (modified from Dombard et al., 2013).

interior and exterior ridge slopes (shown in Figure 3) would come to rest at AOR, I would expect individual double ridges produced by this mechanism to be self-symmetric. Sintering of this granular ice may be possible, and is suggested as a means to produce slopes steeper than the AOR in rare cases (Kadel et al., 1998).

Tidal Squeezing

Tidal forces on Europa are produced by its eccentricity, which is forced by orbital interactions with fellow Jovian satellites Io and Ganymede. The tidal squeezing hypothesis invokes the diurnal (~3.5 day) opening and closing of fractures (Greenberg et al., 1998). Globally, these fractures are oriented perpendicular to the maximum tensile stresses (Greenberg

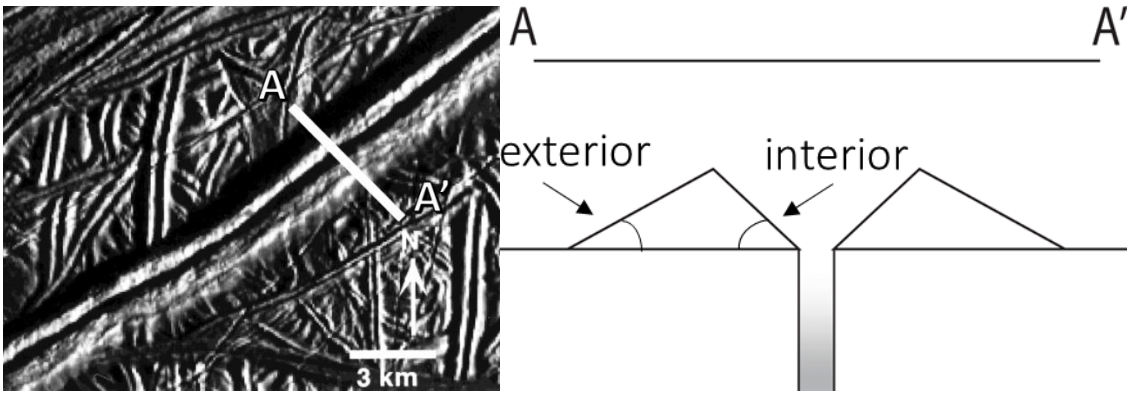

Figure 3. Simplified diagram showing cross section between double ridge, with exterior and interior angles shown (modified from Greeley et al., 1998).

et al., 1998). This orientation results in fractures also following a cycloidal pattern due to changes in the stress field over time (Hoppa et al., 1999b). As a fracture opens, water would rise up through the conduit, where it would then freeze. As the fracture closes, crushed ice and slush would be extruded onto the surface, where it would be then be deposited on either side of the fracture. According to the model, this process would continue on Europa from a period of 30,000 years up to a few million years (for the largest ridges), building up the double ridge of icy deposits over time (Greenberg et al., 1998). As the icy sediment builds up on either side of the fracture, the material closest to the fracture would fall inward (Greenberg et al., 1998). This material falling inward would in turn lower the angle of the interior slopes to the AOR of the material. The material extending away from the central conduit has been described as draping over previously formed ridges in some locations, which also suggests that this extruded material is loose and granular in nature and can flow freely (Greenberg and Sak, 2014).

Low-viscosity cryolava flows

Cryovolcanic flows have been invoked to explain the similar youthful appearance of other icy satellites in the outer solar system (Fagents, 2003). A molten cryolava flow on Europa could consist of briny fluids flowing laterally onto the surface. This type of flow is included as a possible component accompanying an explosive cryovolcanic eruption (Kadel et al., 1998). It has also been suggested that as a double ridge is built over time via tidal squeezing, the overburden produced by the double ridge could lower it underneath the water table of the central conduit (Greenberg et al., 1998). This lowering could result in shallowing of the double ridge slopes if they are spread laterally by this lower-viscosity component. Thus, it is expected that double ridges affected by low-viscosity flooding should have slope angles that are lower than the AOR.

Summary and implications of cryo-sedimentary mechanisms

Each of these cryo-sedimentary models should form double ridges with interior and exterior slopes at or below the AOR. Symmetry is expected for an explosive cryovolcanic model, whereas symmetry is not necessarily expected for either the tidal squeezing or effusive cryovolcanic models. Asymmetry is expected for a low-viscosity cryovolcanic flow, although it is possible that this mechanism could produce symmetrically flat slopes well below the AOR. Asymmetry is also likely for the tidal squeezing mechanism, where interior slopes may be shallowed as material falls into the central fracture. Implications for the cryo-sedimentary hypotheses include the requirement for a thinner ice shell, as each mechanism involves transporting liquid water or slush up through a central conduit bounded by cold, crustal ice. Timescales of tens of years have been suggested for the freezing of a conduit ~10m wide (Craft

et al., 2013), although conduits as narrow as ~1m have been suggested for tidal squeezing (Greenberg et al., 1998). The velocity of fluid ascent and the length traveled (crustal thickness) will play a major role in determining whether the conduit will instead freeze prior to surface deposition (as modeled by Wilson and Head, 1998). These hypotheses involving secondary components of surface flows may better explain the presence of darker albedo material seen on either side of many double ridges, which is suggested to result from surface deposition of briny subsurface ocean material (Greenberg et al., 1998). With the exception of explosive cryovolcanism, these mechanisms may be unable to explain the apparent symmetry of double ridges along trend seen in Galileo imagery. These features extend for thousands of kilometers in some cases, while terrestrial examples of fissure eruptions do not necessarily maintain this consistency along strike (Head et al, 1999; Fagents, 2003).

2.1.2 Brittle Deformation Mechanisms

Linear diapirism

Diapirism involves a more plastic material underneath the surface that rises buoyantly, deforming the brittle surface layer above. Terrestrial examples of diapirism include uprising salt domes that initially form anticlines, followed by the disruption of the overlying strata (Jackson and Vendeville, 1994). A variety of processes have been invoked to explain salt diapirism, including differential loading of sediment (Jackson and Vendeville, 1994). Diapirism may be occurring on Europa, at the locations of circular domes (termed "lenticulae"), which are hypothesized to be a result of rising ice that is warmer than the surrounding brittle ice layer (Rathbun et al., 1998). These ice diapirs would rise buoyantly due to the difference in density with the surrounding material. Linear diapirs may be produced on Earth if diapirism occurs

below extensional faulting. Similarly, this process has been suggested as a viable mechanism to produce europan double ridges (Head et al, 1999). Strain rates from diurnal tidal stresses may be sufficient to deform the upper ductile layer of ice along with the surface brittle layer. Upwarping of this fractured, brittle surface ice by plume activity would result in the observed double ridge form (Head et al., 1999). Upwarping surface terrain may explain why some double ridges appear to extend up the flanks of newer double ridges, although this appearance could also be explained via tidal squeezing if loose, granular material is deposited on top of older ridges (Head et al., 1999; Greenberg and Sak, 2014). Linear diapirism may also explain the presence of marginal troughs on either side of the double ridges (Head et al, 1999). Mass wasting could be a factor along the interior of the double ridge after uplift, based on features seen in high-resolution Galileo imagery (Head et al., 1999). However, the interior slopes of the double ridges produced via this mechanism should be steeper than AOR, or no less than the AOR if mass wasting does occur.

Shear heating

Plate tectonics on Earth produces areas of strike slip faulting, in which plates shear past one another laterally (Yuen et al., 1978). Morphological analyses indicate a component of shearing along many double ridge sets on Europa, with tens of kilometers in offset possible (Hoppa et al., 1999a; Coulter and Kattenhorn, 2010). A shear heating hypothesis (Nimmo and Gaidos, 2002) involves the generation of heat within a vertical fracture as shearing occurs. This heating could produce a buoyant, warmer ice layer underneath the fracture, as in the linear diapirism hypothesis. Results from 2D numerical modeling of brittle and ductile shear heating and heat flux indicate that heating at the base of the brittle layer could be sufficient to raise a

warm ice diapir by a few centimeters a year (Nimmo and Gaidos, 2002). However, in other simulations (Dombard et al. 2013), the uplift provided by this mechanism was not sufficient to flex the europan cryosphere and produce the ridge fore bulges that are present near some double ridges. As with the linear diapirism mechanism, this mechanism should produce ridges with interiors steeper than the AOR.

Buckling due to compression

While surface extension is ubiquitous on Europa, surface expressions of compression are scarce. It has been suggested, however, that subsumption bands may occur as part of europan plate tectonics (Kattenhorn and Prockter, 2014). Compressional relative plate motions on Europa are inferred from the reconstruction of separated lineaments in the bright plains region (Sullivan et al., 1998). In this hypothesis, ridge formation involves the buckling of the lithosphere due to the compressional stresses that result from this plate motion, and is suggested to have occurred in a densely fractured region (40°S, 205°W) (Sullivan et al., 1998). The compressional stresses required by this mechanism may not be consistent with the presence of extensional fractures typically found on either side of double ridge sets (Dombard et al. 2013), although extension could follow the compression.

Summary and implications of brittle deformation mechanisms

Each of these mechanisms suggests uplift of a pre-existing vertical fracture produced by tensional stresses, and so would tend to produce interior slope angles that are near to vertical, and therefore greater than the static AOR. The exterior slope angles should also be shallower than the interior slope angles (as drawn in Figure 2). Brittle deformation mechanisms as proposed require

a warmer, ductile ice layer beneath the colder, brittle surface layer. This ductile layer essentially adds another component to the brittle layer involved in the cryo-sedimentary models. Thus, the depth to the liquid water ocean beneath ridges created from these processes is likely deeper than that for ridges created from cryovolcanism or tidal squeezing. These mechanisms may better explain the consistent, smooth appearance of ridges over long distances than the shallow slope-angle mechanisms (Head et al., 1999). One complication with this suite of hypotheses is achieving the inferred double ridge heights. Modeling by Nimmo and Gaidos (2002) achieved ridge heights of ~100 meters, but calculations and measurements suggest that in some instances ridges may be over twice as tall (e.g., calculations by Kadel et al. (1998), DEM measurements by Coulter and Kattenhorn, 2010). Other attempts to model shear heating were unable to recreate features seen along double ridges such as flanking fractures or flexural bulges (Dombard et al., 2013).

2.1.3 Distinguishing Between Formation Hypotheses via Slope Angles, Symmetry

In this work, these six hypotheses from the literature have been categorized into two groups that reflect the magnitudes of the interior angles expected to result from the specific mechanism (interior and exterior slope angles, Figure 3). The distinction between these two groups is made on the basis of two morphological characteristics: slope angle and symmetry.

Slope angle refers to whether the expected interior slope angles are greater than or less than the angle of repose (AOR); one group includes those mechanisms that would form shallower-than-AOR interior angles, and the other group includes those mechanisms those that would form steeper-than-AOR interior angles. Angle of repose may be of two types. Dynamic AOR is defined as the angle at which moving granular material will come to rest after

avalanching, whereas the static AOR is the angle at which stationary material will begin to move downhill if exceeded. Because the observed slopes of the double ridges are at rest, they represent the static AOR.

The static AOR for icy grains on Europa is not well constrained. It has been assumed by comparison with terrestrial conditions to be ~34° (Bader et al., 2008). However, static AOR may increase by up to 5 degrees with decreasing gravity (Kleinhans et al., 2011). In addition, the shape of ice grains produced via cryovolcanism would also affect their angle of repose, as more angular, blocky particles can form a steeper angle of repose, approaching 40° for silicate materials (Friedman and Robinson, 2002). For this work, we assume a maximum static AOR of 45°.

A secondary analysis is made on the basis of slope self-symmetry or asymmetry (Figure 4). In this work, self-symmetry, or just symmetry, refers to similarity of the values derived for the interior and exterior slopes of a single ridge that is part of a double ridge structure. This characteristic would help to distinguish between the two groupings, as one type of – namely, interior slopes steeper than exterior slopes – is expected for ridges produced via brittle deformation, whereas symmetry is expected specifically for explosive cryovolcanism. Symmetry may occur for the other two cryo-sedimentary mechanisms, although it is not expected. Thus, mechanisms are evaluated with both of these morphological characteristics.

2.2 Double Ridge Degradation

Whereas my grouping of formation mechanisms is based on the original morphology that is expected for each mechanism, post-formation degradation of double ridges would tend to

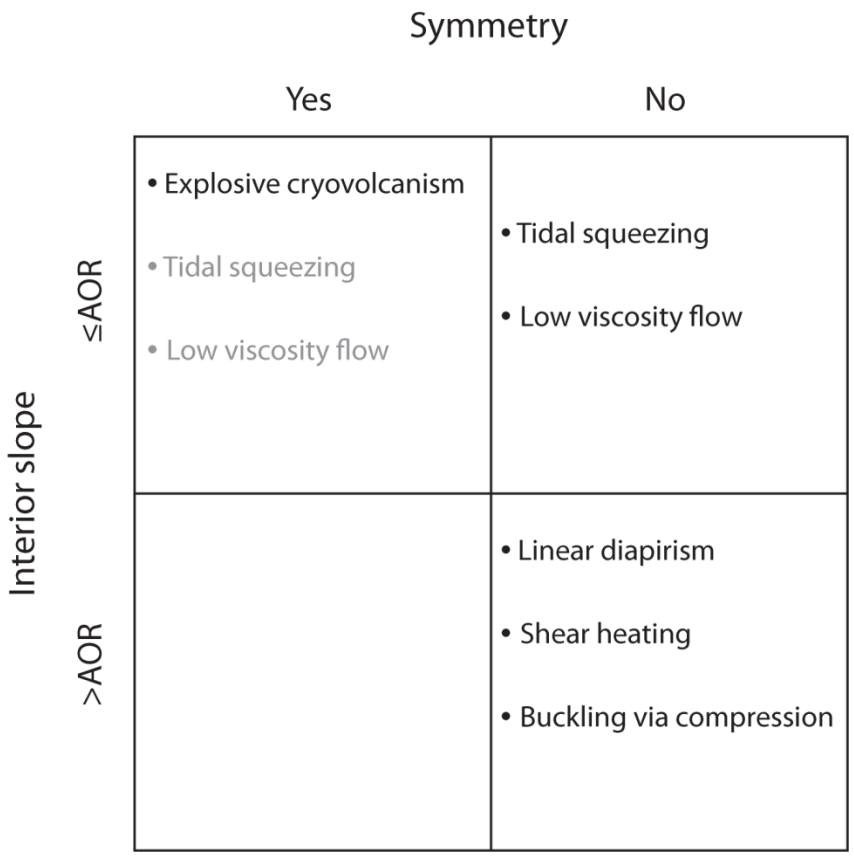

Figure 4. Chart of interior angle of repose (AOR) vs. expected ridge symmetry. Grey text indicates what is expected to be a less likely albeit possible scenario.

reduce the original slopes. Such degradation might occur through a variety of mechanisms. One such mechanism is impact cratering. However, europan impact-generated regolith depth is inferred to be ~1cm (Moore et al., 1999; Bierhaus et al., 2005; Moore et al., 2009). This depth, along with the paucity of impact craters on Europa, suggests that degradation of slopes by micrometeorite impact is minimal. Thus, this type of degradation is not expected to alter double slopes appreciably.

Sputtering erosion involves charged-particle impacts that erode surface H_2O. Galileo spacecraft energetic particle measurements and irradiation modeling suggest a sputtering erosion

rate of 0.02 μm yr^{-1} for Europa (Cooper et al. 2001). This rate would result in the erosion of ~1m of surface ice over a lifetime of 50 Ma, which suggests sputtering dominates over impact erosion on Europa (Moore et al., 2009). However, ~1 m of debris over the width of a double-ridge slope is unlikely to affect slope angles significantly.

Europa's surface ice is also affected by solar insolation and internal heating, which promote ice sublimation (Carlson et al., 2009). Ice sublimation could total up to 5m in equatorial regions, with less of an effect expected for more polar regions (<1m ablation over 50Ma) (Fagents, 2003; Hobley et al., 2013). Dark areas, interpreted as lag deposits, may also enhance sublimation (Fagents, 2003). However, sublimation is not expected to change slope angle significantly, because heat is preferentially trapped at the base of the slope, so that even with loss of material, the angle is maintained (Moore et al. 2009).

Viscous relaxation of ice is another process that affects icy satellites (Nimmo, 2004; Dombard and McKinnon, 2006). This process results in the shallowing of impact craters over time; and, depth to diameter ratios have been used to interpret of Europa's crustal thickness and viscous relaxation history (e.g., Bray et al., 2014). However, viscous relaxation is wavelength-dependent (Turcotte and Schubert, 2002), and it is unclear how significant of an effect this process would have for short-wavelength features on Europa such as double ridges. Features like ridges would likely be unaffected by large-scale relaxation experienced by longer-wavelength features, due to the support from the elastic ice layer underneath (Nimmo 2004). Although Coulter and Kattenhorn (2010) cite viscous relaxation as a possible reason why their double ridge slope measurements are below the angle of repose of ice, modeling suggests that viscous relaxation would not be a viable mechanism to erase or significantly modify folds on Europa, as the topographic changes would be undetectable or very minor (Dombard and McKinnon 2006).

Shear heating may generate heat to aid relaxation (Coulter and Kattenhorn, 2010), although the lack of offset in current data does not support viscous relaxation due to shear heating as a mechanism for slope modification. Thus, it is not expected that this type of modification will affect double ridge slopes significantly.

Mass wasting is inferred to be occurring along interior and exterior ridge slopes, and is inferred based on the highest-resolution images of Europan double ridges (Head et al., 1999; Moore et al., 1999; Sullivan et al., 1999; Moore et al., 2009). Local-scale linear features discernable inside some large double ridges in high-resolution (35 m/pixel or better) imagery are inferred to be terraces produced by slumping (Head et al. 1999, Sullivan et al. 1999, Moore et al. 1999). Loose, ~100-m-diameter blocks seen near one of these ridges, Androgeos Linea, further support this suggestion of mass wasting (Head et al., 1999). Talus slopes are inferred on the sides of rafted blocks in chaos regions (Sullivan et al. 1999) and where impact debris does not seem sufficient to produce this loose granular ice (Moore et al. 1999). Much of Europa's surface debris is attributed to downslope mass wasting and tectonic fracturing, and these surface modification processes might be ongoing (Moore et al., 2009). Thus, this process may indeed significantly alter both interior and exterior slopes of double ridges.

2.3 Previous Work: Double ridge Morphometry

The morphometry of double ridges has been discussed in a few previous conference presentations. Kadel et al. (1998) calculated double ridge dimensions from shadow measurements on high phase (low sun-angle) Galileo images and found average ridge interior and exterior slopes of 36.5° and 38°, respectively. They also found that the exterior slope value can be steeper locally (up to 55°), for which those authors suggested partial consolidation of the

material (similar to welded tuff formation on Earth). However, it is unclear how welding of the material would cause it to steepen from an initial slope at the AOR. The compacting or welding of individual grains together should decrease the volume uniformly but wouldn't necessarily steepen the angle at which the particles rest. Based on several factors (surface brightening, the lack of impacts, and appearance of surface frost), Kadel et al. (1998) proposed that europan ridges form from the gradual buildup of granular ice due to explosive cryovolcanic eruptions, analogous to terrestrial fissure eruptions with the deposits thinning rapidly outward away from a central vent. They also suggested that the central trough could form from later reopening of the fracture.

Bader et al. (2008) measured double ridge height, double ridge width, and peak-to-peak width based on topographic data from DEMs featuring 22 double ridges and 2 ridge complexes in the Bright Plains, Conamara Chaos, Cilix, Argadnel Regio, and Rhadamanthys Linea regions. Based on a maximum height to width ratio value of 0.53, they inferred a maximum average exterior slope angle of 28°. Most of their measured slope values fell between 10 and 20°. They also noted that the exterior ridge flanks can be very shallow, dipping only a few degrees. They proposed that gravitational collapse of sedimentary ridges may be responsible for these slope values below the angle of repose of granular ice, and suggest that this collapse occurs after ridges achieve some maximum height.

Coulter and Kattenhorn (2010), presented in a more detailed form in Coulter (2010), examined geometric relationships between cross-cutting double ridges. Their analysis included measuring (on Galileo spacecraft images) the plan view angle of cross-cutting, the total separation, the strike-slip offset, and the contractional offset between the cross-cutting ridges. They measured ridge height and width, along with interior and exterior slopes, from combined

stereographic and photoclinometric profiles along 24 double ridges. As before, the majority of slopes measured are less than 20°, and these authors suggested that these values are too low to be indicative of mass wasting of granular ice or deposition of granular ice from cryovolcanic eruption, and are more in favor of viscoplastic relaxation of warm ice. They also noted a significant shear component between the ridge sets, which may be accompanied by dilation (but does not necessitate it). Based on their results, they favor a model of ridge formation by brittle fracture due to shear heating, necessarily followed by viscous relaxation to achieve the shallow slope angles that were derived.

Those previous findings on double ridge morphology are summarized in Table 1 and show that slope values obtained in previous studies, using different techniques at different locations, are not all in agreement (Kadel et al., 1998; Bader et al., 2008; Coulter and Kattenhorn, 2010). Slope values calculated by Kadel et al. (1998) are greater than the values obtained by Bader et al. (2008) and Coulter and Kattenhorn (2010), and the different results have different implications for double ridge formation. However, the average values from all of those studies are less than the AOR assumed in the present work.

In a similar vein as the previous work, the present work involves constraining the double-ridge formation mechanism(s) through geometric analysis. This work increases by a few hundred the number of derived slope measurements relative to other studies (e.g., 210 individual profiles from Coulter and Kattenhorn, 2010), and so provides a robust dataset of slope values for spatially distributed and temporally diverse double ridges. Results from this study will also enable comparison between two methods of obtaining surface slope measurements and between two techniques for each method. The slope values obtained from this study expand upon our existing knowledge of ridge morphology and help constrain double ridge formation mechanisms.

Table 1. Summary of previous findings on double ridge morphometry.

Double ridge slope values	Kadel et al. (1998)	Bader et al. (2008)	Coulter (2010)[3]
Technique	Shadow measurements	Photoclinometric profiles, height to width ratios	Stereogrammetric and photoclinometric profiles
Number and type of measurements	Over 60 measurements[1] of ridge height width, slope angles	44 ridges: 265 topographic profiles, height and width, average ridge height, total ridge width, peak-to-peak width	24 double ridges, 210 topographic profiles, height and width, average ridge height, total ridge width, peak-to-peak width
Range or average	36.5° (interior), 38°(exterior)	10-20° (exterior, measured)	Majority <20° [2]
Maximum	55° (exterior)	28° (exterior, calculated)	n/a
Interpretation	Explosive cryovolcanism, some consolidation of material	Gravitational collapse (granular flow or viscoplastic)	Unconsolidated, granular ice not dominant component; ridges viscoplastically relaxed

[1]Number of individual ridges was not stated
[2]Did not specify whether these values were interior or exterior slope values
[3]Unpublished master's thesis. See also Coulter and Kattenhorn (2010).

3. Hypotheses

As per the discussion above, the proposed mechanisms for double ridge formation are here grouped into two different categories based on the interior slope angles – greater or less than static AOR – that would result from each mechanism (Table 2). These groupings in conjunction with previous studies lead to my two hypotheses for this work.

3.1 Null Hypothesis

Based on slope values derived from previous work (Kadel et al., 1998; Bader et al., 2008; Coulter and Kattenhorn, 2010), the null hypothesis in this work also favors double ridge formation mechanisms that produce slopes less than or equal to AOR. Thus, my null hypothesis is that double ridges are created by cryovolcanism or tidal squeezing. Evidence to support this hypothesis would be interior slope angles at the time of ridge formation of less than or equal to 45°, and symmetry of interior and exterior ridge slopes for explosive cryovolcanism (and possible symmetry for effusive cryovolcanism or tidal squeezing).

3.2 Alternative Hypothesis

My alternative hypothesis is that double ridges are created by mechanism that produce brittle deformation of the crust, namely, linear diapirism, shear heating, or buckling due to compression. Evidence to support this hypothesis would be interior slope angles at the time of ridge formation greater than 45°, and asymmetry between interior and exterior ridge slopes.

Table 2. Two groupings, based on the relative interior slope angles that would be produced, for previously proposed formational mechanisms.

Shallow Interior Slope-Angle Mechanisms (≤ AOR)	**Steep Interior Slope-Angle Mechanisms (> AOR)**
Cryovolcanism (explosive)	Linear diapirism
Cryovolcanism (effusive)	Shear heating
Tidal squeezing	Compression

4. Data and Methods

4.1 Galileo SSI Data

In this work, I used data from the Galileo mission and analyzed it using two different methods. Initially, some 100,000 images of the Jovian system were anticipated from the Galileo Solid State Imaging (SSI) experiment (Belton et al., 2000). Due to problems that arose with the main antenna, this number was reduced significantly to less than 2000, with ~200 images of Europa returned. Although much fewer than anticipated, the images returned from the SSI experiment were a significant improvement upon images of Europa returned from Voyager 1 and 2. These new images allowed for resolving double ridges in much finer detail, with ground resolutions as high as 21m/pixel.

Each image for this work was initially selected by locating Galileo image stamps in JMARS Outer Planet Moons and map-projected using online tools offered by the USGS Astrogeology Science center. PILOT (Planetary Imaging Locator Tool) is an interface provided on the web (http://pilot.wr.usgs.gov) to efficiently locate mapped surface images based on user-defined criteria (e.g., camera used, filters, geographic location) (Bailen et al., 2013). PILOT enables the user to select up to 50 individual images at a time by drawing surface polygons, manually entering known image coordinates, or by selecting named features of interest in a drop-down menu. Selected images can then be map-projected on the web via the Map Project on the Web (POW) service, which uses Integrated Software for Imagers and Spectrometers (ISIS) to map-project raw imagery according to user-defined parameters for the output image parameters (bit type) and map-projection (sinusoidal, equirectangular, etc.).

4.2 Shadow Measurements

I used two separate shadow measurement techniques: the exterior and interior shadow length technique. Both techniques – including the exterior shadow length technique – are used to derive the interior double ridge slopes, although each technique has unique assumptions.

4.2.1 Exterior Shadow Length Technique

The exterior shadow measurement technique is one way to derive the interior angle β of a double ridge. The height (h) of a double ridge can be easily calculated from the length of its exterior shadow (s) from the ridge centerline and the solar incidence angle ϕ:

$$h = \frac{s}{\tan \phi} . \qquad \text{(eq. 1)}$$

For europan imagery, the solar incidence angle is measured from the surface normal and was derived from the label file (.lbl) that accompanies each image file (.img). The shadow length can be measured directly off of an image either in qview in ISIS or in ArcMap; these individual measurements were taken in ArcMap. After finding the down sun double ridge height, the peak-to-peak distance between the two ridge tops is measured. The midpoint of the ridge system is considered to be half of this peak-to-peak distance (*ptp*). When the ridge height (h) and midpoint (m) are known, the calculation of the interior angle is as follows:

$$\beta = \tan^{-1}\left[\frac{h}{m}\right] . \qquad \text{(eq. 2)}$$

Figure 5 illustrates the geometric relationship between the variables used in this technique.

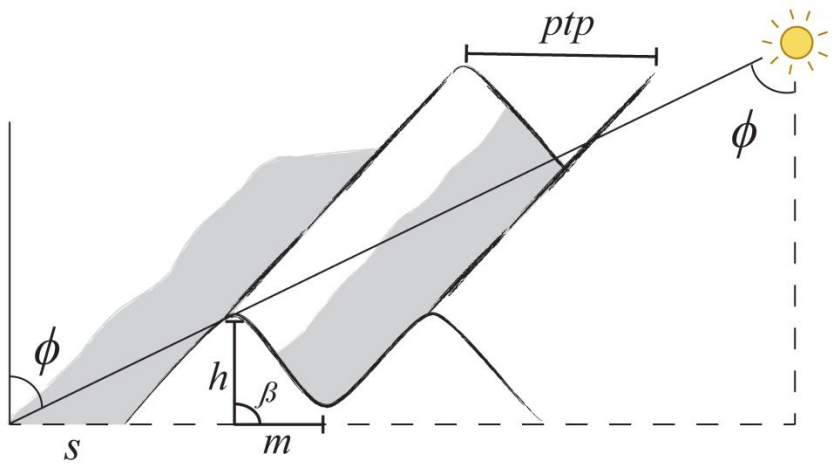

Figure 5. Oblique dross-sectional view (to left) and perspective view (to right) of idealized double ridges showing variables used in calculation of interior slope from exterior shadow measurements (Eqs. 1 and 2). The location of the ridge shadows is illustrated in grey shading.

Assumptions

This technique assumes that the peak-to-peak distance measured on a double ridge can be halved to find the length (*m*) of the facing interior sides, that is, that ridges meet in the center with no flat space between them at their bases. However, a space may exist between the ridges, in which case values obtained by this method would be lower than values obtained along the same ridge section with the interior shadow length technique. As such, this method produces a lower-bound for the ridge interior slopes. If the values obtained from the shadow length technique presented here are higher than the interior shadow length technique, this result may be indicative of areas where the ridge sets have become superimposed upon one another instead of being separated.

Exterior shadow length technique measurements

Five measurements for the values of the exterior shadow length were taken along each profile line in ArcMap, perpendicular to ridge trend. These data, along with the average midpoint value for the double ridge, were used to calculate the interior angle. Five measurements were taken in order to produce more robust data for images that have a variety of pixel resolutions, and to generate error bars for the resulting interior angle β. Sections with 500m profile spacing were used for higher resolution imagery of double ridges (20 - 45 meters per pixel), while sections with 1000 meter spacing were used for lower-resolution imagery for longer ridges (>1000km). Ridges in areas with high albedo variation or dark patches on either side of the ridge were not preferable for this technique, as this change in albedo added a further complication in determining boundaries of the shadows. Profile lines were skipped were albedo variations were too extreme, where cross-cutting was present, or if shadows were discontinuous along the double ridge.

Correcting exterior shadow length measurements oblique to sun direction

This exterior shadow measurement technique assumes that the sun illumination direction is perpendicular to the trend of the ridge. However, the sun illumination direction may change significantly from image to image. Some ridges are rather sinuous, which changes the illumination direction relative to the ridge, so sections of ridges were chosen where the ridge trended consistently in one direction to simplify corrections.

Figure 6 shows the two possible scenarios for the shadow length corrections, with the measured shadow length (*Sm*), corrected shadow length (*Sc*), and angle between the double ridge and subsolar azimuth (φ) shown. In the simplest case, the double ridge trend is perpendicular to

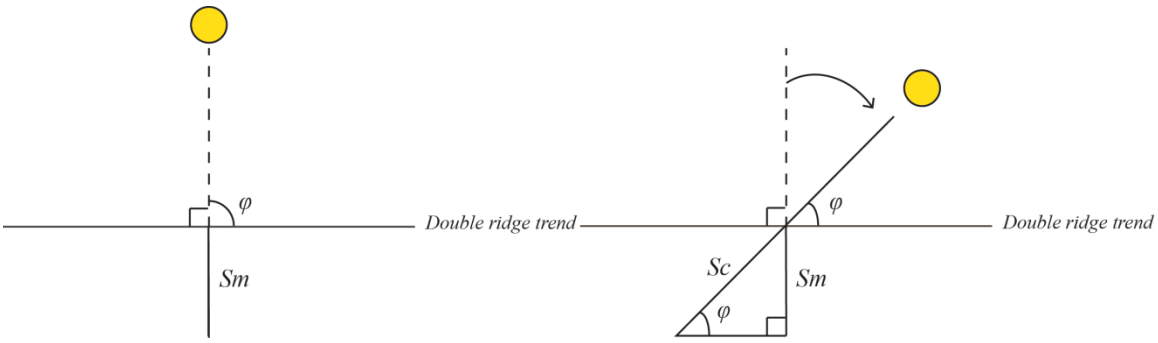

Figure 6. Plan view sketches illustrating the exterior shadow length measurement technique. In the simplest case (left), the subsolar azimuth is perpendicular to double ridge trend, so that ϕ is less than 90. In the more common case (right), the angle between the subsolar azimuth and double ridge trend (ϕ) is less than 90°.

the incoming subsolar azimuth, requiring no correction. In this simplified case, φ equals 90°, thus:

$$sin\,\varphi = \frac{Sm}{Sc}\,, \qquad \text{(eq. 3)}$$

and

$$Sc = Sm \cdot \csc\varphi = Sm \cdot 1 = Sm\,. \qquad \text{(eq. 4)}$$

In the more common scenario, the solar illumination comes in at an oblique angle to the double ridge trend. The angle φ is less than 90°, and this lower angle in turn increases *csc* (φ), resulting in a larger value for corrected shadow length *Sc*. To determine the angle φ, the individual images were viewed in GIMP, and their trends were measured using the measure tool (Figure 7). These trends were compared to the listed subsolar azimuths in the image label files, which are measured clockwise from 90° (due east) relative to the image center.

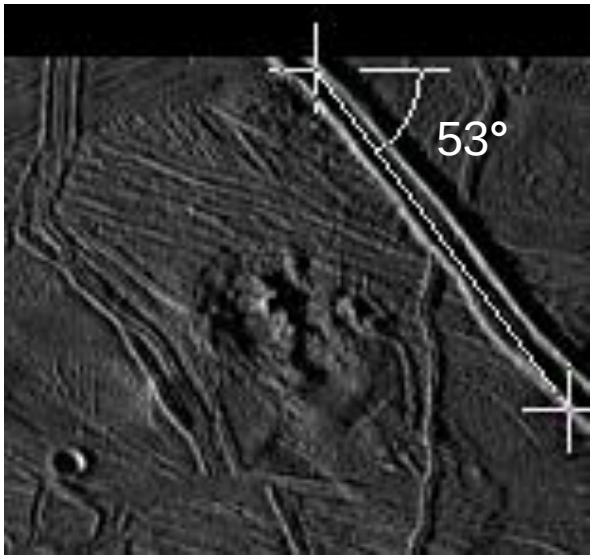

Figure 7. Illustration of measuring double ridge trend in GIMP with the measure tool in order to apply correction shown in Figure 8. SSI images are oriented so that north is to the right.

4.2.2 Interior Shadow Length Technique

The interior angle can also be calculated from measurement of the interior shadow, as derived by Kadel et al (1998) and shown in Figure 8 (their Figure 2). For this calculation, two equations for the ridge height *h'* are set equal to one another:

$$x \tan \beta = y \tan \alpha = h' , \qquad \text{(eq. 5)}$$

$$\tan \beta = \frac{y}{x} \tan \alpha , \qquad \text{(eq. 6)}$$

and

$$\beta = \tan^{-1}\left[\frac{y}{x} \tan \alpha\right], \qquad \text{(eq. 7)}$$

where β is the interior angle of the double ridge set, α is the sun altitude angle (90° minus the solar incidence angle), *y* is the ridge interior length in shadow, and *x* is the length of the illuminated portion of the ridge interior. The measured length values for x and y combined

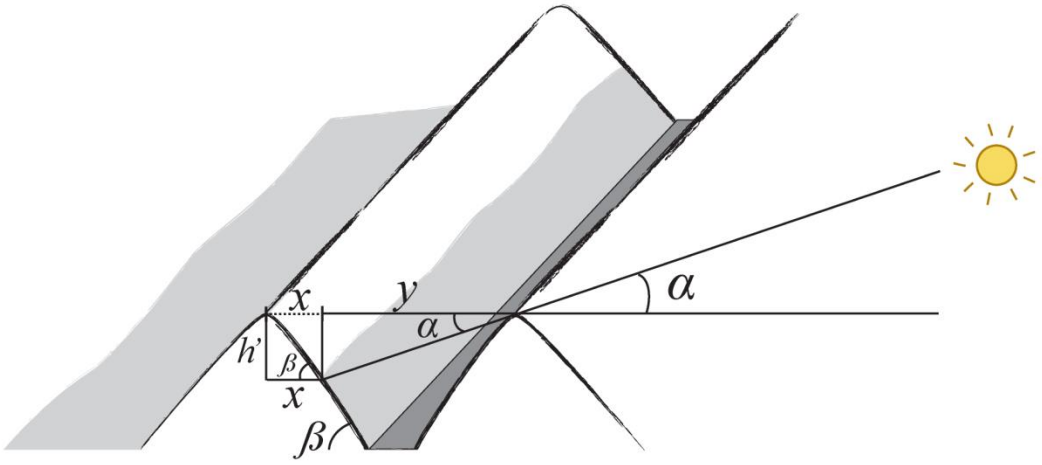

Figure 8. Interior slope angle determination from interior shadow and other planview measurements, modified from Kadel et al. (1998). The illuminated interior length (x) and interior length in shadow (y, shaded in grey) are represented. The peak-to-peak distance between the ridge sets should then be equal to x plus y. From these values and the known solar altitude, the interior angle β can be calculated.

should be equal to the peak-to-peak distance of the interior. The angle β and the angle ϕ are complementary (Figure 8). Whereas the exterior shadow length technique assumes that the two interior ridge slopes meet, this technique presented by Kadel et al. (1998) can be used to calculate the interior angle β regardless of whether a gap exists between ridge sets (Figure 8).

Assumptions

This method assumes that the two ridge heights are equal. There can be offset between ridge heights on Europa, as seen from digital elevation models, so this assumption may not hold for all double ridges. Figure 8 portrays ridge peaks coming to a single point on either side of a trough, whereas the ridge tops might instead be curved, which could affect resulting slope values. In the instance where a clear ridge peak is not seen, several measured peak-to-peak distances were averaged to get a best estimate.

Interior shadow length technique measurements

Five measurements for the values of x and y were taken along each profile in ArcMap, perpendicular to the ridge trend, and averaged. Averaging was done in order to produce more robust measurements for images that have a variety of pixel resolutions, as a slight change in the measurement for lower-resolution images could have a significant effect on the resulting interior angle β. Measurements were taken along the same profile lines as for the simple shadow length technique to enable direct comparison between the two techniques. For this technique, clear boundaries between the areas that were illuminated and in shadow were required. If this boundary was not clear, or if there were significant albedo variations in the interior of the ridge, the profile was skipped. These measurements did not require a correction with double ridge trend, as the ratio of the interior sections ($\frac{y}{x}$, Figure 8) does not change with a change in the angle offset from horizontal.

Comparing techniques

Comparing the slope results from the exterior shadow length technique and the interior shadow length technique may be useful for determining the interior characteristics of double ridges (Table 3). For instance, when both techniques are applied along the same profile and a space exists between the ridges, the exterior shadow length technique should give a lower interior angle than the interior shadow length technique. A higher β value obtained from the exterior shadow length technique would instead suggest that there is no space in between the ridges, or that the ridges are superimposed upon one another. It may be possible to confirm

Table 3. Summary of comparison between the interior and exterior shadow length techniques used in this work. Three scenarios are possible in this comparison: the interior technique and exterior technique produce similar values, the interior technique produces steeper values than the exterior technique, or the interior technique produces shallower values than the exterior technique.

Comparison of results from two different shadow length techniques	
Possible Scenario	Implications
Interior - Exterior = 0	Interior slopes meet at the ridge midpoint, at the height of the exterior land surface
Interior - Exterior > 0	Interior slopes have a gap at the height of the exterior land surface
Interior - Exterior < 0	Interior slopes are superimposed

compression between ridge sets in this case by looking at other structural indicators. For this reason, both techniques are used along each shadow length profile where applicable.

4.2.3 Site Selection

Galileo images used for shadow measurements were selected based upon the presence of continuous shadows along double ridges and the lack of significant cross cutting or albedo variations along ridge sections. Images from ten locations on the europan surface were grouped into a small number of areas to develop an understanding of ridge morphology in a given area. Two regions were chosen based on previously published work with ridge cross-cutting relationships mapped: work by Kattenhorn (2002) focused on ridge relationships in the Conamara Chaos region (15°N, 273°W), whereas work done by Spaun et al. (2003) focused on southern Annwyn Regio (5°N, 327°W). Another region, Argadnel Regio, was chosen based on work done by Figueredo and Greeley (2004), in which ridge relative age relationships were mapped out within four time periods. Finally, individual double ridge images were compared

with Pwyllian ridge locations mapped by Bunte et al. (2013) to determine regional relative age relationships in areas that had not been previously mapped.

4.3 Creation of stereogrammetry DEMs in ISIS 3 using Ames Stereo Pipeline

Ames Stereo Pipeline (ASP) was used within the current version of Integrated Software for Imagers and Spectrometers (ISIS 3) to generate digital elevation models (http://byss.arc.nasa.gov/stereopipeline/binaries/asp_book-2.4.1.pdf). These programs are provided by NASA Ames Research Center Intelligent Robotics Group and the United States Geological Survey as free, open-source software. ISIS is typically used to take raw satellite imagery and convert it other formats such as map-projected image cubes (e.g. Shirley et al., 2000; Anderson et al., 2011). ASP consists of automated stereogrammetry and geodesy tools used to continue processing the planetary imagery after map-projection (Moratto et al., 2010). It was designed to allow for expedited processing of planetary imagery into digital elevation models (DEMs) (Moratto et al., 2010). The stereo mapping and terrain extraction process in ASP is automated.

4.3.1 Selection of Stereo-Pair Images

The first step in the selection of stereo pair images was determining where images overlapped. Two important factors that were then considered with selecting stereogrammetry images for ASP were 1) the differences in the resolution and 2) spacecraft emission angles for both images. The higher-resolution image of the stereo pair is coarsened to have the same resolution as the base image in this process. For the limited number of possible stereo pairs that exist for Europa, this coarsening poses the challenge that the resulting DEM may be too coarse to

measure double ridge slope angles effectively. For this reason, stereo pairs were chosen such that the difference in resolution of the two images was minimized. For the spacecraft emission angle, a difference of 10-20° is ideal to derive surface topography using the parallax effect. Galileo imagery poses another challenge in that most overlapping images have a difference in emission angle of ~10° or less, so emphasis was placed on using image pairs with the appropriate difference in emission angle to effectively derive topography.

4.3.2 Processing in ISIS 3

ISIS is used to first process raw imagery returned from spacecraft; the imagery then becomes level 0, 1, or 2, depending on the amount of processing done. Image and label files taken from NASA's Planetary Data System Imaging Node were entered into ISIS 3 for processing. Each spacecraft instrument with an available camera model in ISIS has its own unique prefix for processing; for the Galileo Solid State Imager, the command line inputs have the prefix "gllssi". The process for generating a stereo-pair DEM in ISIS is as follows: both sets of image and label files are placed into their own directory along with a stereo file. After changing the current directory in ISIS into this folder, both label files are converted to cube (.cub) files using the *gllssi2isis* command. SPICE data with information on the spacecraft position, solar geometry, etc., is then attached to both cube files using the *spiceinit* command to give the files latitude and longitude information. The command *gllssical* radiometrically calibrates the two images, turning them into level 1 image cubes.

The command, *cam2map*, map-projects the images to one another by orienting the smaller image in relation to the large image. The order in which the two images are entered into *cam2map* is important: the command needs to be run on the lower-resolution image first, then

the higher-resolution image is aligned to it. Aligning the images enables ASP to find tie points. Using *cam2map* results in the higher-resolution image being scaled down or coarsened to match the resolution of the base image, which is preferable to artificially improving the resolution of the base image. The output file for this command is a Level 2 image cube.

This image cube can then be used in the ASP, using the stereo command. In order to run the stereo command, a default stereo file is required. This file must be located in the same directory as the other output image files, and the stereo default parameters are adjustable to suit the needs of the user. For Europa imagery, the parameters for the corr-search function were adjusted. The default inputs for the corr-search bounding box (-100, -100, 100, 100) encompass the changes in x-y coordinates between the two images. These bounding box values were too broad for creating sufficient good pixel maps, and were subsequently refined. This command produces several output files such as the rectified input images, images containing information on tie points (.match and .vwip files), and a good pixel map and point cloud image, so new subdirectory was created to hold these results.

The *point2dem* command uses the output point cloud information from the stereo command to generate an 8-bit GeoTIFF terrain model. The command requires knowledge of the center latitude and longitude of the base image, which can be found by running the *caminfo* command on the image cube. In this step, the map projection of the DEM is defined. The map projection used in this work is Europa Equidistant Cylindrical (projection code IAU2000:50210). As changes in map projection can affect surface slopes, the same projection was used on all DEMs that were analyzed for this work. An orthoimage was also generated during this step using the *orthoimage* command. The orthoimage is an image that is geometrically corrected and coarsened to be at the resolution of the DEM, such that true distances can be measured. The last

command, *colormap*, was run on the DEM .tif file for viewing the color-coded elevation changes. This command outputs an image of the DEM showing color-coded elevations. Three DEMs total were generated in ASP for use in this study.

4.4 Generating Stereogrammetry DEMs in SOCET-SET

SOCET-SET (SOftCopy Exploitation Toolkit Set) software, offered by BAE systems, includes more sophisticated matching tools than those used by ASP in ISIS (Bandukwala, 2011). ISIS has image matching tools to ensure that images align correctly to one another. However, the number of tie points it utilizes to do so is sparse, and the tie points may not be placed accurately onto the ground surface. The user can create many tie points in SOCET-SET to build a more accurate surface model. SOCET-SET relies more on the user than ISIS to determine whether tie points between images are sufficient, and whether the resulting DEM is accurate or has errors that require corrections. A benefit for SOCET-SET is that the user can manually edit individual DEM posts to correct errors created during processing, which is not possible in ISIS.

4.4.1 Site Selection

Individual images were chosen based on similar criteria to that of the stereogrammetry DEMs in ISIS 3: differences in the resolution and spacecraft emission angles for both images were considered the most important factors. Prior to choosing the images for SOCET-SET, values for the individual pixel resolution, emission angle, incidence angle, subsolar ground azimuth, and subspacecraft ground azimuth were compared to determine viability of the image pairs. Users initially determine whether two images are well-suited to use with SOCET-SET by calculating the differences in resolution, viewing geometry, and illumination direction of the

images. The difference in pixel resolution is calculated by dividing the coarse resolution by the fine resolution. A value of 2.5 or greater is considered insufficient for generating a DEM, whereas a value below this threshold should result in better-resolution DEMs. As for the ASP DEMs, the difference in emission angle was also examined for the stereo-pairs used in SOCET-SET to determine whether topography could be generated with the parallax effect. The subsolar azimuth and subspacecraft ground azimuth were also considered; images with a difference in illumination direction greater than 45° are not considered good candidates for generating DEMs with SOCET-SET.

Based on these criteria, several of the potential stereo-pairs were ruled out as not having appropriate geometries or sufficient differences in resolution. Two localities were found to have adequate data for DEM generation in SOCET-SET. Two individual DEMs overlapped with the DEMs made in ASP as well, which allowed for comparison between the two techniques. A total of five DEMs were prioritized for creation in SOCET-SET based upon the size of the double ridges, to ensure that slopes could be derived successfully, and those stereo-pairs that had already been used to create DEMs in ASP.

4.4.2 Processing Steps

First, a SOCET-SET project was created. The coordinate system and datum were selected in this step; for Europa, an estimate of ± 100m was chosen for the expected elevation range. Typically altimetry tracks are used to control a stereo pair to a reference system. As altimetry information was not available for europan images, an image mosaic was used as a horizontal control. The Galileo SSI images were imported into SOCET-SET using the import_frame program. Multi-Sensor Triangulation (MST) was used to perform bundle adjustment, or improve

how the images are registered to one another and to the ground truth. In this step, the framing camera parameters describing the spacecraft positioning and pointing accuracy were specified to be applicable for europan Galileo spacecraft images. The nadir-most image was held fixed during this process, while six parameters were set to adjust the positioning and pointing for the second image to control it to the nadir-most image:

x	2000m
y	2000m
z	500m
ω	0.00001m/s
φ	0.00001m/s
κ	0.001°

with x, y, z being the position parameters of the spacecraft, and ω, φ, κ being the velocity parameters describing the rotation (roll, pitch, yaw, respectively) around the three spacecraft axes. The position parameters are chosen from trajectory information for the given mission the image is obtained from (in this case, the Galileo spacecraft), and the velocity parameters are based on the start to end duration of the image. These values are essentially an expected adjustment amount for the positioning of the second image, although it can adjust within these specified values to produce a more accurate match to the nadir-most image.

MST was set up for relative orientation, with a minimum of six equally spaced tie points, set using the interactive point measurement function. The tie points were manually placed on the ground with a topomouse as the images were viewed in stereo. Tie points were set in areas with relatively smooth terrain wherever possible, to ensure the images were both grounded. During this step, one image is locked, and the other is aligned to it, clearing the visible parallax effect.

Autocorrelation, or having SOCET (instead of the user) place the point, is also possible but the user should confirm that SOCET has placed a point correctly before continuing.

After all tie points have been placed, the user performs a "simultaneous solve" that outputs the RMS error of the tie points. A RMS value of 1.0 or below is considered sufficient accuracy for DEM generation. Individual points can be re-measured through the simultaneous solve menu if there are large residual errors. In this work, the RMS error values for the tie points measured were confirmed to be less than 0.6 before continuing. At this point, elevation data (such as Mars Orbiter Laser Altimeter data (Smith et al., 2001)) could be added for the tie points, but altimetry data do not exist for Europa. Epipolar rectification images were generated next for the automatic terrain extraction. The Next Generation Automatic Terrain Extraction (NGATE) is typically used for martian images, because it is considered the most advanced and efficient option. Although different strategy files were implemented through trial and error for the Europa images, NGATE was unsuccessful in generating topography for Europa. Ultimately, using the Automatic Terrain Extraction (ATE) was the most successful in generating the Europa DEMs for this work.

The Europa DEMs generated in SOCET-SET did require editing, as the terrain extraction techniques did not fully capture the ridge topography in some places. Areas were corrected using the following editing tools in the Interactive Terrain Edit (ITE) menu: Post Editing, Area Editing, and Geomorphic Editing tools. In the final steps after DEM creation, orthoimages were generated in SOCET. The DEMs and orthophotos were exported to ISIS 3 and converted to cube files with georeferencing information. One important consideration was the radius for Europa that was used; the value used in SOCET-SET differs from the ASP value used (the IAU 2006 value of 1562090.0 meters vs. the IAU 2000 value of 1564130.0 meters, respectively). Five total

stereo-pair DEMs were generated using SOCET SET and exported as cube files to view in ArcMap. The two additional DEMs over the three DEMs created using ASP were possible because of the SOCET SET ability for user editing.

4.4.3 Analyzing DEMs in ArcMap 10.1 and Excel

DEMs derived from ASP and SOCET-SET were uploaded into ArcMap 10.1 for analysis. As with the shadow measurement data, profiles were taken every 500m along, and perpendicular to, the ridge trend. Individual profile data were extracted using the 3D Analyst Profile Graph tool, which measures the change in elevation for a profile line drawn on the DEM. These elevation data were exported into Excel and the x and y values were plotted. The double ridge interior and exterior slopes were derived using the SLOPE function, which fits a linear regression line to the profile data and returns the slope value in radians. A simple conversion was applied to convert the slopes into degrees. For collecting data of double ridge profiles, a minimum of five points along the ridge interior was necessary. One point was used to identify the visible change in slope at the profile top, one identified the visible change in slope at the profile base, and the three points in between were used as input for the SLOPE function. Requiring five points over interior slopes helps to mitigate effects of slope degradation that could exist at the base of the profile by excluding the ridge top and ridge base, and including only the three middle points in the slope analyses. In a few cases, the resolution of the DEM limited the amount of interior points along the profile data taken, so only two middle points were used to derive slopes. If the interior showed possible evidence of mass wasting (e.g., possible slump features or abrupt shallowing of the slope at the base), data were not taken at that location.

4.4.4 Comparing ASP and SOCET-SET DEMs

A total of eight DEMs were generated using ASP (three DEMs) and SOCET-SET (five DEMs). Of these, two DEMs created with different techniques could be directly compared. Profile lines were drawn such that they overlapped in the two images to enable direct comparison along individual profiles. Slope maps were also generated to determine the range of overall slope values along each individual ridge. To generate a slope raster in ArcMap, the Slope tool in the Spatial Analyst Toolbar is used. This function generates slope values for each cell by taking the change in z-value between cells and outputs a new raster comprised of these values. The output can either be in units of degrees or percent rise.

4.4.5 Statistical Analyses of Data

Data derived from both shadow measurement techniques and DEM measurements were compiled to calculate statistics. Histograms were generated to visually interpret the slope sample distributions to see how they varied with each technique used. Student's t-tests were also applied for slope samples that were determined to be normally distributed (f-test resulting in a p value of less than 0.05).

5. Results

5.1 Digital Elevation Models

Because the DEMs generated in ASP were deemed not as robust as the SOCET-SET DEMs (as described in Section 4.4), the results from the five SOCET-SET DEMs are shown here first. The ASP results are included for completion and comparison with the SOCET-SET data, but not for geologic interpretation. The comparison of slope values derived from the overlapping SOCET-SET and ASP DEMs is discussed in Section 6.1. Results from both techniques are summarized in Table 4. Each of the figures and tables in this section following Table 4 are presented in the Appendix.

For each DEM, four figures are presented:

1) DEM
2) Orthoimage
3) Slope map
4) Slope frequency distribution

5.1.1 Banded Plains region: stereo pairs with 3800r.img (SOCET-SET and ASP)

In the Banded Plains region, three images (2825r.img, 2828r.img, and 2832r.img) were used as stereo pairs with base image 3800r.img to generate three overlapping DEMs in SOCET-SET (Figure 9). Accompanying orthoimages and slope maps are shown in Figure 10. These images feature two prominent double ridges near 16.0°S, 194°W. The individual DEM resolution was set at 100 meters per pixel in SOCET-SET software. For each DEM, 500m profile spacing was used. The same base image was also used in ASP to generate a DEM with 2828r.img.

Table 4. Results from DEMs created with SOCET-SET and ASP in the Banded Plains and Cilix regions, including total number of profiles, ranges for interior and exterior slopes, and the average values for interior and exterior slopes. Interior slopes were not derived for 7542r.img in SOCET-SET and 744r.img in ASP, as there were not sufficient data points available.

			Slope range (°)		**Slope average (°)**	
DEM	**Created with:**	**Number of profiles**	Interior	Exterior	Interior	Exterior
Banded Plains 2828r.img	SOCET-SET	26	21 - 69	17 - 59	38	30
Banded Plains 2828r.img	ASP	24	9 - 67	6 - 67	25	30
Banded Plains 2832r.img	SOCET-SET	18	26 - 71	24 - 78	48	55
Banded Plains 2825r.img	SOCET-SET	9	6 - 18	4 - 20	11	11
Cilix East 7442r.img	SOCET-SET	18	11 - 23	6 - 14	14	14
Cilix East 7442r.img	ASP	5		2 - 4		3
Cilix East 7446r.img	ASP	11	6 - 23	2 - 17	12	8
Cilix West 7542r.img	SOCET-SET	5		8 - 17		13

Banded Plains DEM 2828r.img - SOCET-SET

Twenty-six profiles lines were taken along one double ridge. The DEM shows a prominent double ridge that is over 200m tall (Figure 9). Values for interior and exterior slopes derived from the topographic profiles are listed in Table 5. For interior slopes, values range from 21 to 69°, while exterior slopes range from 17 to 59°. The total distribution of slope values is shown in Figure 11, with most values plotting between 30-45° for the interior and 25-35° for the exterior. Average values for interior and exterior slopes are 38 and 30°, respectively. The cumulative percentage is also plotted along with the histogram, with the majority of slopes falling below the AOR (80% of the interior slopes and 90% of the exterior slopes). Topography for each of the profile lines is shown in Figure 12, with both exterior and interior values for both halves of the double ridge plotted. Most values fall between 20 and 45°, with some interior slopes reaching upwards of 60°.

Banded Plains DEM 2828r.img - ASP

Twenty-four profile lines were taken along a single double ridge; this ridge is the same ridge as pictured in Figure 9 for the 2828r.img and 2832r.img DEMs created with SOCET-SET (Figure 13). Profiles 1 to 24 overlap with profiles 3 to 26 for the SOCET-SET DEM of the same double ridge. For interior slopes, values range from 9 to 67°. Exterior slopes range from 6 to 67°. The distribution of interior and exterior slopes is plotted in a histogram in Figure 14, with both populations centering around the 20-30° slope bins. The vast majority of the interior slopes are below the AOR (96%), whereas 82% of the exterior slopes are below the AOR. Average values for interior and exterior slopes are 25 and 30°, respectively. The change in slope values along trend is shown in Figure 15, which shows a wide range for both interior and exterior slopes (~10-50°). As the DEMs created with 2828r.img in SOCET-SET and ASP overlap, the two are also compared in this figure. Both the SOCET-SET and ASP have the same value for the mean exterior slopes (30°), although the interior mean value for ASP is much shallower than the SOCET-SET value. Both sets of slope measurements occupy the region between 20-50°. Some ASP slope values fall below 20°. SOCET-SET values generally do not.

Banded Plains DEM 2832r.img - SOCET-SET

Eighteen profiles were taken for one double ridge (Figure 9). This double ridge is a continuation of the double ridge in the 2828 DEM, with profiles 1-6 overlapping with profiles 21 - 26 on the 2828 DEM. Values for interior and exterior slopes are listed in Table 6. The exterior and interior slopes for this ridge on the northern section are typically steeper (60-80°), while the southern half is shallower (30-50°). Interior slope values range from 26 to 71°, and exterior slopes range from 24 to 78°. Average values for interior and exterior slopes are 48 and 55°

respectively. The distribution of slope values is shown in Figure 16. The histogram shows a bimodal distribution for the interior slopes, whereas the exterior slopes have the majority of values in the 70° slope bin. The included cumulative percentage plot on Figure 16 reflects this distribution, with 60% of the interior and only 30% of the exterior slopes falling below the AOR. Figure 17 shows the topographic profiles along strike for this ridge. As the DEMs created with 2828r.img and 2832r.img overlap, the difference plots of the two are compared in Figure 18. The difference plot represents the interior slope minus the exterior slope for each paired slope. Based on the difference plot, the southern half for both of the DEMs shows relative symmetry between interior and exterior slopes, while there is a clear trend in the exterior slope steepening so as to reduce the difference between the interior and exterior slopes for the northern ridge in 2832r.img. Generally the values for the northern interior and exterior slopes for 2832r.img are steeper than those for 2828r.img, but the values for the southern half are comparable to values for 2828r.img.

Banded Plains DEM 2825r.img - SOCET-SET

Nine profiles were taken along one double ridge (Figure 9). Values for interior and exterior slopes are listed in Table 7. Interior slopes range from 6 - 18°. Exterior slope values range from 4 - 20°. The distribution of slopes derived from this DEM is shown in Figure 19, with all interior slopes falling within 5 and 15°.. Most exterior slopes fall in the same range, but a few are higher than 20°. All of the interior and exterior slopes fall below the AOR. The average values for the interior and exterior slopes are 11.5 and 11.6°, respectively. The individual topographic profile lines for this double ridge are shown in Figure 20.

5.1.2 Cilix region: stereo pairs with 5013r.img (SOCET-SET and ASP)

Two images (7442r.img and 7542r.img) were used as stereo pairs with base image 5013r.img to generate two overlapping DEMs in SOCET-SET. These images feature double ridges located to the southwest and southeast of Cilix Crater (~2.0°N, 184.0°W), referred to as Cilix West and Cilix East, respectively. In SOCET-SET, 5013r.img was paired with 7442r.img. DEM resolution was set at 190 meters per pixel, with 500 meter profile spacing used for 7542r.img (Cilix East), and 1000 meter spacing used for 7442r.img (Cilix West).

The same base image was also used in ASP to generate DEMs with images 7442r.img (Cilix West) and 7446r.img to the south (also Cilix West). These images have lower resolution compared to the stereo pair images of the Banded Plains, and profiles were skipped if the number of data points were not sufficient (less than three data points) for extracting data. In most cases, profile data for the ridge exterior was sufficient for deriving surface slopes, while the data availability for the interior was variable.

Cilix West DEM 7442r.img - SOCET-SET

Eighteen profiles were taken along one double ridge (Figure 21). The profiles were split into two sections (Profiles 1-8 and 9-18), with only the upper section having sufficient points available for the calculation of interior slope angles, used to compare with the exterior values for symmetry. Values for interior and exterior slopes are listed in Table 8. Interior slope values range from 11 - 23°. Exterior slopes range from 6 - 14°. The distribution of interior and exterior slopes is shown in Figure 22, with the majority of values falling between 10 and 20° for both interior and exterior slopes, and no slopes exceeding the AOR (shown in the cumulative plots). The average slope for both interior and exterior slopes is 14°.

Cilix West DEM 7442r.img - ASP

Five profiles were taken along one double ridge (Figure 23). Profiles 1 to 5 overlap with profiles 3 to 7 for the SOCET-SET DEM of the same double ridge. Interior slopes were not derived for this ridge, as there were not sufficient interior points available. Exterior slopes range from 2 - 4°, with an average value of 3°. The slopes along trend are shown in Figure 24, with the comparison between the SOCET-SET DEM of the same ridge. The values for the western exterior slope for the ASP ridge are ~10° lower than the SOCET-SET DEM, with the differences between the eastern exterior slope values being greater.

Cilix West DEM 7446r.img - ASP

Eleven profile lines were taken along three double ridges (Figure 25). Interior slopes range from 6 - 23°. Exterior slopes range from 2 to 17°. Average values for the interior and exterior slopes are 12 and 8°, respectively. A histogram showing the distribution of interior and exterior slopes is shown in Figure 26, showing that no slopes exceed the AOR. Both the interior and exterior slope samples are centered around 5-15°, and there is a slight preference toward higher slope values for the interior slope histogram.

Cilix East DEM 7542r.img - SOCET-SET

Five profiles were taken along one double ridge (Figure 27). Values for the exterior slopes are listed in Table 9. Exterior slope values range from 8 - 17°, with an average value of 13°. Data points available along the topographic profiles were not sufficient to extract interior slopes for this ridge.

5.1.3 Slope Population Statistics

Eighty-five percent of the interior slopes derived from all eight of the DEMs fall below 45°, the hypothesized boundary (AOR) for double ridges created from cryo-sedimentary processes. A histogram of the total derived DEM slopes is shown in Figure 28, showing that 85% of the interior and 88% of the exterior slopes fall below the AOR. The mean values for the exterior and interior slopes are 24 and 30°, respectively. An unpaired t-test was used to compare the slope interior and exterior samples derived from the 8 DEMs as a first-order test to determine symmetry. The variance of the two samples was determined to be unequal using an f-test, so a t-test assuming unequal variances was chosen. The results of the t-test are described in Table 10. With the chosen value of α (0.05), the p value is sufficiently low to reject the null that these slope samples have equal means. Thus, they are not statistically similar in this case.

Symmetry is investigated further using paired t-tests between interior and exterior slopes (Table 11). Individual ridges were classified as symmetric if the p value was not sufficient to reject the null hypothesis of the t-test, that the mean difference between the two samples is different than zero. Symmetry is evident in four of the five ridge sections examined. The ridge featured in 2828r.img was split into northern and southern sections based on its difference plot (Figure18); the northern section appeared more asymmetrical than the southern section in this figure, which is supported by the statistical tests.

5.1.4 Summary of Results:

These results from analysis of DEMs can be summarized in the following observations:

- The majority of the interior slopes fall below 45°.

- Four of the five double ridge sections examined with paired interior and exterior slopes display symmetry based on statistical analysis.
- SOCET-SET and ASP DEMs created using the same stereo-pair images produced different slope values for overlapping profiles, which is discussed in more detail in Section 6.1.

5.2 Shadow Measurements

Forty individual ridges with defined relative age relationships were chosen for analysis, with a total of five regions examined. Interior slopes were calculated using both the exterior and interior shadow measurement techniques. On the following pages, each area is described textually, with accompanying figures and tables located in the Appendix.

For each area, five figures are presented:

1) Images used for analysis in the study area
2) Frequency vs slope angle
3) Frequency vs slope angle for the interior shadow length method plotted by age of the double ridges. For one area, this plot will also be shown for the exterior shadow length method as well.
4) Box plots of slope values with age. This is omitted for areas with only one age.
5) The difference between the results for the exterior and interior shadow length techniques plotted by age. For areas with one age, this plot is omitted.

5.2.1 Argadnel Regio

Three time divisions for double ridges were chosen for study in this region from geologic mapping done in Figueredo and Greeley, 2004. Nine images were used in this region to collect data from five Pwyllian (youngest), five Annwynian (middle), and six Argadnellian (oldest) ridges (Figure 29). The overall distribution of the slope sample shows that all interior slope values fall below 45° (Figure 30); the slope sample was then broken up into age groupings to note changes with age (Figure 31). Younger Pwyllian and Annwynian ridges are shifted toward slightly higher values, while the oldest Argadnellian ridges are centered near 20°. Average values for each age are 25.5°, 22.7°, and 18.6°, respectively. The modes obtained for each age are 29.5°, 24.2°, and 15.6°, respectively. The distributions of all three age groupings show overlap, but there is also a clear decrease in the median value for each age grouping for either technique used (Figure 32). The calculated difference between the interior and exterior shadow measurement techniques is shown in Figure 33, with the majority of values on this plot falling between -5 and 5°.

5.2.2 Bright Plains Region

Five images in this region had been mapped in previous work, with relative ages defined from cross-cutting relationships (Kattenhorn, 2002). Three time divisions for 10 ridges were selected for analysis: from youngest to oldest, they are the DR5, DR2, and DR1 age groups (Figure 34). The results show that all interior slope values fall below 45° (Figure 35). The slope sample was then broken up into the three europan time stratigraphic epochs for both the exterior and interior techniques to note changes with age (Figure 36). The exterior shadow length technique shows a decrease in slope with increasing age, whereas the interior technique shows a

more stacked distribution with the middle time step having the highest slope values overall. Average values for each age are 17.0°, 22.9°, and 16.5°, for D5, D2, and D1, respectively, for the interior technique. The modes obtained with the interior technique for each age are 19.4°, 26.8°, and 12.8°, respectively. Overlap is apparent among all three age groups, with the box plots of these data showing the shallow values obtained from the interior shadow length technique for the youngest ridges in the region (Figure 37). The calculated difference between the two shadow measurement techniques is shown in Figure 38. The majority of values on this plot fall between -10° and 10°; however, the values for DR5 plot well below 0° in most cases.

5.2.3 Southern Annwyn Regio (5°N, 327°W)

Two time divisions for five ridges were chosen in this region from geologic mapping done in Spaun et al. (2003). Profiles taken along ridges A-E are shown in Figure 39, with ridge C defined as the youngest, and A, B, D, and E defined as older than C via cross-cutting relationships. The overall distribution for both techniques is shown in Figure 40. Most values fall below 45°, although a portion of the interior slopes calculated with the interior technique are higher than the AOR (~22%). All of the slope calculated with the exterior technique fall below the AOR. Average values for each age are 45.1° and 35.6°, for C and ABDE, respectively, for the interior technique. The modes obtained for each age are 40.2° and 48.0°, respectively. The box plots of these data show the anomalously high outliers that exist in this region (near 60° for the youngest ridge) (Figure 41). The calculated difference between techniques is shown in Figure 42. Most values lie between 0-20°, with values for ridge C falling within the same range of values as ridges A, B, D, and E.

5.2.4 Other Pwyllian Ridges

Four of the double ridges analyzed are located in the northern hemisphere (40°N, 148°W, near Tyre Crater). These ridges have been defined as Pwyllian based on geologic mapping done by Bunte et al. (2013), with individual profiles shown in Figure 43. Five other Pwyllian ridges are analyzed in the southern hemisphere (45-60°S, 160-180°W), as defined as such in mapping by Bunte et al. (2013). Individual profiles for these ridges are shown in Figure 44.

The distributions of slopes for the northern and southern ridges for both techniques are shown in Figures 45 and 46, respectively. All of the slopes derived from both techniques in the northern hemisphere fall below the AOR (Figure 45). All of the slopes derived from the interior technique in the southern hemisphere fall below the AOR, while one of the 35 slopes (~3%) lies above the AOR for the exterior technique. The distributions comparing values derived for the interior technique in both regions are shown Figure 47. The average values for each sample are 20.2 and 31.2°, respectively. All of the interior slope values obtained from these young ridges also fall below 45°. A difference plot of the interior and exterior shadow length techniques is shown in Figure 48. For the northern ridges, most values lie between ±5°. The ridges in southern latitudes have higher values, with the majority of values being greater than 0°.

All of the youngest ridges examined (defined as Pwyllian by Greeley et al. (2004) and Bunte et al. (2013)) have interior slopes that fall within the hypothesized values for cryovolcanism or tidal squeezing (Figure 49). Most values fall between 15 and 35°. Average values for all of the Pwyllian interior slopes are 23.6 and 25.7° for the exterior and interior techniques, respectively.

5.2.5. Summary of Results:

The results from shadow length measurements can be summarized in the following observations (Table 12, Appendix):

- Collectively, the frequency vs. slope plots have interior slopes shallower than 45°, although interior slopes reach up to 60° in one region.
- The plots of frequency vs slope angle by age and average slope by age both show in general a trend of decreasing slope with age for the majority of the locations analyzed and techniques used (individual results are shown in Table 12).
- The plots of the difference between the results for the two different techniques show complicated results that vary with area (and even location within the area).
- The variability in these results suggests either that gaps are variably present on Europa, or that the assumptions of the two techniques do not hold. This may especially be true for the DR5 age group in the Bright Plains region, which are the only ridges that are inferred to have interiors that are superimposed based on their difference plot (Figure 38).

6. Discussion

In this section, I first compare results from overlapping DEMs created with ASP and SOCET-SET. I then discuss which group of mechanisms for double ridge formation is more viable, given results from both the DEM and shadow length technique slope values. A unique case within the Banded Plains has steeper slopes than were derived for the other study regions, and so does not fit neatly into the same group of formation mechanisms. I then discuss the change in slope morphometry over time as seen in the shadow measurement results and describe why mass wasting is unlikely to be a controlling influence on these results. The presence or absence of a gap between ridge sets is discussed in Section 6.6, along with the implications for each possible scenario. Finally, I conclude with a discussion of the subsurface implications of the results presented in this work.

6.1 Comparison of ASP and SOCET-SET DEMs

The use of two different techniques to generate DEMs with stereo-pair images allows me to make some comparisons about the two techniques. These two techniques were applicable for DEMs created with two sets of stereo pairs: 2828r.img and 3800r.img (Figures 9 and 13 for SOCET-SET and ASP, respectively) in the Banded Plains, and 7442r.img and 5013r.img (Figures 21 and 23 for SOCET-SET and ASP, respectively) for Cilix West. For the Banded Plains double ridge, the slopes for both techniques along overlapping profiles are shown in Figure 15. For the Cilix West DEMs, five overlapping profile lines are compared in Figure 24.

For the Banded Plains double ridge, comparison between slopes from the SOCET-SET and ASP DEMs shows mixed results (Figure 15). The interior slope values for both the northern and southern ridge sections are generally steeper in the SOCET-SET DEM than in the ASP

DEM. Conversely, the exterior slopes in the SOCET-SET DEM are ~10-15° shallower along the northern ridge than in the ASP DEM. For the ASP DEM, the values for the southern ridge exterior slopes appear to increase along strike from 7 to 67°, whereas for the SOCET-SET DEM, the data generally lie between 25 and 35°.

Comparison of the Cilix West DEMs was limited to exterior slopes, as the interior slopes lacked sufficient data points for the ASP DEM (see Section 5.1.2). In addition, ASP was unable to derive topography for a large section of the overlap area, (as shown in the western half of the DEM in Figure 23), which limited data collection along the southern section of the ridge examined in the SOCET DEM. For the section of the Cilix West double ridge that could be compared, the results are both more consistent than for the Banded Plains comparison and also show distinct differences between the slopes. The exterior slope values from the SOCET-SET DEM are always steeper than those from the ASP DEM, typically by 10° to 15° (Figure 24). The ASP DEM slopes are quite shallow, as low as 2° for one profile. However, the two different Cilix West DEMs are also consistent in that the exterior slopes for the western section of the ridge are slightly steeper than the eastern section for both techniques.

For this work, more confidence was placed in using the SOCET-SET DEMs for analysis, because manual editing of the DEMs was possible. For example, the ASP DEM of 2828r.img shows some spiky areas along the southern half of the ridge that were later determined to be DEM errors while editing within SOCET-SET. Using the SOCET-SET DEM for 7442r.img was also more practical, as it was able to pick up more data points along the interior to enable slope measurements, whereas the ASP DEM was lacking sufficient data to generate good pixels along the interior of the Cilix West region. Being able to compare the two techniques over a terrain

with known topography from an independent source would be ideal to better assess the strengths/validity of using either technique.

6.2 Supported Formation Mechanisms: Cryo-sedimentary Processes

A total of 44 double ridges were examined in this study using the two different techniques of stereo pair DEMs (only SOCET SET values are reported below, as explained in section 6.1) and shadow measurements (4 and 40 double ridges examined per technique, respectively). Of these, the majority (80%) of the 353 derived interior slopes from the SOCET-SET DEMs fall below 45°. Almost all of the slope values from the shadow measurement techniques are also below the AOR used in this work of 45° (97% of 301 slopes for the interior shadow measurement technique), with the exception of one ridge of the 40 examined with this technique that had slopes near 60°. If the AOR for europan ice particles is less than the value I've used in this work, then a slightly smaller supermajority of slopes would fall below the AOR. Specifically, if I used 40 degrees instead, 68% of the slopes from the SOCET-SET DEMs would be below AOR, whereas 93% and 99% of the data would be below AOR for the interior and exterior shadow measurement techniques, respectively. Therefore, the majorities shown indicate that these conclusions should be robust against this slight uncertainty for the AOR.

Overall, these results for the interior slope angle are consistent with formation by cryo-sedimentary mechanisms and inconsistent with formation by brittle deformation mechanisms. Symmetry between double ridge interior and exterior slopes as derived from SOCET SET DEMs is also dominant, with four of the five examined ridge sections being symmetric (Table 11). Symmetry is expected for the explosive cryovolcanic formation mechanism, with piles of granular ice being deposited near the central vent. Effusive cryovolcanism or tidal squeezing

may also produce symmetric slopes. Strong asymmetry is expected for each of the three brittle deformation mechanisms, with the exterior slopes expected to be much shallower than the interior. Thus, the large majority of my slope data favor cryo-sedimentary formation of double ridges over formation from brittle deformation mechanisms, with symmetry also supporting cryo-sedimentary mechanisms, namely explosive cryovolcanism.

Although symmetry is inferred to be most consistent with explosive cryovolcanism, the other cryo-sedimentary mechanisms could also be consistent with self-symmetric double ridges (Figure 4), and could co-occur with explosive volcanism. Several driving forces could be responsible for explosive eruptions of cryomagma, each of which requires overcoming the negative buoyancy of the cryomagma (water) compared to the surrounding ice layer. Possible driving forces include pressurization of the cryomagma or the inclusion of materials or volatiles that increase its buoyancy compared to ice (Fagents et al., 1998). Pressurization could be achieved via partially freezing a reservoir of cryomagma within the crust (Fagents, 2003). The inclusion of materials such as ammonia may increase the buoyancy of the cryomagma and aid surface eruption, although materials other than sulfates ($MgSO_4$ or Na_2SO_4) are not thought to exist in high quantities (Fagents, 2003). The exsolution of volatiles such as water vapor, SO_2, and CO_2 could also decrease the cryomagma density and enable an explosive eruption (Kadel et al. 1998; Fagents et al., 2000).

Similar driving forces are also involved in the other two cryo-sedimentary processes. As opposed to explosive cryovolcanism, effusive cryovolcanism would result in flows of cryolava being deposited on the surface instead of granular ice particles (Fagents et al., 2003). Like explosive cryovolcanism, this effusive style may also be driven by the exsolution of a cryomagma but one that is less rich in volatiles (Kadel et al., 1998; Fagents, 2003). Thus, these

two types of cryovolcanism could co-occur based on close spatial variation in the volatile content (Kadel et al., 1998), or could occur in the same area sequentially in time, as a function of volatile content variability. The viscosity of the cryomagma may also play a role in the type of eruption occurring, with more viscous magma resulting in a greater pressure build up and more explosive eruptions, as in silicate eruptions (Giordano et al., 2008). The viscosity of europan cryolavas is uncertain, and this parameter has been varied widely in modeling of effusive flows specifically (Fagents, 2003), but both more and less viscous magmas are possible.

Along with the two cryovolcanic mechanisms, tidal squeezing could also be co-occurring or interleaved in time with cryovolcanism. Tidal squeezing involves the opening of fractures to pump ice and slush to the surface, and these fractures could penetrate into existing reservoirs of cryomagmas within the crust (Greenberg et al., 1998). High pressures or large amounts of volatiles facilitate the transport of material through the fractures to the surface. Conversely, effusive cryovolcanic eruptions of ice or slush could also be aided by tidal squeezing, as the opening and closing of conduits on diurnal timescales would pump more material to the surface.

In summary, these results best support cryo-sedimentary processes, with interior and exterior slope symmetry best supporting explosive cryovolcanism as the dominant shape-former for double ridges. However, other cryo-sedimentary processes such as effusive cryovolcanism or tidal squeezing could also be co-occurring, depending upon the volatile content or tidal stresses experienced during eruption. Data returned from future missions to Europa involving observations of an actively forming ridge over time could indicate whether these processes are coeval.

6.3 Possible Formation Mechanisms within Banded Plains

Twenty percent of ridge slope values derived from the SOCET-SET DEMs exceed the posited AOR for cryo-sedimentary formation mechanisms. These slope values are all located along one double ridge in the Banded Plains (shown in the 2828r.img and 2832r.img DEMs; Figure 9). The steeper than AOR slope values suggest formation via brittle deformation. However, this double ridge achieves symmetrically steep slopes, which is not expected via the three brittle deformation mechanisms discussed previously, as rollback of the vertical fracture would produce a steep interior slope but not steeper angles than 45° for both interior *and* exterior slopes (e.g., Figure 2). Symmetrically steep interior and exterior angles could possibly be achieved via welding of cryovolcanic particles, a mechanism suggested by Kadel et al. (1998) for locally steeper exterior slopes they found in their work. However, it is unclear how this process could produce slopes in excess of 60°, as seen in this work. Symmetrically steep slopes (~60°) have been achieved in laboratory experiments for natural snow crystals (Kuroiwa et al., 1967). Very steep slopes (near 90°) can be achieved for pulverized snow crystals if the particle temperatures are increased to near their melting point, where a liquid film can develop and attract particles to one another (Kuroiwa et al., 1967). This process results in the material having a shallower AOR near its base, with the top becoming quite steep, producing a chimney-like feature in the center (Kuroiwa et al., 1967). However, this result occurs on the centimeter scale in laboratory studies, and might not scale to features hundreds of meters tall such as double ridges. It also depends on the presence of thin films, which occur under terrestrial conditions. The development of thin films seems less likely to occur on Europa, given its frigid surface temperatures ranging from 80-140K (Spencer et al., 1999). Thus, the formation of steep slopes by this mechanism seems unlikely.

The very steep (~60-70° in some places) interior slopes along the northern half of this double ridge could be explained by post-formation modification, either by strike-slip faulting or as a mass wasting head scarp. Strike-slip faulting could result in the steepening of one half of the double ridge set (Sylvester, 1988), if the vertical fault propagated into one half of the ridge. This configuration could result in the other half being shallower, consistent with my data of this double ridge (Figure 15). There are not any clear indicators of lateral motion occurring between these ridge sets, however, in the stereo pair images (2828r.img and 2832r.img; Figure 10). Mass wasting head scarps are typically steep slopes that are upward-convex, with hummocky debris deposits (Hovius et al., 1998). The topographic profiles for this ridge in Figure 12 do not appear to be convex, although there may not be sufficient data points to determine how arcuate this profile truly is. Individual profiles do show variation in the slope steepness along the northern half (Figure 12), although the limited number of data points also makes it difficult to state whether there is a slump feature along the interior profile. It is possible that elevated feature in the center of the profiles in Figure 12 could be some sort of debris deposit if this is a mass wasting head scarp. This individual ridge appears unusually sinuous along strike, which could lend support to post-emplacement modification occurring such as episodes of debris movement. The two halves of the double ridge also have differing heights, further suggesting some type of modification might have occurred in its history. Thus, whereas post-formation modification is often considered to shallow slopes (see Section 2.2), the data from this location in the Banded Plains raises the possibility of post-formation modification that may steepen slopes. Of the several possibilities for the formation of this steep interior, a mass wasting scarp may be the most likely option, given that the topographic profiles show what could be a scarp face and a pile of debris in the center of the double ridge.

6.4 Double Ridge Morphometry Over Time

The change in double ridge morphometry over time is also investigated, with these results summarized in the second column of Table 12. Each of the five regions examined in this work had defined relative ages. As no absolute ages exist for these double ridges, I am limited to using only these relative ages determined via cross-cutting relationships to determine whether their morphometry is changing with time.

Of the three time divisions investigated in Argadnel Regio (mapped in Figueredo and Greeley, 2004), both the mean and mode values decrease from the youngest to oldest double ridges. Likewise, a steady decrease in the median value is shown in the box plots for these data (Figure 32). This result holds true for both the interior and exterior shadow length techniques shown in this figure. These observations of interior slope decreasing over time are supported by the statistically significant difference between each age group in this region. For southern Annwyn Regio (mapped in Spaun et al. 2003), only two time divisions were identified from cross-cutting relationships. The youngest time step does have a steeper mean value (~10° higher) for the interior shadow length technique, although slope data from this more recent age is limited to a single ridge in this region. For the double ridges mapped in the Bright Plains Region (Kattenhorn 2002), the interior shadow length technique has the middle time step (DR2) as the steepest, whereas the exterior shadow length technique shows a clear decrease in slope as the time steps increase in age (Figures 36 and 37). However, data from both interior and exterior techniques in this region agree that the oldest time step (DR1) has the shallowest slope values. This area does have a background terrain that appears quite rough and may warp exterior shadows; therefore, the interior shadow length technique may be a better indicator of age relationships.

For other double ridges mapped as Pwyllian in Bunte et al. (2013), the mean slope values are 20.2 and 31.2°, respectively, for double ridges mapped in the northern and southern hemispheres (Figures 43 and 44). The steeper interior slopes in the southern hemisphere for the same age grouping may suggest that these double ridges formed more recently than those in the north (Figure 46). The values derived for ridges in the northern hemisphere are typically shallower, and more comparable to other Pwyllian ridges mapped in Argadnel Regio. The results for both regions are generally steeper than the Annwynian and Argadnellian values derived in Argadnel Regio.

Overall, these results show a decrease in slope with age. The modification processes of sputtering or sublimation would not shallow these slopes appreciably over Europa's surface age (see Section 2.2). Mass wasting is a known modification process as indicated by morphologies interpreted as terraces or grooves along the interiors of some double ridges (Head et al., 1999). In my study areas, the double ridge shown in the 2828r.img DEM in the Banded Plains may have a terrace along its northern half (shown in the topographic profiles in Figure 12) and one degraded-looking double ridge in Argadnel Regio, R5 (Figure 29), has shallower slopes on average compared to other ridges within its age grouping (~15-20°). No other mass wasting features are visible at the resolution of the images in my study areas, but both of these ridges appear sinuous along trend compared to the majority of straight ridge sections, which would be consistent of episodic debris movement. And Androgeos Linea, the most prominent double ridge in the Bright Plains region (DR5 age group; Kattenhorn (2002)) shows vertical lineations along its interior that may be grooves or lanes of sediment. Thus, I conclude that the most likely mechanism for shallowing of double ridge slopes with time is mass wasting.

6.5 Influence of Mass Wasting on Inferences of Formation Mechanisms

Based on the results discussed in Section 6.2, the overwhelming majority of the data support cryo-sedimentary mechanisms for double ridge formation. During the collection of these data, care was taken to avoid measuring obvious mass wasting features. Thus, although these slopes could have been modified to some degree, mass wasting would not significantly influence the conclusions derived here.

The limited influence of mass wasting on slope values is supported by the tests for symmetry: the symmetry between interior and exterior slopes seen in the DEM profiles would not be seen for double ridges created from brittle deformation processes, which are expected to be strongly asymmetric. The formation of the observed symmetric and near-AOR slopes from such strongly asymmetric slopes as would be formed by brittle deformation would require steepening the exterior slopes instead of shallowing them. However, the process of mass wasting would tend to shallow slopes over time, not steepen them. Mass wasting of both the asymmetric interior and exterior slopes would shallow both slopes over time, which would not produce symmetry until extremely low angles were obtained for both interior and exterior slopes. However, my results show moderately steep or near-AOR slopes with symmetry. It is thus morphologically less likely to produce two symmetric slopes at or near the AOR via mass wasting when they initially form as strongly asymmetric, with one slope being much less than the AOR. From this, symmetry is more strongly in support of cryo-sedimentary formation mechanisms for double ridges, namely explosive cryovolcanism.

6.6 Presence of Gaps between Double Ridges

The interiors of double ridges are enigmatic, given that they are heavily shadowed in Galileo satellite images. Determining whether gaps exist between ridge sets is crucial to accurately calculating the interior slopes of double ridges. If a gap does not exist, both techniques used in this work should produce similar results. If a large gap exists, as seen in DEMs like 2828r.img, the exterior shadow length technique will underestimate the interior slope (sometimes severely so). For example, the double ridge shown in Figure 44 in image 0213r.img clearly has a gap between the two ridges. The exterior shadow length technique produces slopes near 10°, while the interior shadow technique typically gives values between 15-30° (with one profile reaching 39°). This underestimation of the slope values would have a significant effect on the resulting interpretation of morphology if the interior was in shadow, as is seen in the majority of Galileo SSI images.

The exterior and interior shadow length techniques were compared to make inferences on double ridge interiors, i.e., whether the two ridge sets had a gap existing between them. For the interior slope sample of 40 double ridges, the mean value derived from the exterior shadow length technique is slightly shallower than the interior shadow length technique (19.6 and 23.1°, respectively). This positive difference between the mean interior slope values derived from the interior shadow technique (which does not account for a gap) and from the exterior shadow technique (which does account for a gap) may be suggestive of a gap existing within the majority of these ridge sets, although the sample means are within error of one another. Looking at individual regions, the difference plot for Argadnel Regio shows the slopes derived from the two techniques being relatively similar (within ±5°). Individual profiles show a slight preference for higher values for each of the three age groupings, with the majority of the difference data falling

above zero (i.e., steeper interior slopes) for each age grouping examined. For the Bright Plains region, the majority of values for the older ridges (DR2 and DR1) plot within ±5°, while the values for the youngest ridge (DR5) plot well below zero in most cases. That is, my data for the youngest double ridge show steeper interior slopes values from the technique that does not account for a gap than the technique that does account for a gap. These relative values from the two different shadow techniques may be indicative of the interior slopes of the youngest ridges in this region being superimposed on one another (Table 3), as opposed to having a gap between them. For difference plots in southern Annwyn Regio, the majority of data points cluster above zero (76%), suggesting that a gap exists between most of these ridge sets. Four Pwyllian ridges in the northern hemisphere tend to lie within ±5° on a difference plot of the techniques, while the majority of ridges in the southern hemisphere plot above 5°. This preference for high values may also suggest the presence of a gap is more common for the double ridges located in southern latitudes.

The presence or absence of a gap could serve as a geologic indicator, suggesting a formation mechanism for a given double ridge. For instance, ridges created via brittle deformation mechanisms involve the upwarping of the crust, with the ridge sets touching in the center, closing the fracture. However, post-formation processes could also determine the presence or absence of a gap. For example, one scenario to explain the presence of a gap would be extension occurring after ridge formation. This general scenario is supported by the fact that extensional features are ubiquitous on Europa, while compressional features such as folds appear to be more scarce (e.g., Prockter and Pappalardo, 2000). This model of post-emplacement extension is also supported by cryo-sedimentary mechanisms which require extension to create a central conduit to facilitate eruptions. As discussed above, extension could result from tidal

deformation of Europa's icy crust occurring on diurnal timescales (Kattenhorn and Hurford, 2009). Ridges could form with superposed or touching interior slopes as a result of compression after ridge formation. This scenario is favorable in that it could account for surface contraction to balance the wealth of extensional features seen on Europa (Kattenhorn and Hurford, 2009). The notion that double ridges could accommodate a portion of this missing contraction has also been suggested recently based on displacement measurements (Culha et al., 2014). As described below, plate tectonism could be occurring on Europa (Prockter and Kattenhorn, 2014), which could result in compression.

However, another cause for the difference between the interior slope values derived from the two different shadow techniques could be that the two techniques have different assumptions, as explained previously; the interior technique assumes equal ridge heights, whereas the exterior technique assumes that the interior slopes touch at the midpoint between the ridges. Thus, the difference in slope values derived from the two techniques could also point to locations where these assumptions are not met. Future images and topography from Europa could be used to test these two assumptions, or even measure directly the presence or absence of a gap, and thus provide evidence for or against the above two scenarios. Future modeling work centered on double ridge formation could also help indicate whether the presence of a gap could be diagnostic of a given formation mechanism.

6.7 Implications for the Subsurface

Based on the slopes derived from both techniques for the 44 ridges examined, the null hypothesis is supported, that these double ridges are created from cryo-sedimentary mechanisms such as cryovolcanism (explosive or effusive) or tidal squeezing. The prevalence of symmetry

supports explosive cryovolcanism as the dominant shape-forming mechanism. These cryo-sedimentary mechanisms could suggest direct communication between the surface and the europan ocean below. This could be achieved via a central conduit or fracture penetrating through the crust. Other configurations of cryomagma within the crust are anticipated to exist as well, such as conduits that are capped instead by a lateral body of water, or sill (Collins et al, 2000). Sills could be sourced by the ocean below, or from other localized lenses of water within the crust (Fagents et al., 1998; Michaut and Manga, 2014). Localized pockets of water within the crust have been hypothesized to form features such as chaos terrain on Europa, and may exist at depths as shallow as 3km (Schmidt et al., 2011).

A thin outer ice shell would be preferable for cryomagma ascent, as the ascent time would need to be minimized to prevent freezing of the cryovolcanic conduit or fracture prior to eruption (e.g. modeling by Turtle et al., 1998a). However, numerical modeling suggests that eruption onto the surface *is* possible at depths of up to 100km (Wilson and Head, 1998). Because of the negative buoyancy of liquid water compared to the icy shell, pressurization of the ocean alone may not be sufficient to drive eruptions (Manga and Wang, 2007), but partial freezing of discrete water reservoirs within the ice layer may generate enough pressure to drive surface eruptions (Fagents, 2003). The results of this study could support the hypothesized existence of water lenses underneath chaos terrain (Schmidt et al., 2011), in that the ridges in the Bright Plains (within Conamara Chaos) all exhibit interior slopes below the AOR, favoring cryo-sedimentary formation.

Plate subduction on Europa is evidence for a thicker ice shell, as described in Kattenhorn and Prockter (2014), which necessitates a ductile layer that would increase the total crustal thickness. There is evidence that plate subduction is occurring distal to Argadnel Regio

examined in this work, with subsumption bands well to the north (Kattenhorn and Prockter, 2014). Plate subduction may be more beneficial in generating melt for cryovolcanic processes than a thin-shell model alone. The presence of a thicker ice shell may be better able to accommodate significant water reservoirs as well (Pappalardo, 2000).

7. Conclusions

The goal of this work was to expand upon our knowledge of europan double ridges as well as test between proposed double ridge formation hypotheses. My tool to achieve this goal was examination of double ridge morphology using multiple techniques. Existing formation hypotheses were split into two groupings that reflected expected interior slope values and, secondarily, symmetry between interior and exterior slopes. Forty-four double ridges were investigated, with study areas chosen based on established relative age relationships and availability of Galileo SSI stereo-pair images. Both results from DEMs and shadow measurement techniques are in agreement that double ridges generally have shallow interior slopes (less than 45°). These results support the null hypothesis of this work, suggesting that cryo-sedimentary processes such as cryovolcanism or tidal squeezing are more likely to form these double ridges than brittle deformation mechanisms such as linear diapirism. Symmetry is seen between the interior and exterior slope pairs for four of the five double ridge sections examined in the DEMs. This is more supportive of cryo-sedimentary mechanisms, as modification of double ridge slopes created via brittle deformation slopes should maintain their asymmetry. Double ridges with defined relative ages in Argadnel Regio show a clear trend of shallowing over time. This trend is not as clear in other regions, although the oldest ridges in each region examined tend to be the most subdued, with the shallowest interior slopes. Finally, comparisons between the two shadow length techniques show that most values derived from the interior shadow length technique are either close to those of the exterior shadow length technique, or are higher. This comparative result suggests that a gap exists between these double ridge sets. Shallowing of slopes over time could be explained from mass wasting of double ridge interiors. While morphometry alone cannot fully explain double ridge formation histories, it can

be a good first indicator of which of the many existing formation hypotheses are most viable. In this case, existing hypotheses involving either a thin ice shell or an ice shell with water lenses, such as cryovolcanism or tidal squeezing, are better supported by my data than brittle deformation processes in the formation of these ubiquitous features.

Nine science instruments have been selected for an upcoming NASA mission to Europa expected to launch in the 2020's (Chou and Cantillo, 2015). This suite of instruments will be vital for testing the results of this and other studies that have utilized Galileo spacecraft data to investigate Europa. One instrument, the Europa Imaging System (EIS), will have both narrow and wide angle cameras. It will produce a global map with higher-resolution images (4 times better than the lowest resolution Galileo SSI camera images used in this work, and 100 times better than images in other regions), which would enable more precise measurements for the shadow length techniques in this work. This improvement in precision would in turn produce more robust slope data for testing my hypotheses. The high-resolution thermal instrument on the spacecraft (Europa Thermal Emission Imaging System (E-THEMIS)) could detect areas of active cryolava eruption on the surface. The ice penetrating radar onboard (Radar for Europa Assessment and Sounding: Ocean to Near-surface (REASON)) could detect the depth to liquid water and determine whether localized water reservoirs exist within the crust. Thus, these data returned from this mission would be invaluable for further investigating the formation of double ridges and the wealth of unique surface features we see on Europa.

References

Anderson et. al., 1997. Europa's differentiated internal structure: inferences from two Galileo encounters. Science, v. 276, p. 1236- 1239.

Bader, C. E., Kattenhorn, S.A., and Schenk, P.M., 2008. Topographic Analysis of Europa's Ridges. AGU Fall Meeting 2008, Abstract #P23A-1349.

Bandukwala, F., 2011. Extracting spatially and spectrally coherent regions from multispectral images. Proceedings of the Institute of Electrical and Electronic Engineers' Computer vision and Pattern Recognition Workshop (CVPRW) 2011, p. 82-87.

Belton, M.J.S., et al., 1996. Galileo's first images of Jupiter and the Galilean satellites. Science, v. 274, p. 377–384.

Belton, M.J.S., and Galileo Team, 2000. Results of the Galileo solid state imaging (SSI) experiment. Advances in Space Research, v. 26, p. 1641–1647.

Bierhaus, E. B., Chapman, C. R, and Merline, W. J., 2005. Secondary craters on Europa and implications for cratered surfaces. Nature, v. 427(20), p. 1125–1127.

Bierhaus, E.B., Zahnle, K., and Chapman, C.R., 2009. Europa's crater distributions and surface ages. In *Europa* (ed. R.T. Pappalardo, W.B. McKinnon & K.K. Khurana, Univ. Ariz. Press), p. 161-180.

Bray, V.J., Collins, G.S., Morgan, J.V., Melosh, H.J., and Schenk, P.M., 2014. Hydrocode simulation of Ganymede and Europa cratering trends – How thick is Europa's crust? Icarus, v. 231(1), p. 394-406

Bunte, M.K., et al., 2013. Exotic Europa: Global Geologic Map as a Reference for Future Study. GSA Fall Meeting 2013, Abstract #226021 (poster).

Carlson, R.W., et al. 2009. Europa's Surface Composition. In *Europa* (ed. R.T. Pappalardo, W.B. McKinnon & K.K. Khurana, Univ. Ariz. Press), p. 283-327.

Chou, F., and Cantillo, L., 2015. NASA's Europa Mission Begins with Selection of Science Instruments [Press Release]. Retrieved from http://www.nasa.gov/press-release/nasa-s-europa-mission-begins-with-selection-of-science-instruments

Collins, G. C., Head, J.W., Pappalardo, R.T. and Spaun, N.A., 2000. Evaluation of models for the formation of chaotic terrain on Europa, J. Geophys. Res., v. 106, p. 1709– 1716.

Collins, G.C., McKinnon, W.B., Moore, J.M., Nimmo, F., Pappalardo, R.T., Prockter, L.M., and Schenk, P.M., 2008. Tectonics of the Outer Planet Satellites. In *Planetary Tectonics* (ed. T. Watters, R. Schultz, Cambridge University Press, Cambridge, UK), p. 1-43.

Cooper J. F., Johnson R. E., Mauk B. H., Garrett H. B., and Gehrels, N. 2001. Energetic ion and electron irradiation of the icy Galilean satellites. Icarus, v. 149, p. 133–159.

Coulter, C.E., 2010. Kinematic and Morphological Evolution of Europa's Ridges. Unpublished master's thesis. University of Idaho, Moscow, Idaho.

Coulter, C.E., and Kattenhorn, S.A., 2010. The morphology of Europa's ridges examined in a detailed topographic and kinematic survey. AGU Fall Meeting 2010, Abstract #P21B-1599.

Craft, K.L, Patterson, G.W., and Lowell, R.P., 2013. Sill emplacement in Europa's ice shell as a driving mechanism for double ridge formation. Lunar Planet. Sci. XLIV, Abstract #3033

Culha, C., et al., 2014. Double ridges on Europa accommodate some of the missing surface contraction. J. Geophys. Res.: Planets, v. 119, p. 395-403.

Dombard, A. J., Patterson, G.W., Lederer, A.P., and Prockter, L.M., 2013. Flanking Fractures and the formation of double ridges on Europa. Icarus, v. 223, p. 74-81.

Fagents, S.A., Kadel, S.D., Greeley, R., Kirk, R.L., and the Galileo SSI team, 1998. Styles of cryovolcanism on Europa: Summary of evidence from the Galileo nominal mission. Lunar Planet. Sci. XXIX., Abstract #1721.

Fagents, S.A., Greeley, R., Sullivan, R.J., Pappalardo, R.T., Prockter, L.M., and the Galileo SSI team, 2000. Cryomagmatic mechanisms for the formation of Rhadamanthys Linea, triple band margins, and other low-albedo features on Europa. Icarus, v. 144, p. 54–88

Fagents, S. A., 2003. Considerations for effusive cryovolcanism on Europa: The post-Galileo perspective, J. Geophys. Res., v. 108, E125139.

Figueredo, P.H., and Greeley, R., 2004. Resurfacing history of Europa from pole-to-pole geological mapping. Icarus, v. 167, p. 287–312.

Friedman, S. P., and Robinson, D. A., 2002. Particle shape characterization using angle of repose measurements for predicting the effective permittivity and electrical conductivity of saturated granular media. Water Resources Research, v. 38(11), 1236, doi:10.1029/2001WR000746

Gaddis, L., et al., 1997. An overview of the integrated software for imaging spectrometers (ISIS). Lunar Planet. Sci. XXVIII, Abstract #387.

Geissler, P. E., et al. 1998c. Evolution of Lineaments on Europa: Clues from Galileo multispectral imaging observations, Icarus, v. 135, p. 107-126.

Giordano, D., Russell, J.K., and Dingwell, D.B., 2008. Viscosity of magmatic liquids: a model. Earth and Planetary Science Letters, v. 271, p. 123–134.

Greeley, R., et al., 1998. Europa: Initial Galileo Observations. Icarus, v. 135, p. 4 – 24.

Greeley, R., Chyba, C.F., Head, J.W., McCord, T.B., McKinnon, W.B., Pappalardo, R.T., and Figueredo, P., 2004. Geology of Europa. In *Jupiter* (eds. F. Bagenal, T.E. Dowling, W.B. McKinnon, Cambridge University Press, Cambridge, UK), p. 329–362.

Greenberg, R. et. al. 1998a. Tectonic processes on Europa: Tidal stresses, mechanical response, and visible fractures. Icarus, v. 135, p. 65-78.

Greenberg, R., and Sak, P.B., 2014. The ridges of Europa: Extensions of adjacent topography onto their flanks. Earth and Planetary Science Letters, v. 389, p. 43-51.

Head, J.W., Pappalardo, R.T., and Sullivan, R., 1999. Europa: Morphological characteristics of ridges and triple bands from Galileo data (E4 and E6) and assessment of a linear diapirism model. J. Geophys. Res. v. 104, E10, p. 24223-24236.

Hobley, D.E.J., Moore, J.M., and Howard, A.D., 2013. How rough is the surface of Europa at the lander scale? LPSC XLIV, Abstract #2432

Hoppa, G.V., Tufts, B.R., Greenberg, R., and Geissler, P., 1999a. Strike-slip faults on Europa: Global shear patterns driven by tidal stress. Icarus, v. 141, p. 287–298.

Hoppa, G. V., Tufts, B.R., Greenberg, R., and Geissler, P.E., 1999b. Formation of cycloidal features on Europa. Science, v. 285, p. 1899–1902.

Hovius, N., Stark, C.P., Tutton, M.A., and Abbott, L.D., 1998. Landslide-driven drainage network evolution in a pre-steady-state mountain belt: Finisterre Mountains, Papua New Guinea. Geology, v. 26, p. 1071–1074.

Jackson, M.P., Vendeville, B., 1994. Regional extension as a geologic trigger for diapirism. Geol. Soc. Am. Bull., v. 106, p. 57 – 73.

Kadel, S.D., Fagents, S.A., Greeley, R., and Galileo SSI Team. 1998. Trough-bounding ridge pairs on Europa – considerations for an endogenic model of formation. LPSC XXIX, 1078-1079.

Kargel, J. S., S. K. Croft, J. I. Lunine, and J. S. Lewis 1991. Rheological properties of ammonia–water liquids and crystal–liquid slurries: Planetological implications. Icarus, v. 89, p. 93–112.

Kargel, J.S., et al., 2000. Europa's crust and ocean: Origin, composition, and the prospects for life. Icarus, v. 148, p. 226–265.

Kattenhorn, S. A., and Hurford, T., 2009). Tectonics of Europa. In Europa (eds. R. T. Pappalardo, W. B. McKinnon, and K. K. Khurana, Univ. Arizona Press, Tucson, AZ), p. 199–236

Kattenhorn, S.A., (2002). Nonsynchronous rotation evidence and fracture history in the Bright Plains region, Europa. Icarus, v. 157, p. 490–506.

Khurana, K.K., et al., 1998. Induced magnetic fields as evidence for subsurface oceans in Europa and Callisto. Nature, v. 395, p. 777-780.

Kirk, R. L., 1987. III. A fast finite-element algorithm for two-dimensional photoclinometry, Unpublished Ph.D. thesis. Caltech, Pasadena, California. pp. 165–258.

Kirk, R. L., 2003. ISIS Photoclinometry User Guide. <digitalcorpora.org/corp/nps/files/govdocs/313/313845.pdf>

Kirk, R.L., Barrett, J.M., Soderblom, L.A., 2003. Photoclinometry made simple...? In: ISPRS Working Group IV/9 Workshop ''Advances in Planetary Mapping 2003", Houston, March 2003. <http://astrogeology.usgs.gov/Projects/ISPRS/Meetings/Houston2003/abstracts/Kirk_isprs_mar03.pdf>

Kivelson, M.G., et al., 2000. Galileo magnetometer measurements: A stronger case for a subsurface ocean at Europa. Science, v. 289, p. 1340-1343

Kleinhans, M.G., Markies, H., de Vet, S.J., in't Veld, A.C., Postema, F.N., 2011. Static and dynamic angles of repose in loose granular materials under reduced gravity. J. Geophys. Res., v. 116, E11004.

Kuroiwa, D., Mizuno, Y., and Takeuchi, M., 1967. Micromeritical properties of snow. In *Physics of snow and ice* (ed. H. Oura, University Institute of Low Temperature Science, Sapporo, Hokkaido), v. 1, part 2, p. 751-772.

Lucchitta, B.K., and Soderblom, L.A., 1982.The geology of Europa. In *Satellites of Jupiter* (ed. D. Morrison, Univ. of Arizona Press, Tucson, AZ), p. 521–555.

Manga, M., and Wang, C. Y. 2007. Pressurized oceans and the eruption of liquid water on Europa and Enceladus, Geophys. Res. Lett., v. 34, L07202.

Michaut, C., and Manga, M., 2014. Domes, pits, and small chaos on Europa produced by water sills. J. Geophys. Res. – Planets, p. 550–573.

Moore, J.M., Asphaug, E., Morrison, D., Spencer, J.R., Chapman, C.R., Bierhaus, B., Sullivan, R.J., Chuang, F.C., Klemaszewski, J.E., Greeley, R., Bender, K.C., Geissler, P.E., Helfenstein, P., and Pilcher, C.B. 1999. Mass movement and landform degradation on the icy Galilean satellites: results of the Galileo nominal mission. Icarus v. 140, p. 294–312.

Moratto,Z.M., Broxton, M. J., Beyer, R. A., Lundy, M., Husmann, K., 2010. Ames Stereo Pipeline, NASA's open source automated stereogrammetry software. LPSC XLI, abstract #2364

Nimmo, F. and Gaidos, E.J. 2002. Strike-slip motion and double ridge formation on Europa. JGR, v. 107, E4. 5021.

Pappalardo, R.T. et. al. 1999. Does Europa have a subsurface ocean? Evaluation of the geological evidence. JGR, v. 104, E10. 24015-24055.

Pappalardo, R. T., 2000. Upwarped domes on Europa: Constraints on mottled terrain formation. LPSC XXXI, Abstract #1719

Patterson, G.W., Prockter, L.M., and Schenk, P. Examining topographic variability within chaos terrain on Europa. AGU Fall Meeting 2008, Abstract #P23A-1351.

Porco, C.C., et al. 2006. Cassini observes the active south pole of Enceladus. Science, v. 311, p. 1393–1401.

Prockter, L.M., and Schenk, P. 2005. Origin and evolution of Castalia Macula, an anomalous young depression on Europa. Icarus, v. 177, issue 2, p. 305-326

Rathbun, J.A., Musser Jr., G.S., Squyres, S.W., 1998. Ice diapirs on Europa: Implications for liquid water. Geophys. Res. Lett. v. 25, p. 4157–4160.

Sack N. J., Baragiola R. A., and Johnson R. E. (1993) Effect of plasma ion bombardment on the reflectance of Io's trailing and leading hemispheres. Icarus, v. 104, p. 152–154.

Spaun, N.A., Pappalardo, R.T., and Head, J.W., 2003. Evidence for shear failure in forming near-equatorial lineae on Europa. J. Geophys. Res. v. 108. 10.1029/2001JE001499.

Spencer, J.R., Tamppari, L.K., Martin, T.Z., Travis, L.D., 1999. Temperatures on Europa from Galileo photopolarimeter–radiometer: nighttime thermal anomalies. Science, v. 284, p. 1514–1516.

Sullivan, R. et. al. 1997. Ridge formation on Europa: Examples from Galileo high resolution images. Geol. Soc. Am. Abstr. Programs, 29, A-312.

Sullivan R., Moore J., and Pappalardo R. (1999) Mass-wasting and slope evolution on Europa. LPSC XXX, Abstract #1747

Sylvester, A. G., 1988. Strike-slip faults. Bull. Geol. Soc. Am., v. 100, p. 1666–1703.

Turcotte, D.L., and G. Schubert, Geodynamics. 456 pp., John Wiley, New York, 2002

Turtle, E.P., and Pierazzo, E., 2001. Thickness of a Europan ice shell from impact crater simulations. Science, v. 294, p. 1326–1328.

Weiss, P., Yung, K. L., Kömle, N., Ko, S. M., Kaufmann, E., Kargl, G., 2011. Thermal drill sampling system onboard high-velocity impactors for exploring the subsurface of Europa. Advances in Space Research, v. 48, issue 4, p. 743-754.

Wilson, L., and Head, J.W., and Pappalardo, R.T., 1997. Eruption of lava flows on Europa: Theory and application to Thrace Macula, J. Geophys. Res., v. 102, p. 9263– 9272.

Wilson, L., and Head, J.W., 1998. Europa cryovolcanism: ascent and eruption of magma and its role in resurfacing. LPSC XXIX, Abstract #1138

Yuen, D. A., L. Fleitout, G. Schubert, and C. Froidevaux, Shear deformation zones along major transform faults and subducting slabs, Geophys. J. R. Astron. Soc., 54, 93– 119, 1978.

Zahnle, K., Schenk, P., Dones, L., Levison, H.F., 2003. Cratering rates in the outer solar system. Icarus v. 163, p. 263–289.

Appendix

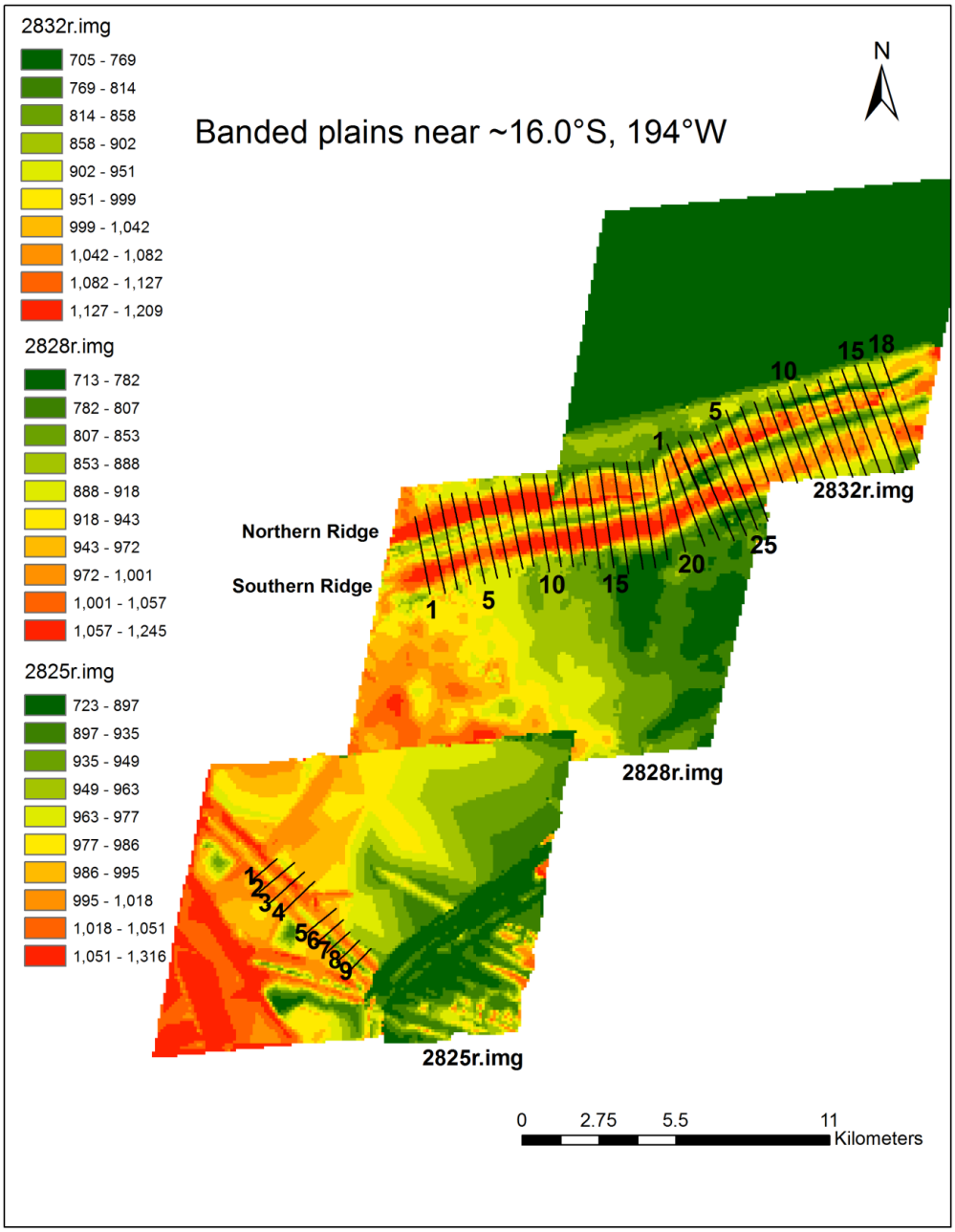

Figure 9. Banded plains region (~16.0°S, 194°W) SOCET-SET DEMs (100m resolution) created with higher resolution images (from south to north): 2825r.img, 2828r.img, and 2832r.img (25m/pixel resolution). These images were paired with base image 3800r.img (48m/pixel resolution). Elevation data for the area north of the ridge featured in 2832r.img were set to null during processing for ease of editing in SOCET-SET, which resulted in the green color for this region (constant arbitrary elevation). The elevations in areas of overlap between DEMs do not match perfectly, as the base elevation values for each surface are determined within SOCET-SET, and no control for elevation (such as MOLA tracks for martian data) exist for Europa. Profiles 21 - 26 on the 2828 DEM overlap with profiles 1-6 on the 2832r.img DEM. The last five profiles for 2828r.img show only the southern ridge, while the first eight profiles in 2832r.img show the northern ridge and only the interior of the southern ridge.

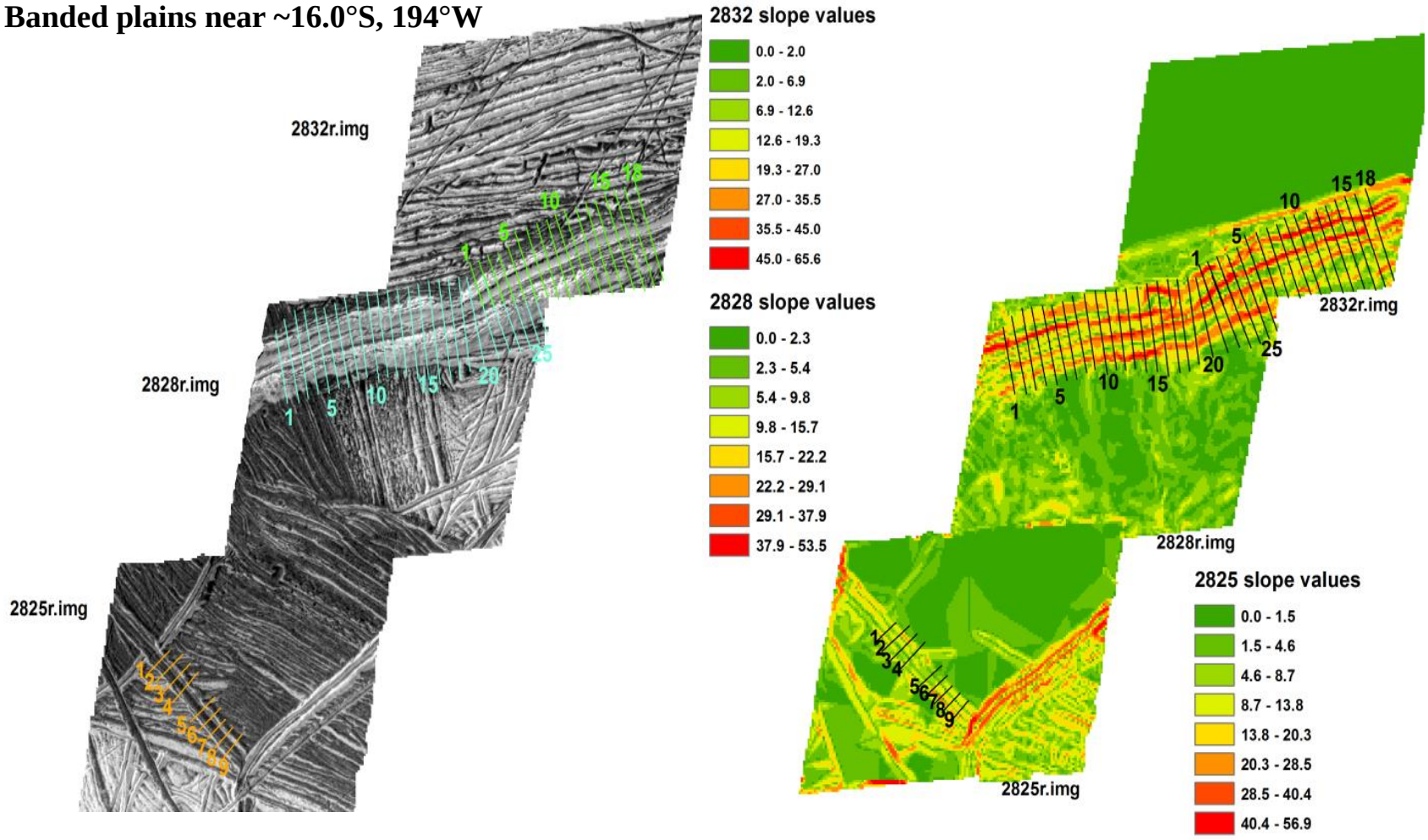

Figure 10. Banded plains region (~16.0°S, 194°W) orthoimages (left) and slope maps (right) accompanying three DEMs shown in Figure 9. As in Figure 9, profiles 21 - 26 on the 2828 DEM overlap with profiles 1-6 on the 2832r.img DEM, the last five profiles for 2828r.img show only the southern ridge, while the first eight profiles in 2832r.img show the northern ridge and only the interior of the southern ridge. The dark bands at the southwest of the figure are Yelland Linea.

Table 5. Banded Plains 2828r.img SOCET-SET DEM slope values for 26 profile lines. Two sets of interior slopes (I1 and I2) and exterior slopes (E1 and E2) are reported. The average, standard error (SE), and range are also reported.

	Profile	1	2	3	4	5	Average	SE	Range
1	E1	26.4	26.2	26.0	26.3	25.7	26.1	0.29	0.74
	I1	54.1	54.1	54.4	54.1	55.1	54.3	0.44	1.04
	I2	29.7	21.2				25.4	6.02	8.52
	E2	26.7	26.1	26.8	26.8	27.1	26.7	0.36	1.00
2	E1	18.5	18.4	18.5	17.9	18.5	18.4	0.25	0.63
	I1	41.9	42.1	42.0	41.8	42.0	42.0	0.12	0.29
	I2	28.6	29.0	28.9	28.2	29.1	28.8	0.37	0.92
	E2	19.9	19.8	19.7	20.0	20.0	19.9	0.11	0.26
3	E1	20.3	20.6	20.5	20.2	20.4	20.4	0.16	0.38
	I2	28.4	30.2	29.6	28.3	28.6	29.0	0.83	1.88
	E2	32.5	33.0	33.1	32.4	32.4	32.7	0.34	0.72
4	E1	20.1	20.5	20.7	20.1	20.8	20.4	0.32	0.70
	I2	25.5	25.6	26.7	24.3	26.2	25.7	0.89	2.38
	E2	23.1	23.3	22.4	23.6	22.6	23.0	0.50	1.22
5	E1	22.5	21.2	22.5	22.5	22.5	22.2	0.57	1.30
	I1	58.8	62.3	59.0	61.2	61.8	60.6	1.60	3.45
	I2	25.6	24.9	26.2	23.4	23.9	24.8	1.17	2.81
6	E1	35.2	34.8	35.0	34.5	35.3	34.9	0.33	0.82
	I1	69.0		64.5		65.7	66.4	2.33	4.49
	I2	26.1	25.4				25.7	0.47	0.66
	E2	18.4	19.2				18.8	0.59	0.84
7	E1	26.6	25.8	26.5	26.8	27.0	26.5	0.45	1.17
	I1	51.9	51.9	52.1	52.3	51.8	52.0	0.18	0.47
	E2	29.0	29.8	27.4	31.4	29.8	29.5	1.45	3.99
8	E1	28.0	28.1	28.1	28.1	28.0	28.1	0.06	0.16
	E2	26.7	26.4	26.6	26.4	26.1	26.4	0.25	0.67
9	E1	27.3	27.6	27.0	28.3	27.8	27.6	0.48	1.25
	E2	24.7	24.2	24.9	24.1	24.4	24.5	0.33	0.80
10	E1	28.6	28.1	27.7	28.0	27.3	28.0	0.48	1.30
	I1	39.5				40.7	40.1	0.84	1.19
	I2	30.0	29.5	30.2	32.2	31.3	30.6	1.10	2.73
	E2	33.4	33.5	36.5	32.0	33.1	33.7	1.70	4.59
11	E1	22.6	22.4	22.5	22.3	22.6	22.5	0.12	0.29
	I1	42.0	42.6	42.3	40.5	42.5	42.0	0.85	2.06
	I2	43.0	40.2	41.2	43.0	41.1	41.7	1.22	2.74

Table 5 continued

	Profile	1	2	3	4	5	Average	SE	Range
11	E2	40.4	40.4	40.4	38.4	39.5	39.8	0.88	2.02
12	E1	23.7	24.4	24.0	23.3	24.0	23.9	0.41	1.10
	I1	46.5	49.6	45.0	50.0	44.1	47.0	2.67	5.90
	I2	40.7	37.1	40.4	37.5	39.7	39.1	1.69	3.65
	E2	44.5			40.8	42.2	42.5	1.88	3.73
13	E1		20.3	21.0	21.0	20.9	20.8	0.35	0.74
	I1	36.6	35.6	35.4	35.8	36.2	36.0	0.48	1.21
	I2	43.6	45.8	43.1	43.9	44.6	44.2	1.06	2.72
	E2	51.6	57.4	52.7	54.5	56.4	54.5	2.42	5.74
14	E1	19.7	19.8	20.0	19.7	19.7	19.8	0.15	0.37
	I1	52.0	52.9	51.6	55.9	51.8	52.8	1.78	4.28
	I2	39.5	42.5	41.3	37.7	38.1	39.8	2.05	4.81
	E2	56.2	58.3	57.5			57.3	1.01	2.01
15	I2	33.3	38.5	32.3	34.9	31.6	34.1	2.76	6.97
	E2	49.9	51.2	49.8	46.9	51.3	49.8	1.78	4.43
16	E1	59.4	58.7	58.8	58.3	58.8	58.8	0.42	1.16
	I2	38.2	38.2	38.0	38.2	37.7	38.1	0.21	0.52
	E2	27.4	27.3	27.6	27.4	27.6	27.5	0.13	0.29
17	E1	38.1	38.2	38.4	39.2	39.5	38.7	0.63	1.39
	I1	34.9	34.4	34.3	34.0	35.8	34.7	0.68	1.74
	I2	35.1	35.4	36.2	36.1	35.9	35.8	0.48	1.09
	E2	30.1	30.0	28.9	28.1	28.3	29.1	0.91	1.92
18	E1	29.3	29.3	29.4	29.3	29.5	29.3	0.10	0.23
	I1	27.2	27.6	27.6	27.6	28.1	27.6	0.30	0.85
	I2	30.9	30.7	30.2	30.0	29.7	30.3	0.48	1.16
	E2	31.8	31.7	33.2	33.6	33.6	32.8	0.93	1.87
19	E1	21.3	20.6	21.0	20.6	20.3	20.8	0.36	0.91
	I1	28.2	28.6	26.4	26.2	27.0	27.3	1.09	2.42
	I2	28.7	29.0	27.7	28.5	27.0	28.2	0.82	2.00
	E2	26.3	25.7	27.3	26.3	27.4	26.6	0.72	1.66
20	E1	26.0	25.8	26.4	26.4	25.4	26.0	0.42	1.03
	I1	44.5	44.3	44.0	45.7	41.9	44.1	1.38	3.80
	I2	35.9	35.8	36.9	34.4	30.7	34.7	2.43	6.23
	E2	29.5	29.7	28.9	29.8	29.5	29.5	0.33	0.87
21	E1	30.2	30.6	29.5	29.3	27.8	29.5	1.05	2.74
	I1	51.7	50.8	50.6	51.2	52.0	51.3	0.58	1.36

Table 5 continued

	Profile	1	2	3	4	5	Average	SE	Range
21	I2	32.5	33.7	32.5	31.8	32.2	32.6	0.72	1.91
	E2	26.8	26.7	27.2	27.0	26.7	26.9	0.20	0.47
22	I1	42.3	41.1	43.8	43.1	43.1	42.7	1.04	2.73
	I2	34.3	28.4	30.6	32.0	32.2	31.5	2.16	5.88
	E2	31.1	31.2	30.6	31.1	31.1	31.0	0.22	0.54
23	I1	51.3	48.3	52.8	52.2	52.3	51.4	1.78	4.43
	I2	40.4	41.2	39.0	38.9	39.5	39.8	0.98	2.27
	E2	40.1	39.8	39.2	39.3	40.3	39.7	0.47	1.11
24	I2	32.1	29.0	30.4	30.2	31.5	30.6	1.22	3.13
	E2	47.3	49.7	42.8	49.4	46.8	47.2	2.75	6.86
25	I2	37.1	35.3	37.1	35.8	35.9	36.2	0.82	1.83
	E2	45.7	44.3	43.2	44.1	44.0	44.3	0.92	2.52
26	I2	32.0	32.4	31.9	32.7	31.5	32.1	0.50	1.27
	E2	29.3	29.2	28.0	28.1	29.5	28.8	0.72	1.58

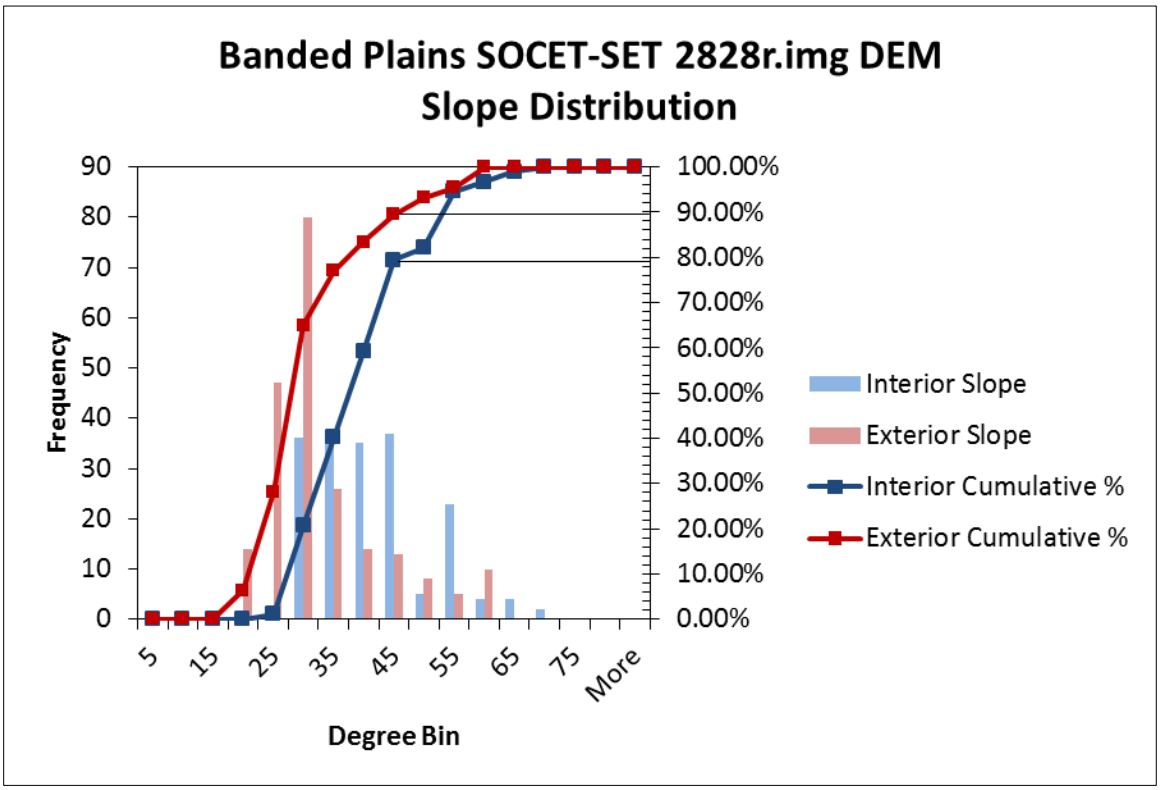

Figure 11. Banded Plains SOCET-SET 2828r.img DEM slope distribution. A total of 184 interior and 217 exterior slopes are plotted. The exterior slopes are more skewed to the right, favoring lower values, while interior slopes are more evenly distributed. The cumulative frequency for both slope samples is also plotted, with ~80% of the interior slopes and ~90% of the exterior slopes being at or below the AOR (the positions as shown in the black lines approaching the second y axis).

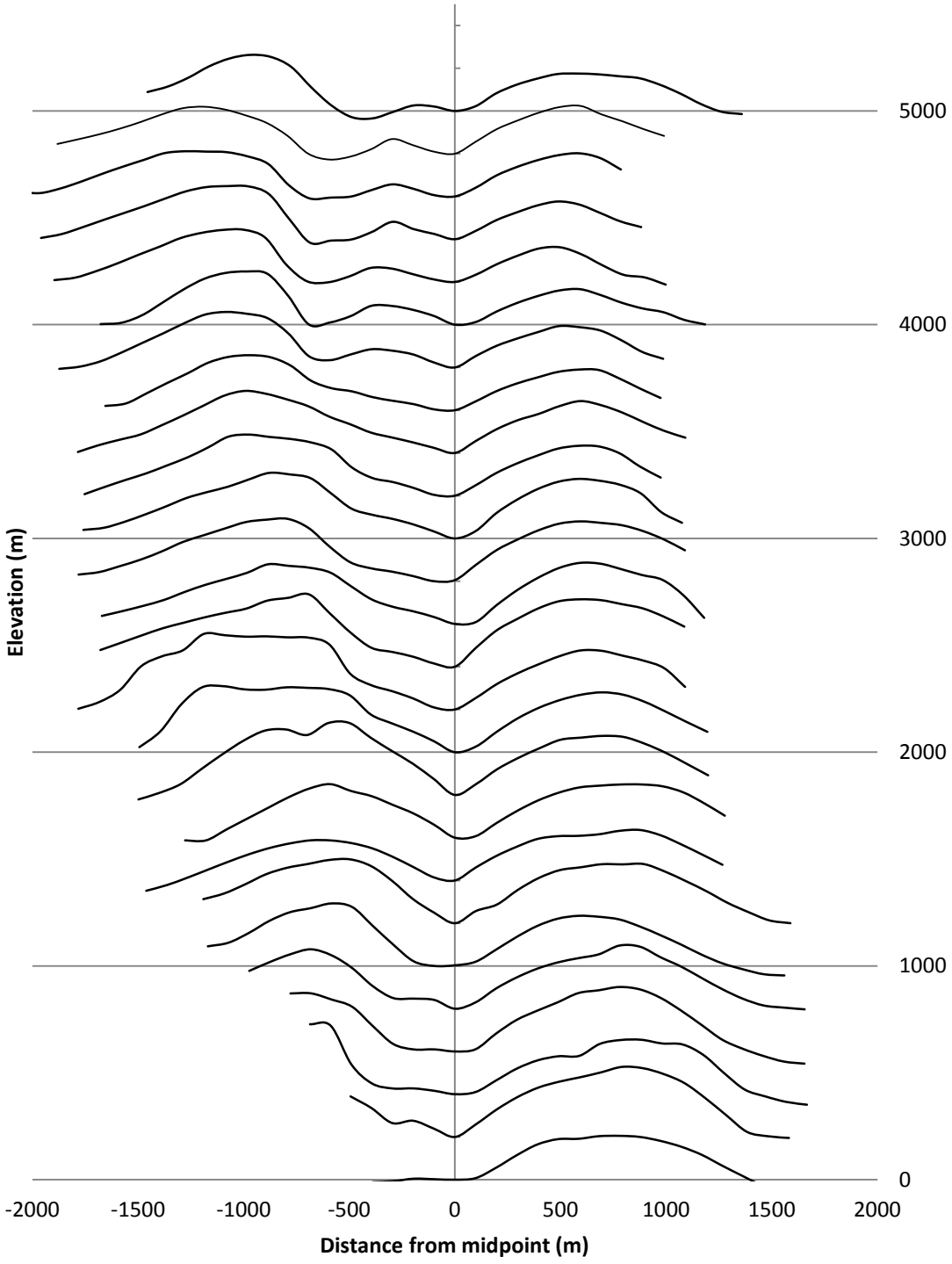

Figure 12. Banded Plains 2828r.img DEM double ridge profile lines 1-26 (offset 200m for clarity). Profile lines were drawn from north to south, giving the northern ridge as the ridge to the left in this figure, and the southern ridge as the ridge to the right.

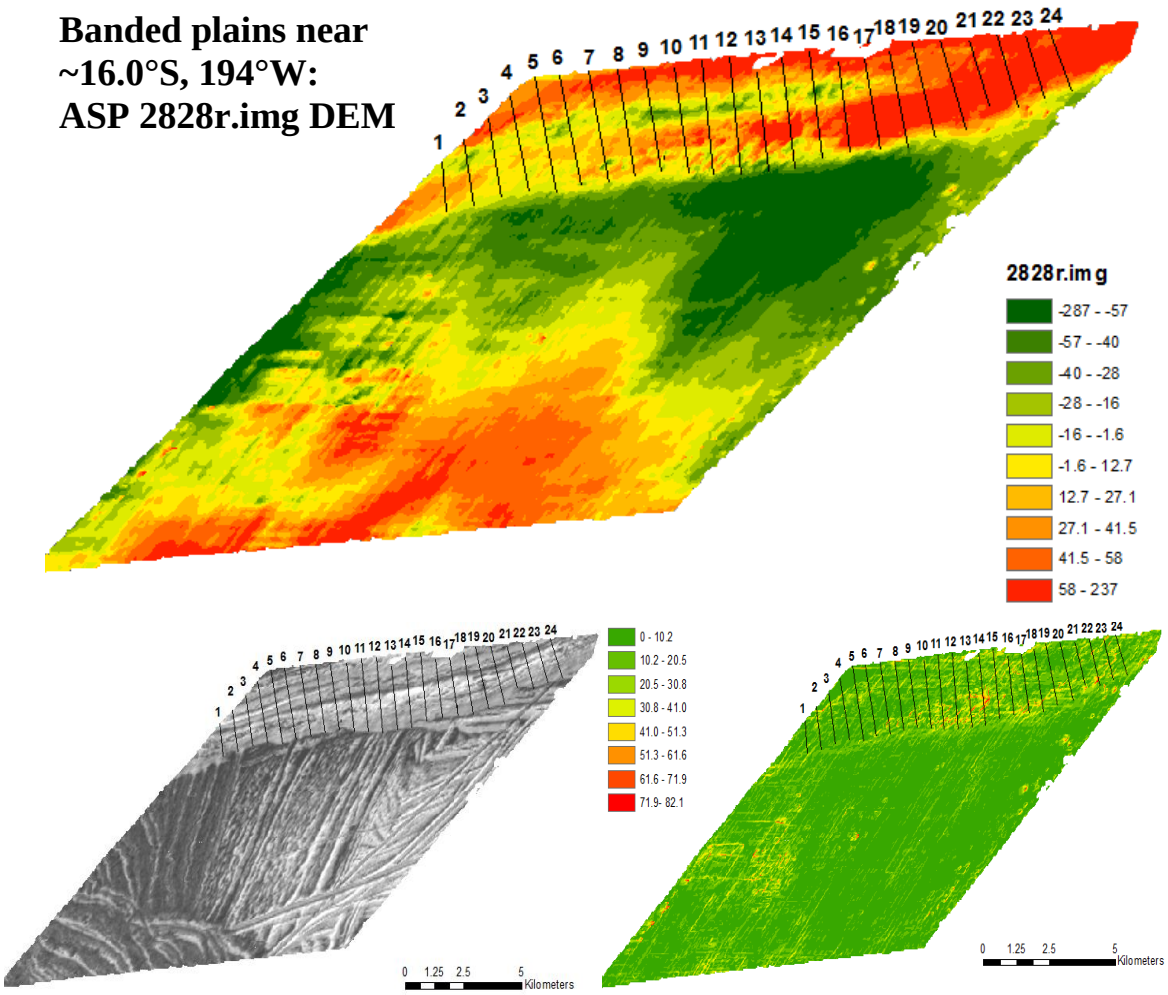

Figure 13. Banded plains region (~16.0°S, 194°W) ASP DEM (upper image). DEM has 95m resolution and was created with higher resolution image 2828r.img (25m/pixel) paired with base image 3800r.img (48m/pixel). Orthoimage (lower left) and slope map (lower right) included. This is the same ridge pictured in the SOCET-SET DEM using the same stereo-pair images (Figure 9).

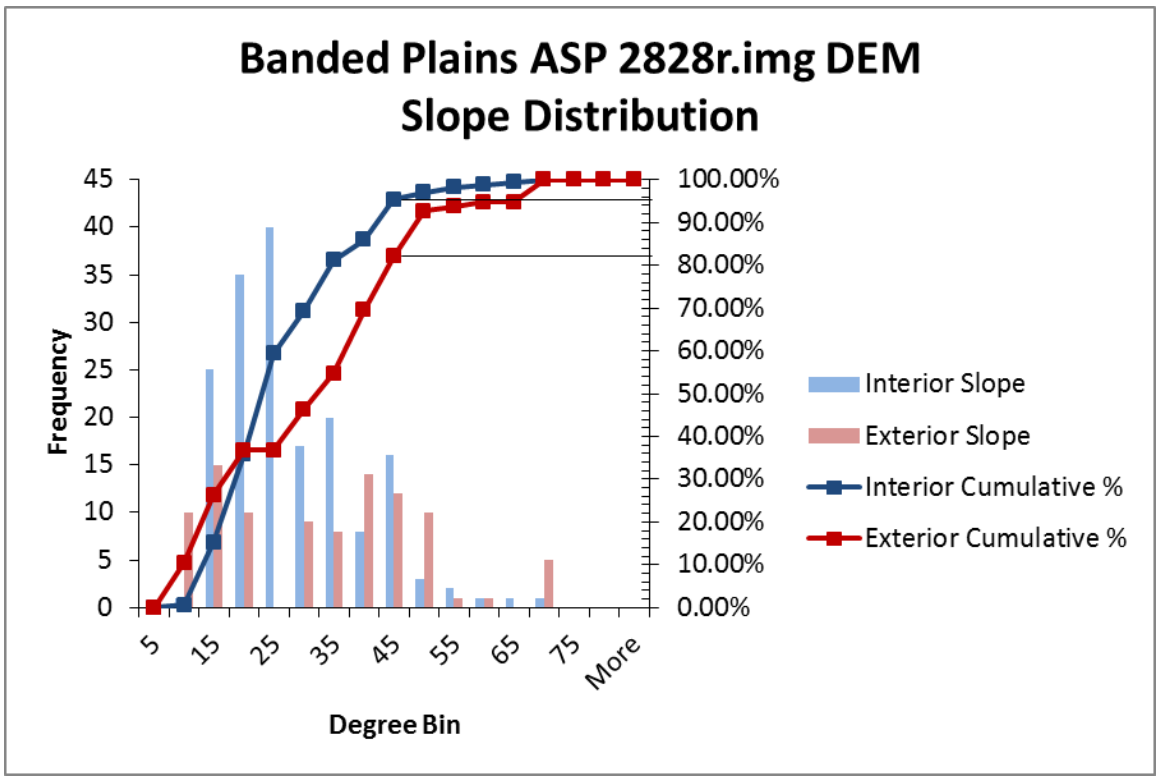

Figure 14. Banded Plains ASP 2828r.img DEM slope distribution. A total of 170 interior and 90 exterior slopes are plotted. The exterior slopes appear more evenly distributed, while interior slopes are right skewed, favoring shallower slopes. The cumulative frequency for both slope samples is also plotted, with ~96% of the interior slopes and ~82% of the exterior slopes being at or below the AOR (the positions as shown in the black lines approaching the second y axis).

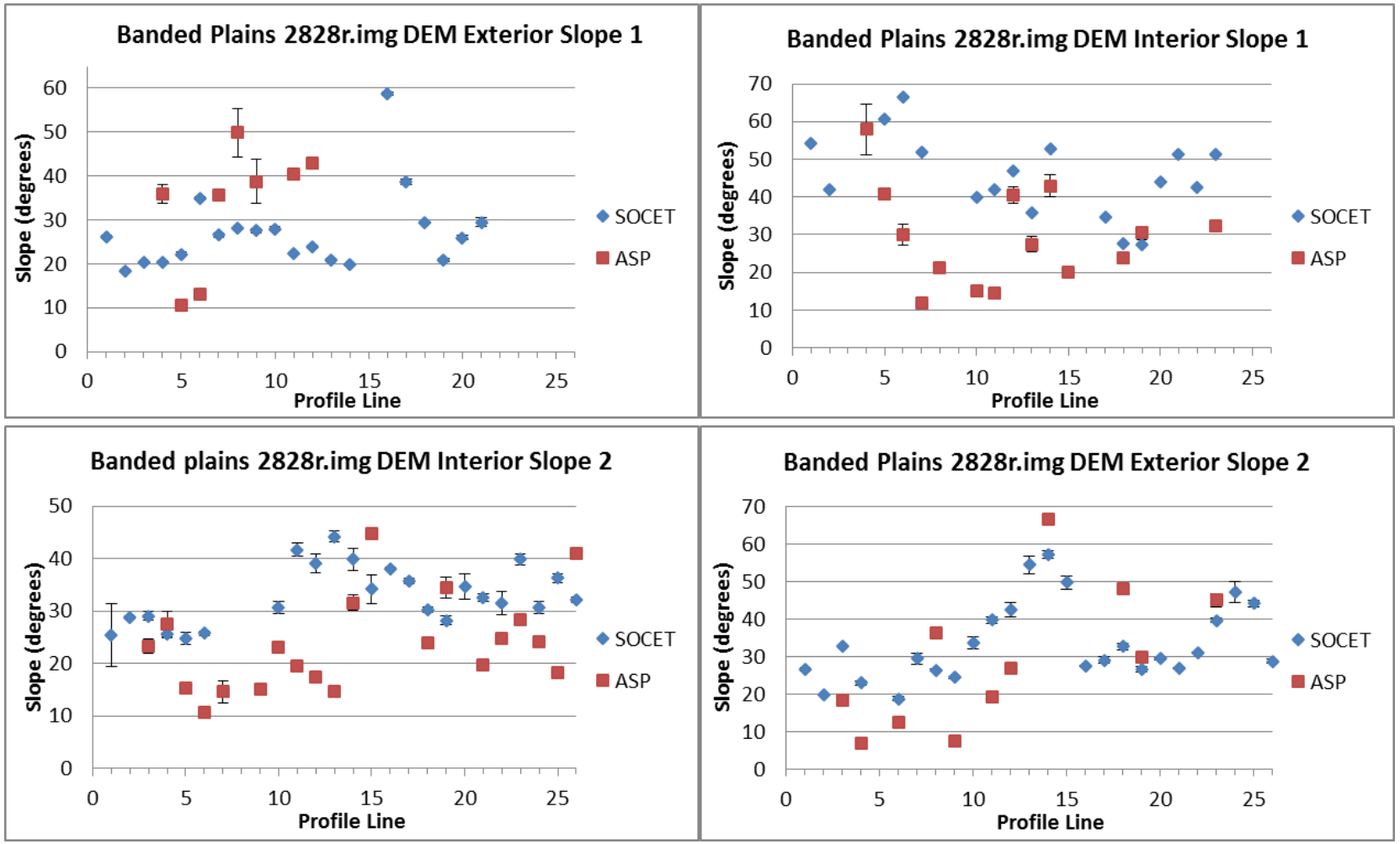

Figure 15. Banded Plains SOCET-SET and ASP 2828r.img DEM slope distributions along trend, comparing overlapping exterior (E1 and E2) and interior (I1 and I2) slopes derived from the two DEM generation techniques. The SOCET-SET profile line numbers are plotted along the x axes, with profile lines 3-26 of the SOCET-SET DEM overlapping with profile lines 1-24 of the ASP DEM. Thus, the two points per profile line can be directly compared on these plots. Each data point represents the average of five individual slopes along the given ridge section. Exterior slope 1 and interior slope 1 (top two plots) are along the northern ridge in Figure 9, shown as the first two slopes in the topographic profiles in Figure 12. The Interior slope 2 and exterior slope 2 are along the southern ridge, shown as the last two slopes in the topographic profile in Figure 12.

Table 6. Banded Plains 2832r.img SOCET-SET DEM slope values for 18 profile lines. Two sets of interior slopes (I1 and I2) and exterior slopes (E1 and E2) are reported. The average, standard error (SE), and range are also reported.

	Profile	1	2	3	4	5	Average	SE	Range
1	E1	64.0	63.2	65.7	65.1	63.5	64.3	1.06	2.46
2	E1	59.8		61.9			60.8	1.51	2.14
4	I1	61.6	62.5	62.8	61.9	61.8	62.1	0.50	1.22
	I2	42.4	42.7	41.8	42.4	42.2	42.3	0.35	0.95
6	E1	64.8	65.7	65.0	65.0	64.8	65.1	0.37	0.90
7	I1	69.3	69.0	69.3	69.2	69.2	69.2	0.11	0.27
8	E1	42.5	43.1	42.3	41.9	42.8	42.5	0.48	1.22
9	I1	60.4	59.1	59.5	58.2	59.5	59.3	0.80	2.19
10	E1	77.4	78.4	77.2	76.5	75.9	77.1	0.94	2.48
	E2	31.1	31.0	31.2	31.2	31.5	31.2	0.20	0.56
11	E1	66.0	65.6	65.3	64.6	65.0	65.3	0.52	1.36
	I1	41.9	42.1	42.1	42.4	42.3	42.1	0.19	0.50
	I2	38.5	39.0	39.0	39.5	39.3	39.1	0.37	0.95
	E2		37.4	36.9	37.8	37.7	37.4	0.42	0.90
13	E1	60.6	59.3	58.9	59.7	61.9	60.1	1.19	2.95
	I1		65.2	64.9	63.4	56.8	62.6	3.90	8.30
	I2	36.4	32.7	33.3	31.6	26.7	32.1	3.53	9.71
	E2		24.2		24.9		24.6	0.49	0.70
14	E1	74.0	70.8	73.4	73.8	74.1	73.2	1.38	3.30
	I1	67.8	68.3	67.6	67.8	67.9	67.9	0.25	0.66
	I2	41.6	41.6	41.6	41.5	41.5	41.6	0.06	0.16
15	E1	65.3	65.3	65.3	65.4	65.3	65.3	0.05	0.15
	I1	69.1	69.3	70.5	68.9	71.2	69.8	1.02	2.34
	I2	38.2	38.2	38.0	38.2	38.0	38.1	0.08	0.15
16	E1	69.5	69.7	69.6	69.6	70.3	69.7	0.32	0.83
	I1	65.3	66.0	64.9	66.0	68.7	66.2	1.49	3.80
	I2	31.9	32.2	31.8	32.1	32.6	32.1	0.33	0.84
17	E1	69.6	68.2	69.3	69.6	71.0	69.5	1.01	2.84
	I2	37.5	36.7	36.3	37.1	38.2	37.2	0.74	1.91
	E2		47.8	48.0	48.2	45.5	47.4	1.26	2.69
18	I1	30.6	30.2	30.8	30.9	31.0	30.7	0.31	0.78
	I2	31.5	32.0	30.7	30.7	30.4	31.1	0.66	1.60
	E2	29.0	28.7	28.8	29.4	29.5	29.1	0.36	0.85

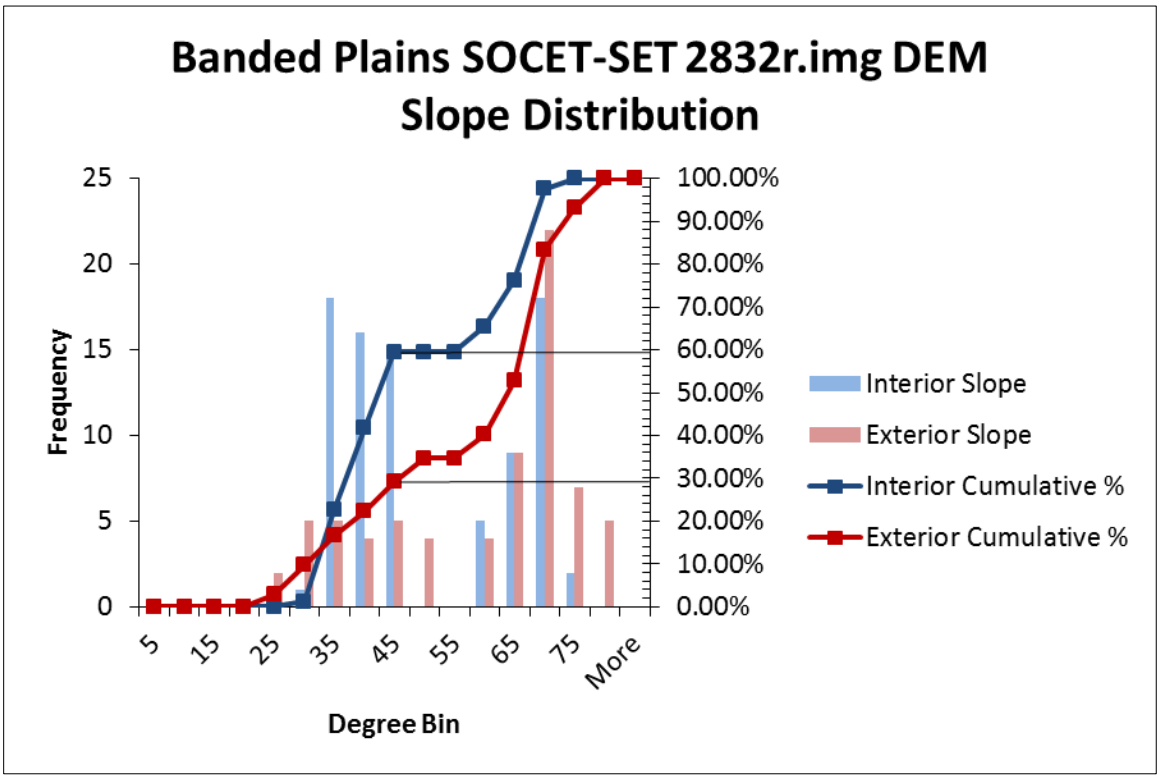

Figure 16. Banded Plains SOCET-SET 2832r.img DEM slope distribution. A total of 84 interior and 72 exterior slopes are plotted. Interior slopes show a distinct bimodal distribution, while exterior slopes show a similar distribution but skewed to the left, favoring higher slope values. The cumulative frequency for both slope samples is also plotted, with ~60% of the interior slopes and ~30% of the exterior slopes being at or below the AOR (the positions as shown in the black lines approaching the second y axis).

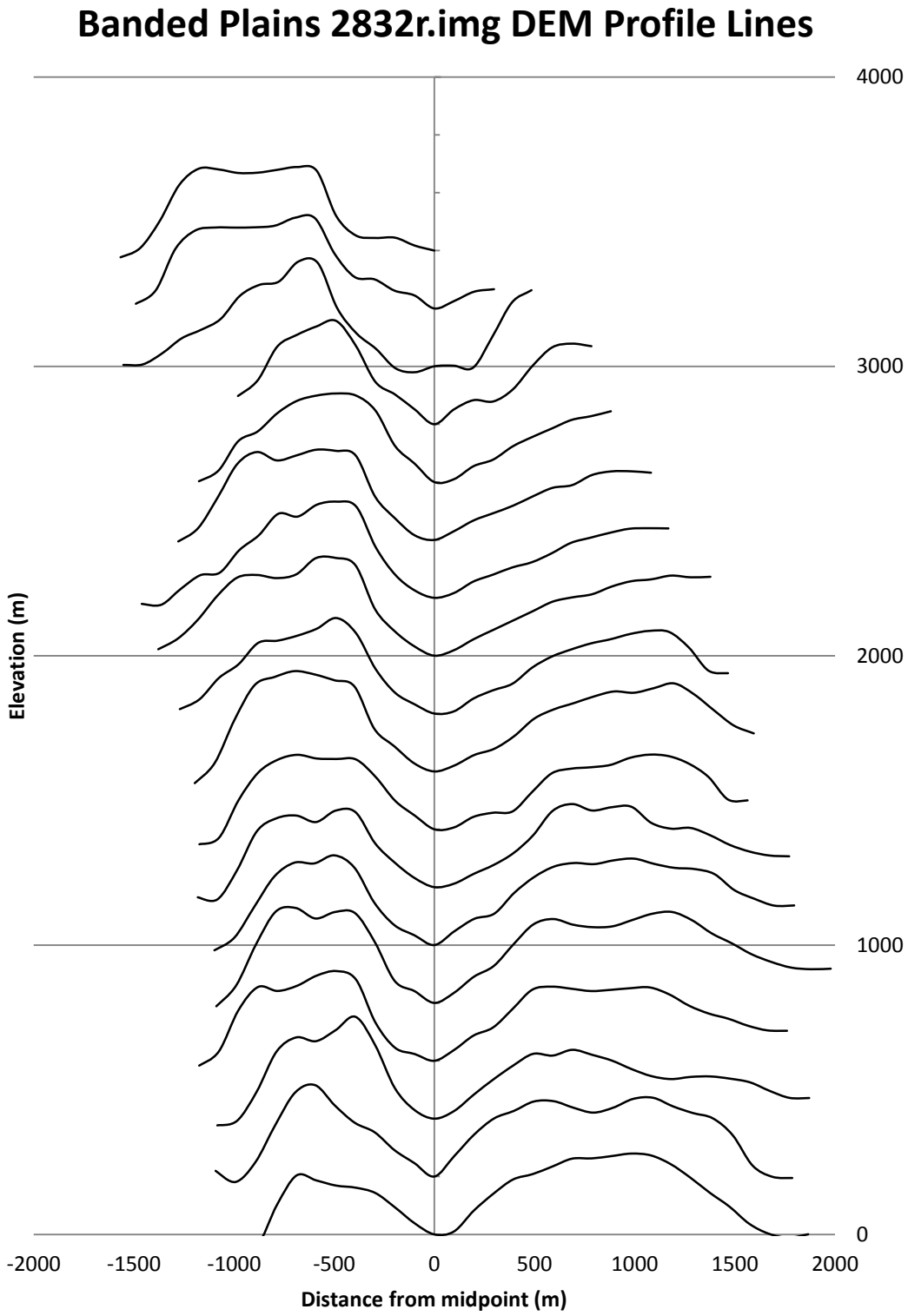

Figure 17. Banded Plains 2832r.img DEM double ridge profile lines 1-18 (offset 200m for clarity). Profile lines were drawn from north to south, giving the northern ridge as the ridge to the left in this figure, and the southern ridge as the ridge to the right.

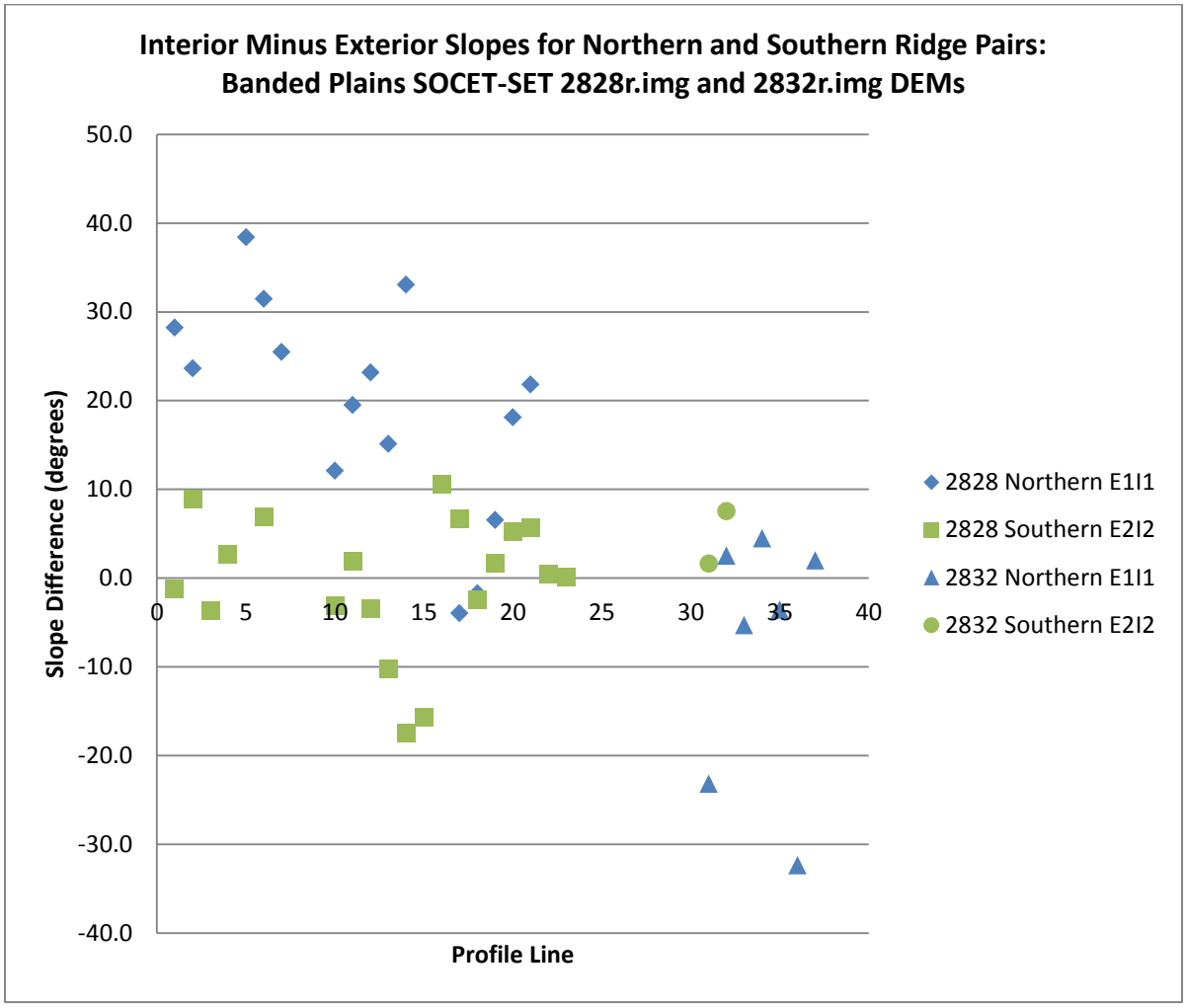

Figure 18. Banded Plains SOCET-SET DEM 2828r.img and 2832r.img difference plot along strike for interior and exterior slope pairs for the northern (E1I1) and southern (E2I2) halves of the double ridge. Each data point represents the average of five individual slopes along the given ridge section. In each case, the data point is derived by taking the average interior slope of the pair and subtracting the average exterior slope along the same ridge. The values for the southern ridge for both 2828r.img and 2832r.img have a somewhat symmetric distribution along strike, while the values for the northern half appear to decrease along strike, suggesting that the exterior slope is steadily increasing to be comparable with the interior value.

Table 7. Banded Plains 2825r.img SOCET-SET DEM slope values for nine profile lines. Two sets of interior slopes (I1 and I2) and exterior slopes (E1 and E2) are reported. The average, standard error (SE), and range are also reported.

	Profile	1	2	3	4	5	Average	SE	Range
1	E1	11.5	11.0	10.7	10.5	9.9	10.7	0.60	1.62
	I2	11.1	11.1	11.4	10.3	10.6	10.9	0.42	1.01
	E2	9.5	9.9	10.3	9.7	9.7	9.8	0.31	0.80
2	I2	12.1	12.2	12.2	12.1	12.1	12.1	0.05	0.11
	E2	20.5	20.7	20.6	20.5	20.5	20.6	0.07	0.18
3	E1	10.9	10.9	10.9	10.9	10.9	10.9	0.02	0.04
	I2	12.7	12.6	12.6	12.7	12.6	12.7	0.04	0.11
	E2	20.4	20.2	20.4	20.4	20.3	20.3	0.08	0.17
4	E1	10.0	9.4	9.4	10.0	10.0	9.8	0.34	0.70
	I1	9.5			9.6	9.6	9.6	0.04	0.09
	I2	9.1			9.2	9.1	9.1	0.07	0.14
	E2	5.8	6.2	4.6	5.7	5.8	5.6	0.58	1.54
5	I2	6.6	6.5	6.6	6.6	6.6	6.5	0.04	0.10
	E2	4.4	4.0	4.4	4.4	4.5	4.3	0.20	0.50
6	I2	12.7	12.5	12.4	12.4	12.4	12.5	0.11	0.25
	E2	6.6	6.6	6.6	6.5	6.6	6.6	0.02	0.06
7	I2	12.5	11.9	12.2	11.8	12.1	12.1	0.26	0.65
	E2	12.2	12.1	12.1	12.1	12.1	12.1	0.07	0.18
8	E1	12.9	12.9	12.9	12.8	12.8	12.9	0.05	0.13
	E2	13.7	13.8	13.7	13.6	13.7	13.7	0.09	0.25
9	I2	18.0	18.3	18.1	18.2	18.0	18.1	0.13	0.31
	E2	13.5	13.7	13.5	13.5	13.4	13.5	0.10	0.27

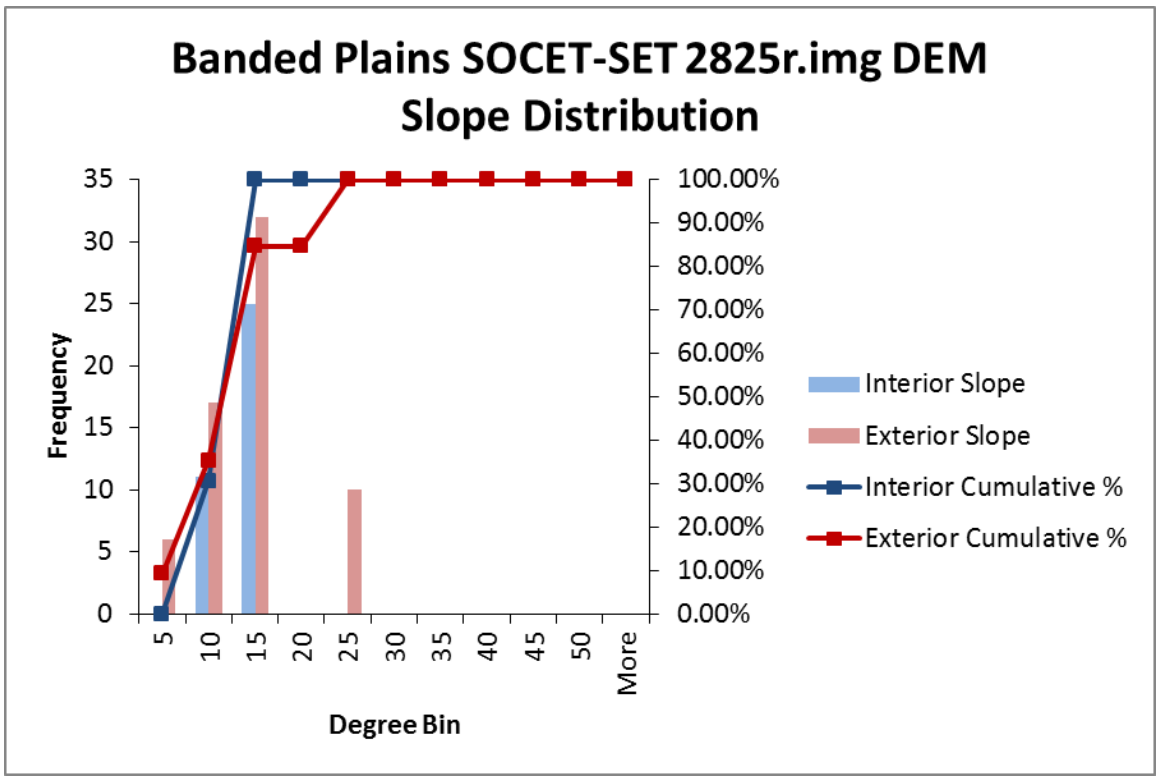

Figure 19. Banded Plains SOCET-SET 2825r.img DEM slope distribution. A total of 36 interior and 65 exterior slopes are plotted. Both show a similar distribution concentrated around lower values, while there is a small population of exterior slopes in excess of 20°. The cumulative frequency for both slope samples is also plotted, with all of the interior slopes and exterior slopes being at or below the AOR.

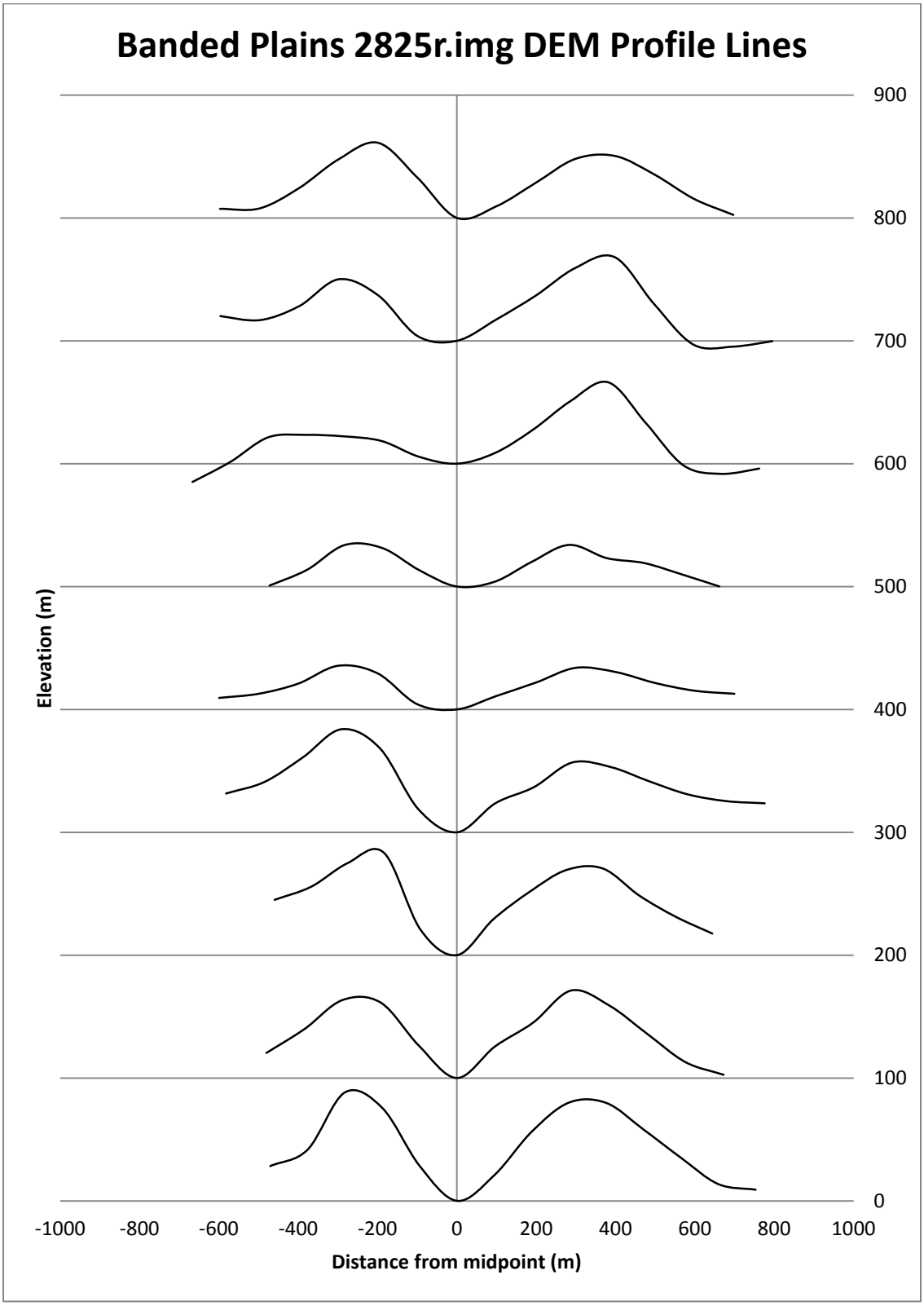

Figure 20. Banded Plains 2825r.img DEM double ridge profile lines 1-9 (offset 100m for clarity). Profile lines were drawn from southwest to northeast.

Cilix West near 2.0°N, 184.0°W: SOCET-SET 7442r.img DEM

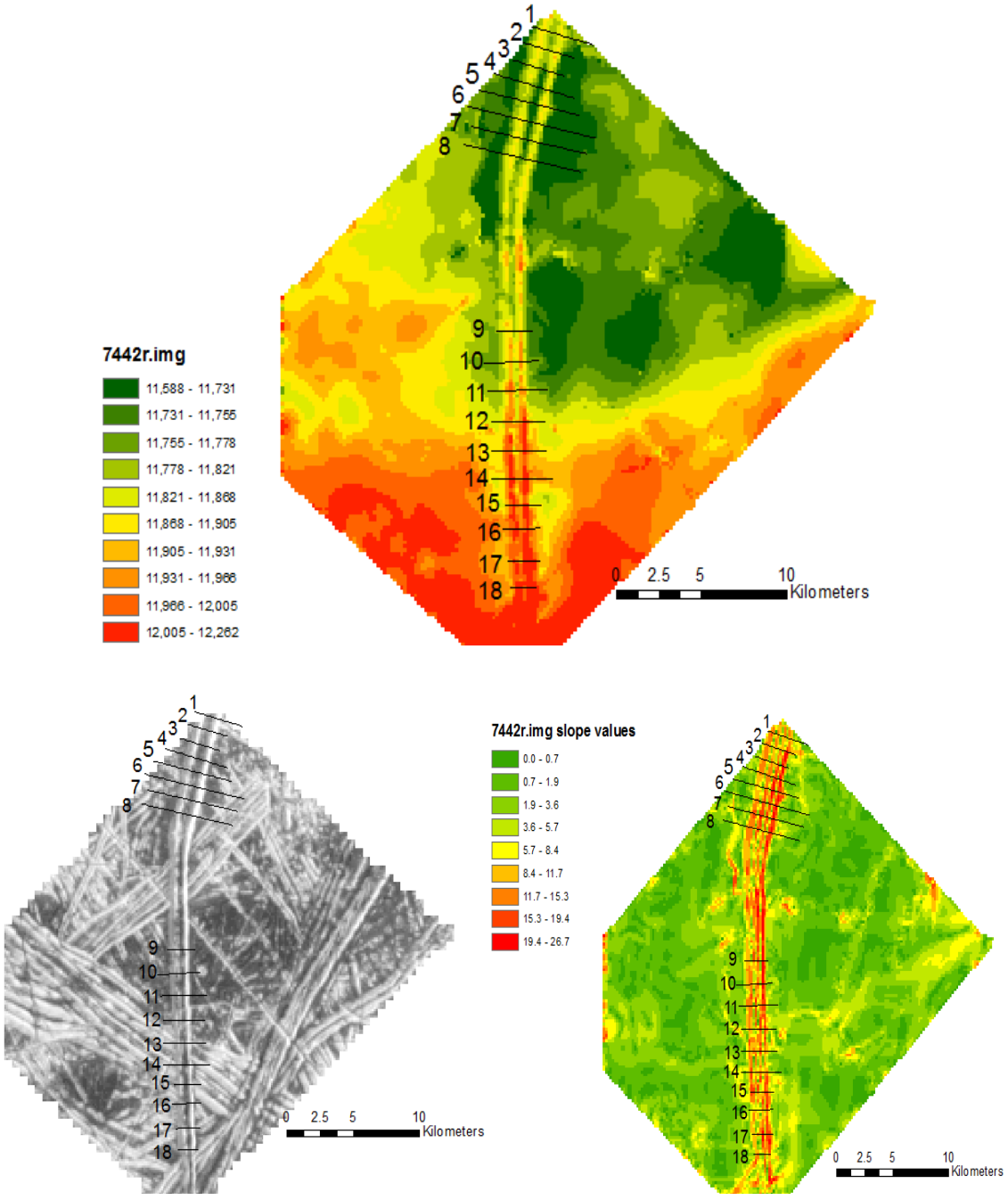

Figure 21. Cilix West region (2.0°N, 184.0°W) SOCET-SET DEM (200m resolution) created with higher resolution image 7442r.img (65m/pixel resolution). The Cilix crater is off the image to the northeast. Image 7442r.img was paired with base image 5013r.img (109 m/pixel) to create this DEM. The accompanying orthoimage (lower left) and slope map (lower right) are shown as well.

Table 8. Cilix West 7442r.img SOCET-SET DEM slopes for 18 profiles, showing two sets of interior (I1 and I2) and exterior slope data (E1 and E2). The average, standard error (SE), and range are also reported.

	Profile	1	2	3	4	5	Average	SE	Range
1	E1	16.1	16.0	15.7	15.5	15.4	15.7	0.30	0.7
	I1	13.8	13.8	13.8	13.0	13.3	13.6	0.39	0.9
	I2	11.5	11.5	11.2	11.9	11.9	11.6	0.33	0.8
	E2	10.5	10.5	10.8	10.3	10.3	10.5	0.22	0.6
2	E1	12.9	12.9	13.2	13.0	13.0	13.0	0.11	0.3
	I1	13.2	12.0	11.2	11.6	11.8	12.0	0.76	2.0
	E2	18.2	19.9	19.1	19.0	18.9	19.1	0.61	1.7
3	E1	12.9	12.7	12.8	12.9	12.8	12.8	0.10	0.3
	I1	13.3	13.6	13.6	13.6	13.8	13.6	0.18	0.5
4	E1	12.2	12.4	12.5	12.2	12.2	12.3	0.12	0.3
	I1	13.7	13.8	13.8	13.7	13.7	13.7	0.02	0.0
5	E1	9.0	8.8	8.9	8.8	8.8	8.9	0.09	0.2
	I1	14.5	12.8	12.7	12.8	12.8	13.1	0.77	1.8
	I2	23.4	23.5	23.4	23.5	23.4	23.4	0.03	0.1
	E2	14.4	14.1	14.2	14.2	14.2	14.2	0.12	0.3
6	E1	12.8	12.7	12.4	12.8	12.8	12.7	0.16	0.4
	I1	16.6	17.0		16.6	16.6	16.7	0.23	0.5
	E2	20.7	20.1	16.5	20.8	20.5	19.7	1.83	4.3
7	E1	18.2	18.1	18.1	18.2	18.1	18.1	0.04	0.1
	I1	20.6	20.6	20.0	20.3	20.6	20.4	0.29	0.6
	E2	19.7	19.8	19.8	19.7	20.0	19.8	0.12	0.3
8	E1	13.5	13.6	13.6	13.6	13.6	13.6	0.01	0.0
	I1	16.9	16.1	16.1	15.7	16.1	16.2	0.45	1.2
	E2	18.9	17.6	17.5	17.3	17.5	17.8	0.63	1.6
9	E1	10.7	10.7	10.7	10.6	10.7	10.6	0.04	0.1
	E2	18.5	18.4	17.8	19.7	18.6	18.6	0.69	1.9
10	E1	12.2	12.2	12.3	12.2	12.2	12.2	0.04	0.1
11	E1	13.8	13.8	13.8	13.7	13.8	13.8	0.05	0.1
12	E1	12.7	12.3	12.2	12.8	12.7	12.6	0.28	0.6
	E2	13.0	12.8	12.5	12.6	12.8	12.7	0.21	0.5
13	E1	12.9	13.0	13.1	13.3	13.1	13.1	0.18	0.5
14	E1	13.7	12.7	11.3	13.9	12.2	12.8	1.09	2.6
15	E1	18.1	17.9	18.3	18.1	14.6	17.4	1.58	3.7
16	E1	6.7	7.7	6.7	7.5	7.4	7.2	0.47	1.0
17	E1	10.2	11.0	9.8	10.6	10.2	10.4	0.45	1.2
	E2	18.5	18.5	17.9	18.3	15.1	17.6	1.44	3.4
18	E1	12.4	11.6	12.3	11.8	11.6	12.0	0.39	0.8
	E2	18.4	12.3	12.3	13.0	11.8	13.6	2.75	6.6

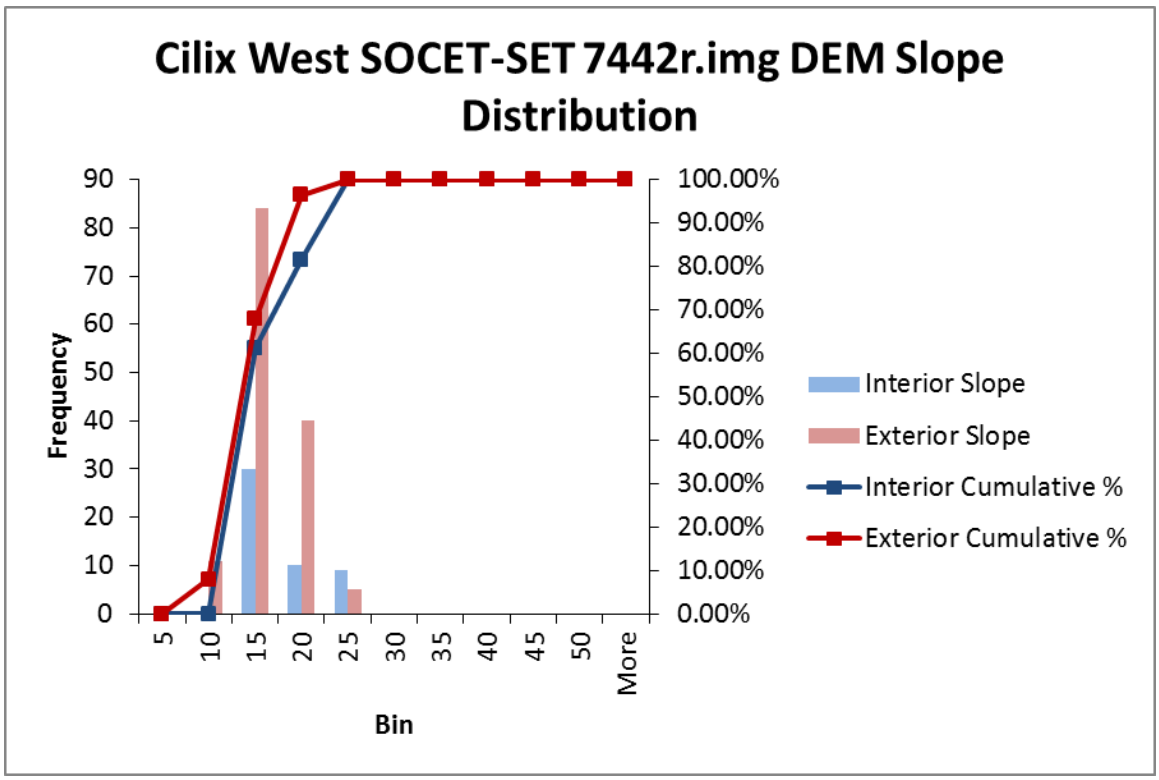

Figure 22. Cilix West SOCET-SET 7442r.img DEM slope distribution. A total of 49 interior and 140 exterior slopes are plotted. The exterior slopes appear fairly normally distributed, while interior slopes are right skewed, favoring lower values slightly. The cumulative frequency for both slope samples is also plotted, with all of the interior slopes and exterior slopes being at or below the AOR.

Cilix West near 2.0°N, 184°W: ASP 7442r.img DEM

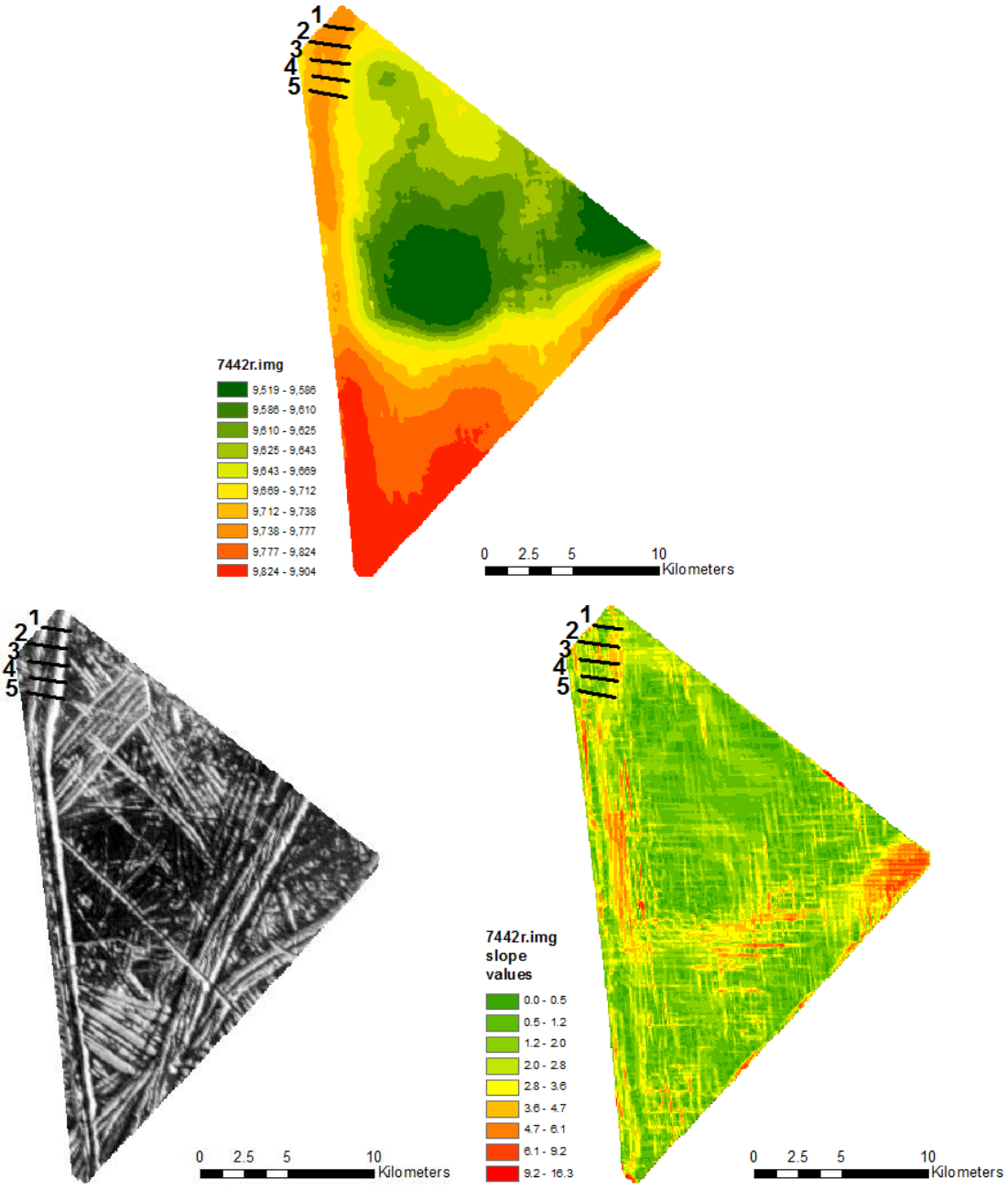

Figure 23. Cilix West region (2.0°N, 184.0°W) ASP DEM (200m resolution) created with higher resolution image 7442r.img (65m/pixel resolution). The Cilix crater is off the image to the northeast. Image 7442r.img was paired with base image 5013r.img (109 m/pixel) to create this DEM. Orthoimage (lower left) and slope map (lower right) are included. This is the same ridge pictured in the SOCET-SET DEM using the same stereo-pair images (Figure 18). Profiles 1-5 in this DEM overlap with profiles 3-7 for the SOCET-SET DEM.

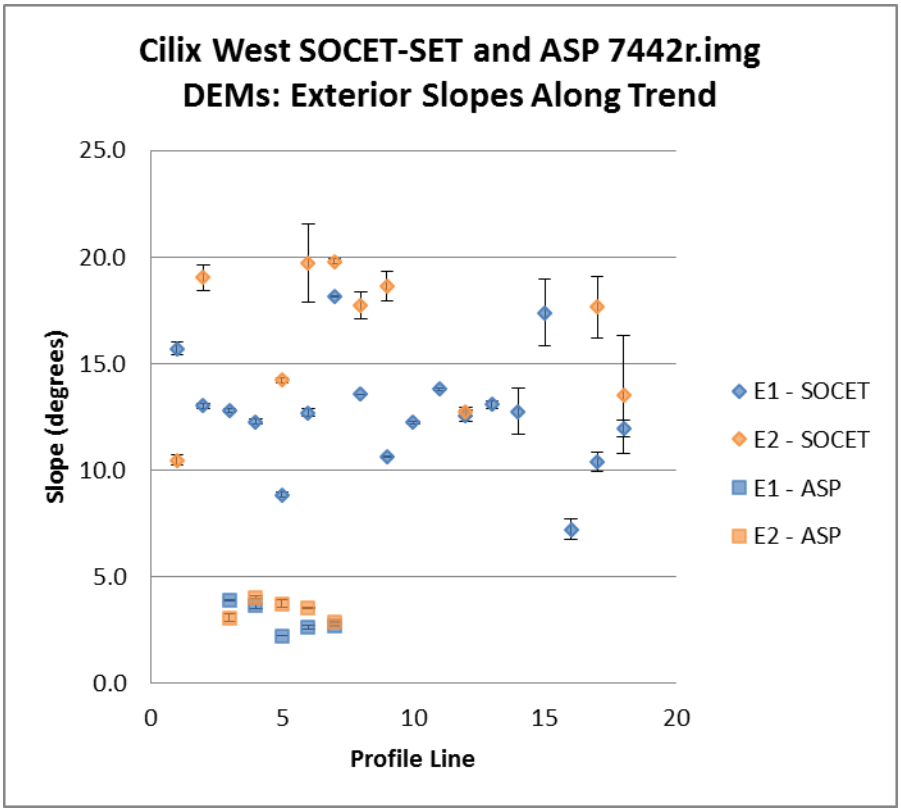

Figure 24. Cilix West SOCET-SET and ASP 7442r.img DEM slope distributions along trend, comparing overlapping exterior (E1 and E2) slopes derived from the two DEM generation techniques. The SOCET-SET profile lines are plotted here, with profile lines 3-7 of the SOCET-SET DEM (along the x-axis of this plot) overlap with profile lines 1-5 of the ASP DEM. Thus, the two points per profile line can be directly compared on these plots. Each data point represents the average of five individual slopes along the given ridge section. Only exterior slopes are plotted here, as exterior slopes only were derived from the ASP DEM due to the coarseness of the resulting DEM. The exterior slopes for the western half (blue diamonds) are typically 10° steeper for the SOCET-SET DEM, while the exterior slopes for the eastern half (orange triangles) are closer to 15° steeper for the SOCET-SET DEM.

Cilix West near 1.5°N, 183.0°W: SOCET-SET 7446r.img DEM

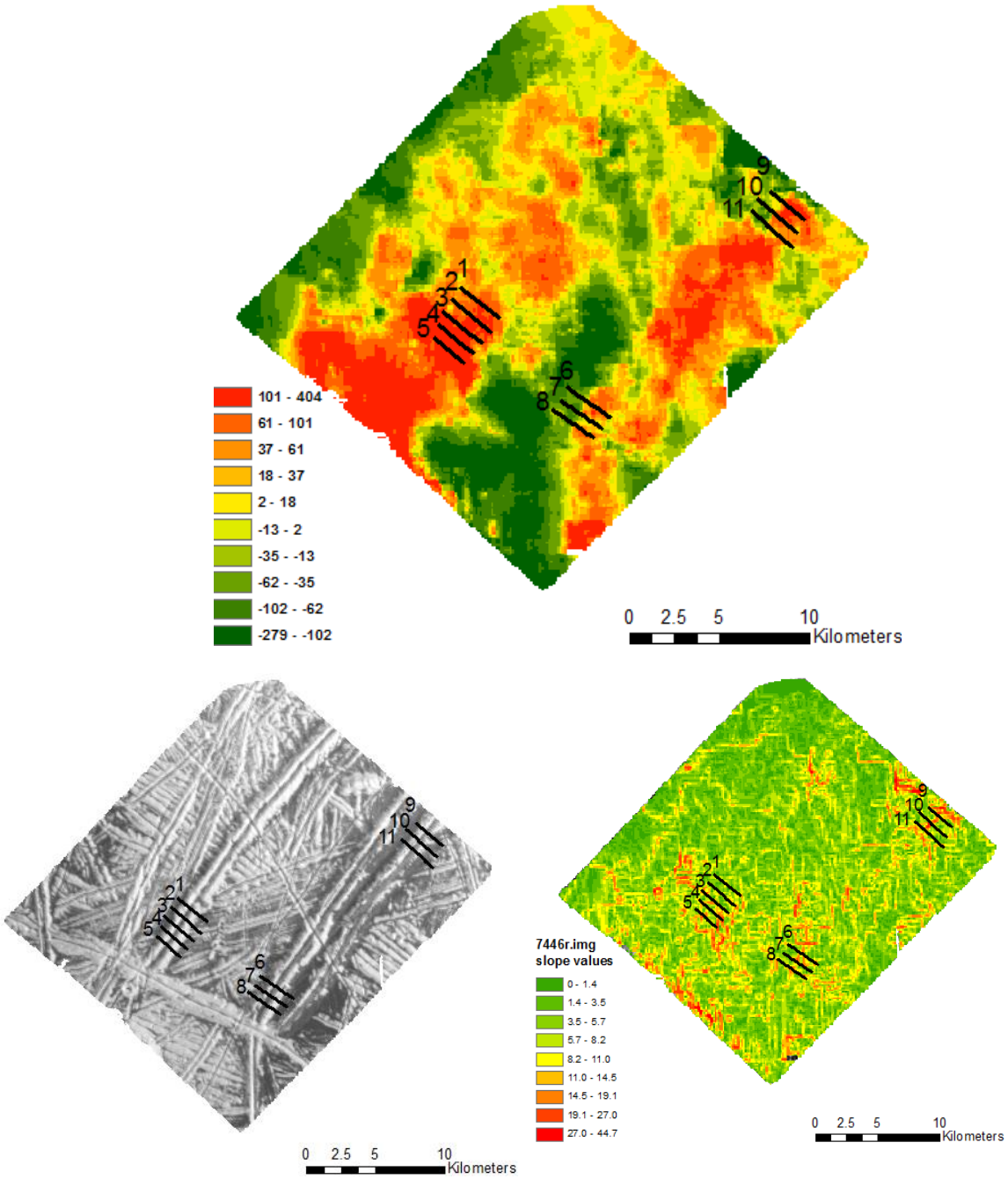

Figure 25. Cilix West region (1.5°N, 183.0°W) ASP DEM (200m resolution) created with higher resolution image 7446r.img (65m/pixel resolution). The Cilix crater is off the image to the northeast. Image 7446r.img was paired with base image 5013r.img (109 m/pixel) to create this DEM. Orthoimage (lower left) and slope map (lower right) included. This ridge is located south of the SOCET-SET DEM 7442r.img.

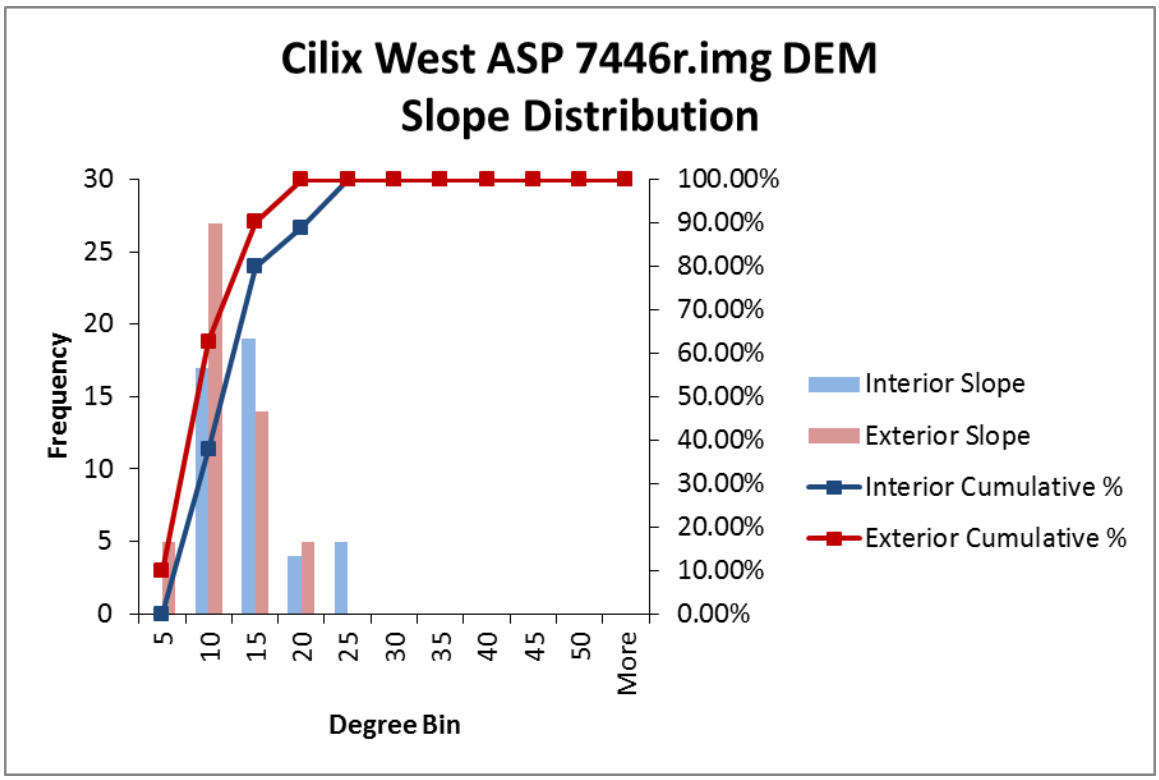

Figure 26. Cilix East ASP 7446r.img DEM slope distribution. A total of 45 interior and 51 exterior slopes are plotted. The exterior slopes appear more evenly distributed, while interior slopes are more concentrated toward lower values. The cumulative frequency for both slope samples is also plotted, with all of the interior slopes and exterior slopes being at or below the AOR.

Cilix East near 2.0°N, 182.0°W: SOCET-SET 7542r.img DEM

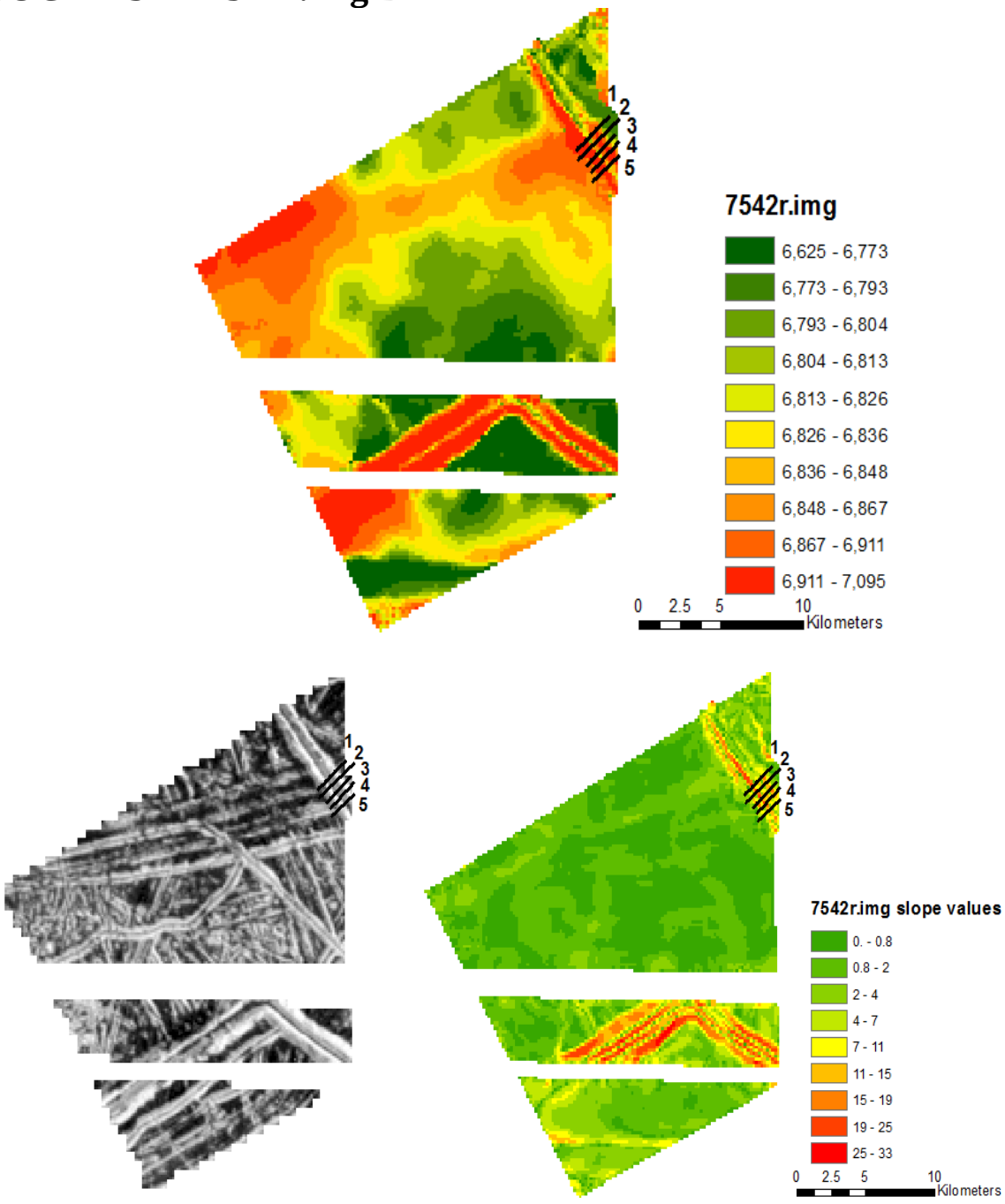

Figure 27. Cilix East region (2.0°N, 182.0°W) SOCET-SET DEM (200m resolution) created with higher resolution image 7542r.img (65m/pixel resolution). The Cilix crater is off the image to the northwest, and the bottom of the image shows the cusp of a cycloid. Image 7542r.img was paired with base image 5013r.img (109 m/pixel) to create this DEM. Orthoimage (lower left) and slope map (lower right) included.

Table 9. Cilix East 7542r.img SOCET-SET DEM slope values for five profile lines. Only exterior slopes (E1 and E2) are reported here, given the lack of sufficient interior points available. The average, standard error (SE), and range are also reported.

	Profile	1	2	3	4	5	Average	SE	Range
1	E2	12.9	13.3	13.4	13.4	13.1	13.2	0.210	0.49
2	E2	14.4	14.9	14.6	14.3	14.5	14.6	0.230	0.62
3	E1	15.0	12.8	13.5	14.9	14.2	14.1	0.934	2.19
	E2	17.4	15.5	15.3	17.7	16.0	16.4	1.082	2.37
4	E1	13.9	14.2	12.8	13.4	13.4	13.5	0.528	1.37
	E2	13.2	13.7	13.8	13.0	13.1	13.4	0.385	0.86
5	E2	8.1	8.7	8.5	8.2	8.5	8.4	0.265	0.63

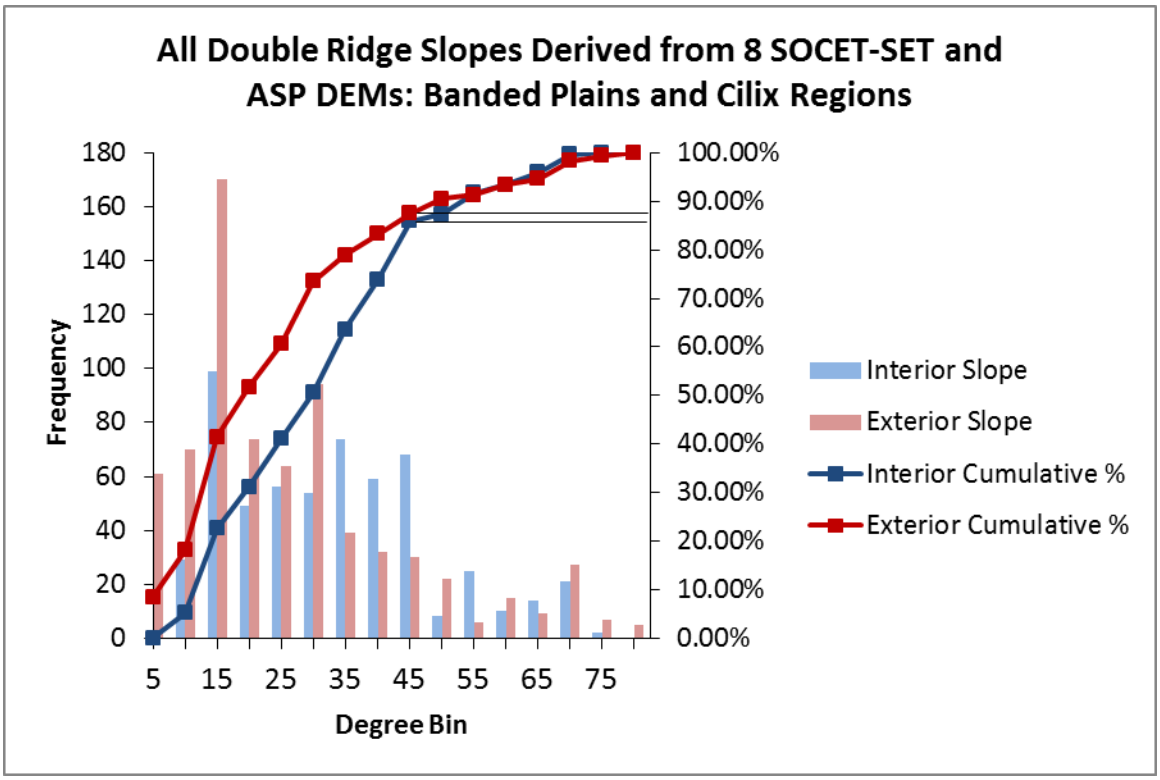

Figure 28. Histogram of slopes derived from both SOCET-SET and ASP DEMs created in this work from the Banded Plains and Cilix regions (8 DEMs in total). A total of 568 interior slopes and 725 exterior slopes are shown in this plot. The interior slope sample appears to be slightly right skewed, favoring shallower slopes, while the exterior slope sample appears to be more right skewed. The cumulative frequency for both slope samples is also plotted, with ~85% of the interior slopes and ~88% of the exterior slopes being at or below the AOR (the positions as shown in the black lines approaching the second y axis).

Table 10. Results from t-tests between exterior and interior slope samples derived from DEMs ($\alpha = 0.05$).

t-Test: Two-Sample Assuming Unequal Variances		
	Exterior	*Interior*
Mean	24.1	30.4
Variance	304	246
Observations	725	568
Hypothesized Mean Difference	0	
t Stat	6.87	
P(T<=t) one-tail	4.901E-12	
t Critical one-tail	1.65	
P(T<=t) two-tail	9.81E-12	
t Critical two-tail	1.97	

Table 11. Results from paired t-tests (2-tail, $\alpha = 0.05$) between interior and exterior slope pairs for each DEM. Included are the number of observations (n), t-test p-value (p), sample means ($\bar{\boldsymbol{\beta}}$) for both interior and exterior, a comparison of the means, and whether or not the two were considered symmetric.

Double Ridge Slope Symmetry: Paired t-tests (2-tail)	**n**	**p**	$\bar{\beta}$ **(interior)**	$\bar{\beta}$ **(exterior)**	**Implies**	**Symmetric?**
2825r.img	9	0.900	11.5	11.4	int. ≈ ext.	**Yes**
2828r.img (upper)	15	2.44 E-5	45.2	25.8	int. > ext.	**No**
2828r.img (lower)	22	0.469	33.4	34.6	int. < ext.	**Yes**
2832r.img	9	0.095	46.0	56.3	int. < ext.	**Yes**
7442r.img	10	0.051	15.4	13.2	int. > ext.	**Yes**

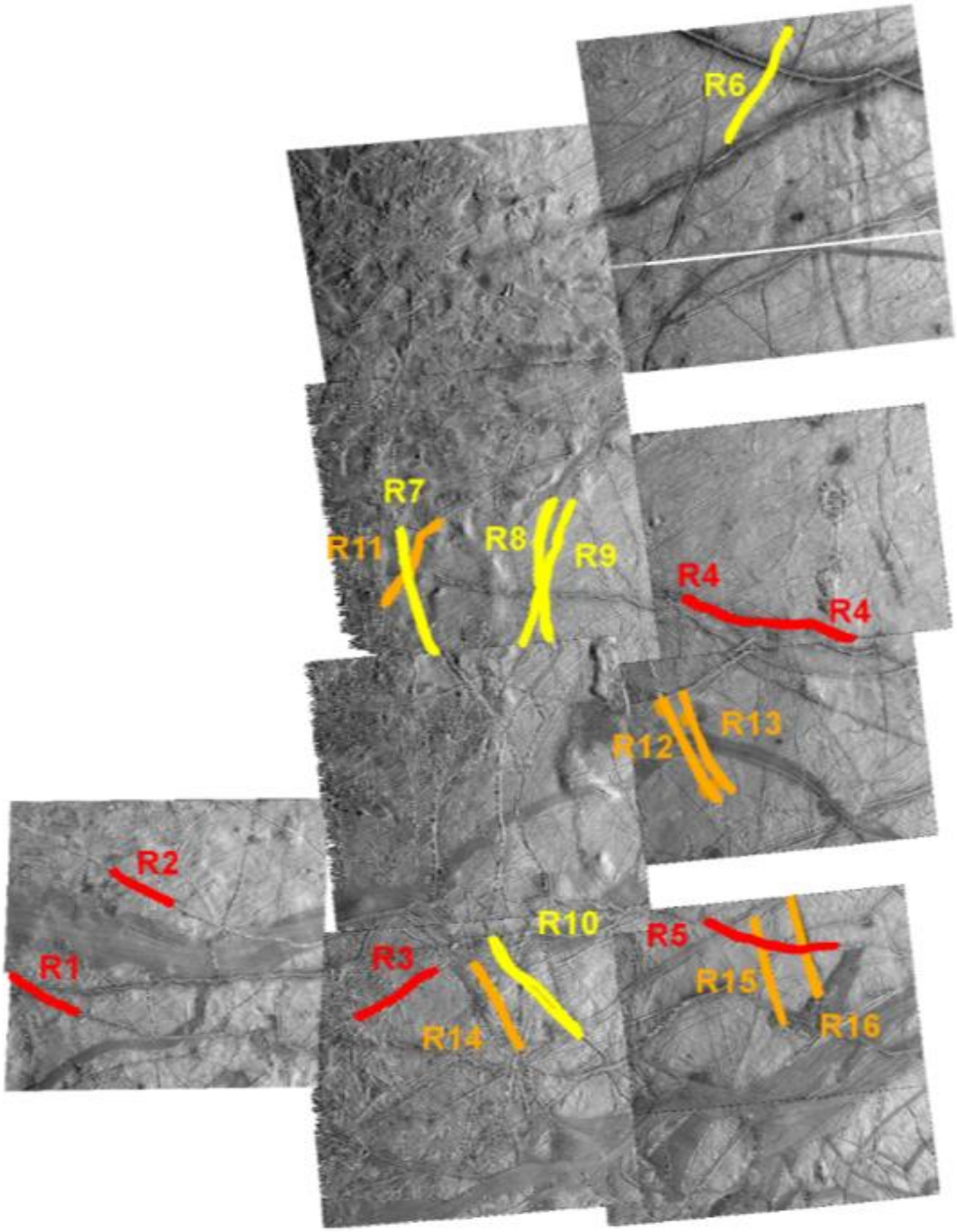

Figure 29. Sixteen ridges examined in this study located in Argadnel Regio, mapped in Figueredo and Greeley (2004), shown with relative ages indicated by color. Proceeding from youngest to oldest, they are designated Pwyllian (red), Annwynian (yellow), and Argadnellian (orange). The images shown are: 4166r.img, 4178r.img, 4552r.img, 4201r.img, 9252r.img, 4565r.img, 4214r.img, 4578r.img, and 4227r.img.

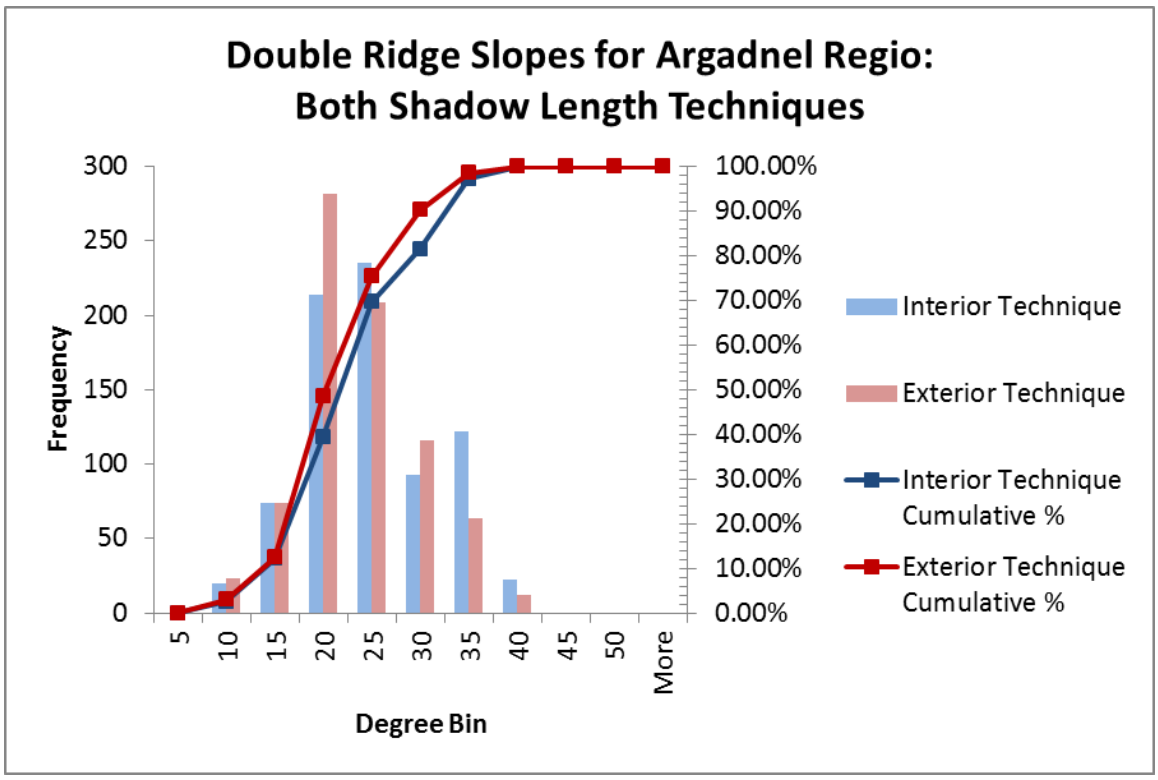

Figure 30. Histogram showing distribution of exterior and interior shadow length technique slopes for Argadnel Regio. Seven-hundred and eighty slopes were derived from both the interior and exterior shadow length techniques in this region. Both appear to be relatively normally distributed. The cumulative frequency for both slope samples is also plotted, with all of the interior slopes and exterior slopes being at or below the AOR.

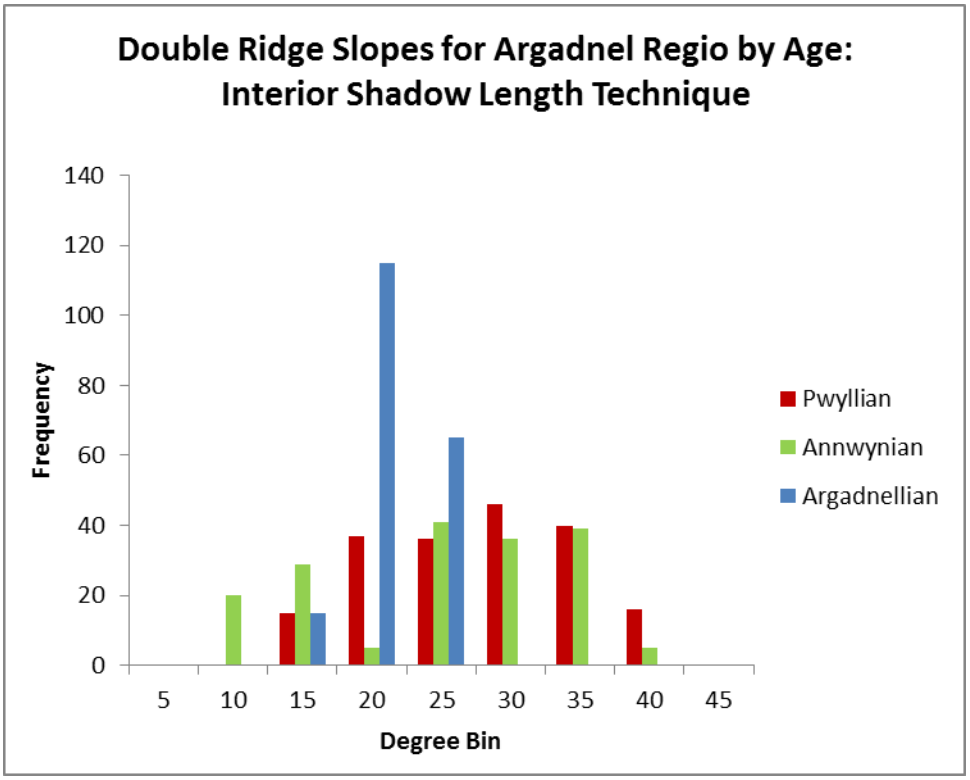

Figure 31. Histograms showing distribution of interior slopes classified by age (proceeding youngest to oldest from Pwyllian, to Annwynian, to Argadnellian) using the interior shadow length technique, with a total of 780 slopes derived.

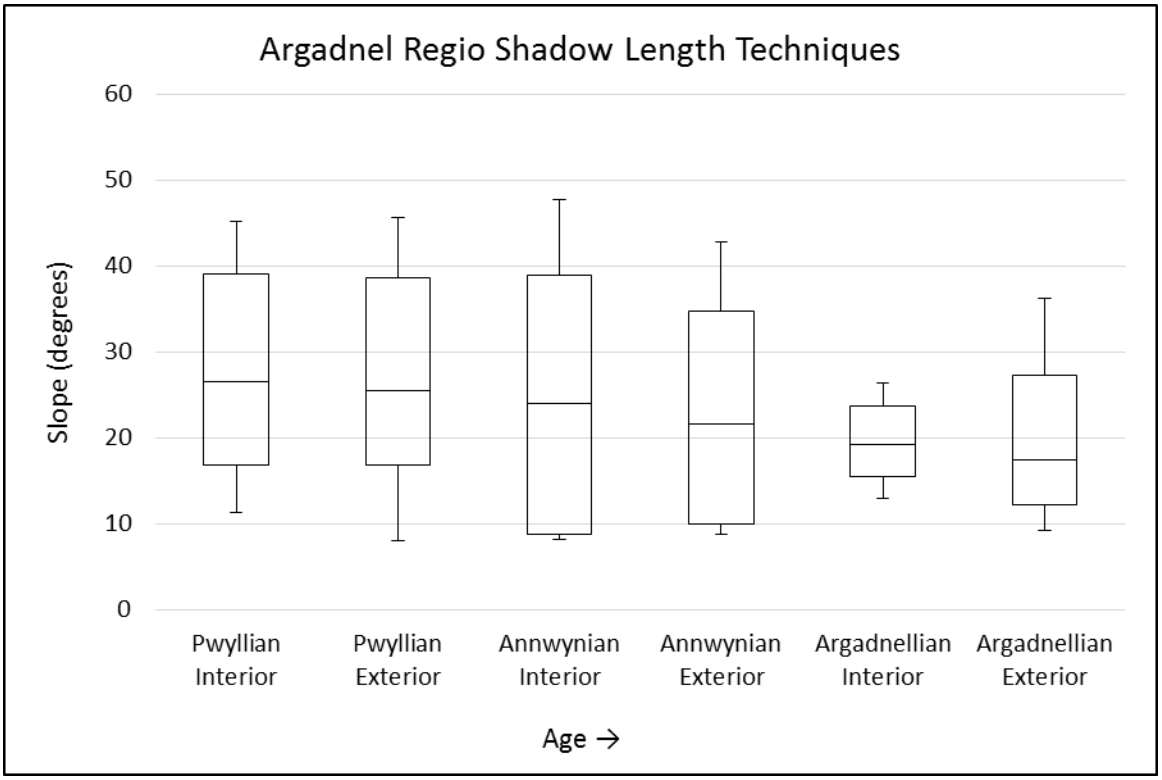

Figure 32. Box plot of Argadnel Regio, showing both the interior shadow length and exterior shadow length techniques distribution for each age group. This plot proceeds from youngest (Pwyllian) to oldest (Argadnellian) from left to right. The upper and lower whiskers represent the maximum and minimum values, while the median value for each age grouping is shown with the black bar in the center of each plot. The boxes represent one sigma (~68%) of the data centered on the mean.

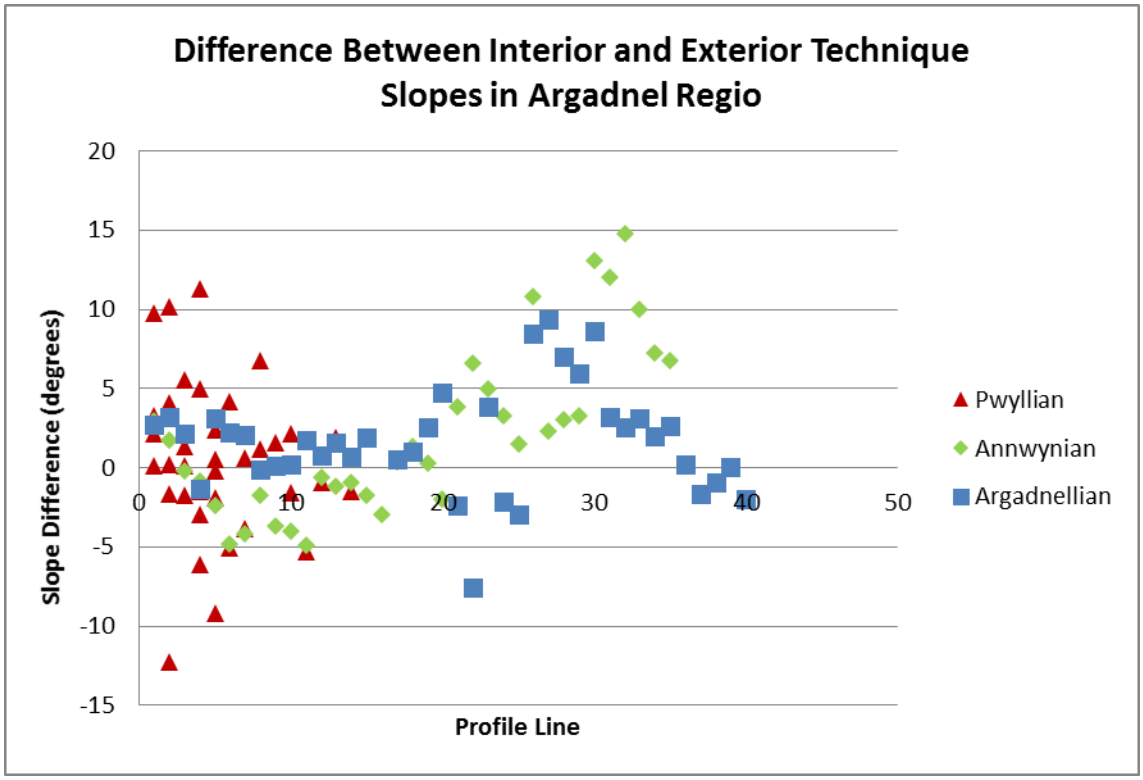

Figure 33. Difference between interior and exterior shadow length techniques in Argadnel Regio for three age groupings. The order in which the profiles are listed along the x axis is arbitrary. Most values in this plot fall within ±5°, suggesting no real preference for either high or low values, or suggesting neither the presence of a significant gap or very superimposed ridge sets.

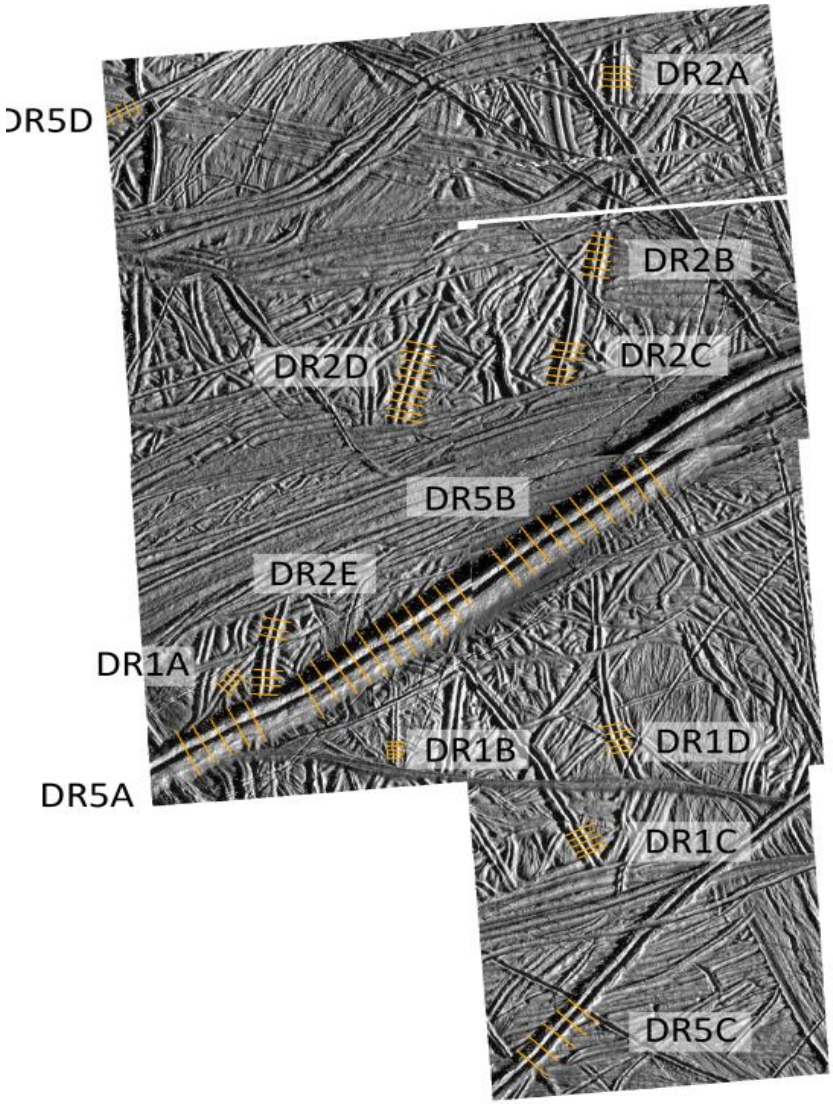

Figure 34. 10 ridges located in Bright Plains Region mapped in Kattenhorn (2002), with individual profile lines drawn on five images: 8639r.img, 8600r.img. 8652r.img, 8613r.img, and 8626r.img. Individual profiles along ridges with defined relative ages are labeled: proceeding from youngest to oldest, they are designated DR5, DR2, and DR1.

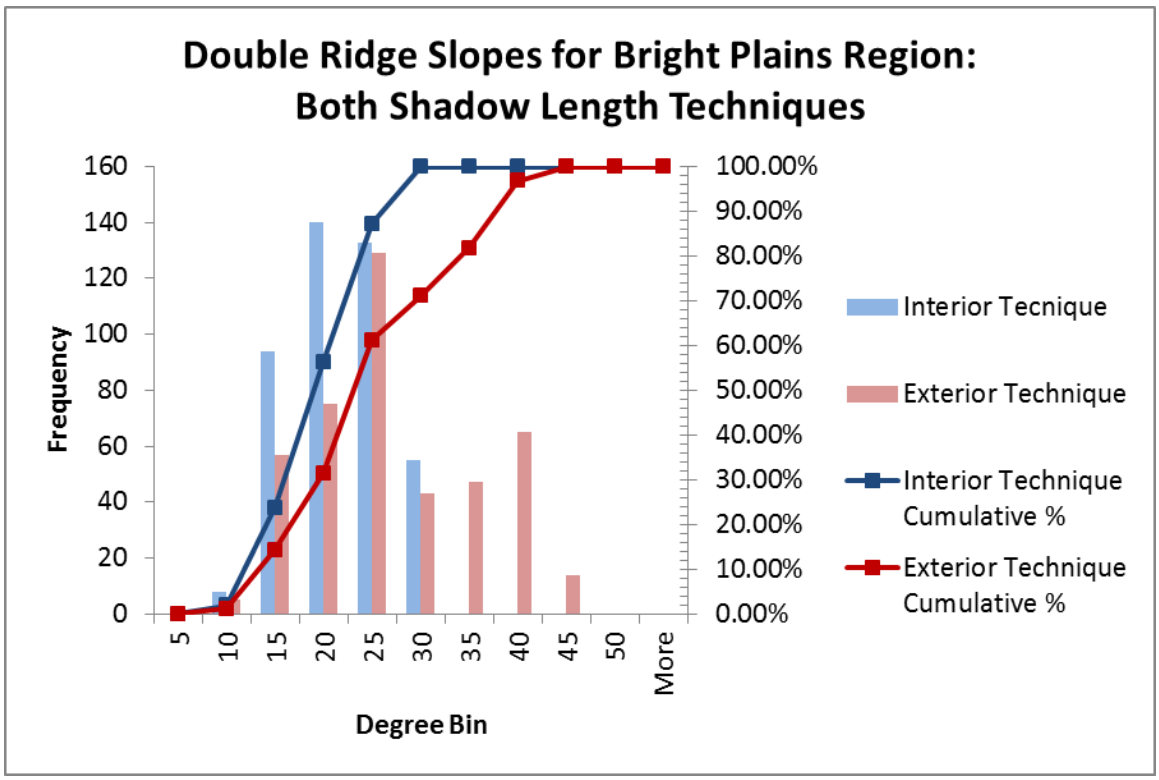

Figure 35. Histograms showing slope distribution of both techniques for the Bright Plains region. 430 slopes were derived from the interior technique, while 435 were derived from the exterior shadow length techniques in this region. The exterior technique slope sample appears to be relatively normally distributed, while the interior technique sample appears slightly right skewed. The cumulative frequency for both slope samples is also plotted, with all of the interior slopes and exterior slopes being at or below the AOR.

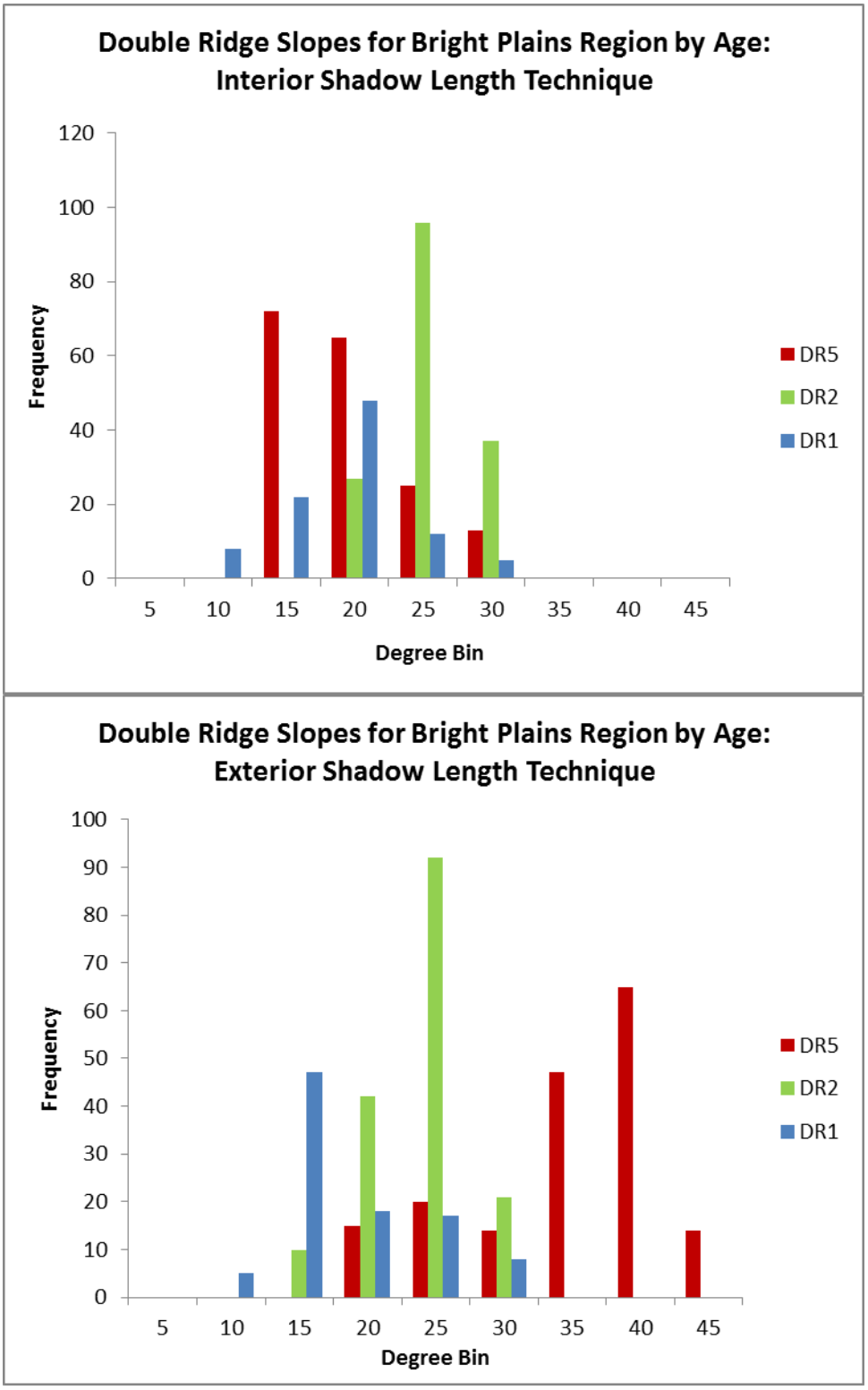

Figure 36. Histograms showing slope distribution of interior (upper) and exterior technique classified by age (lower). DR5 is the youngest time step in this region, followed by DR2, then DR1 as the oldest.

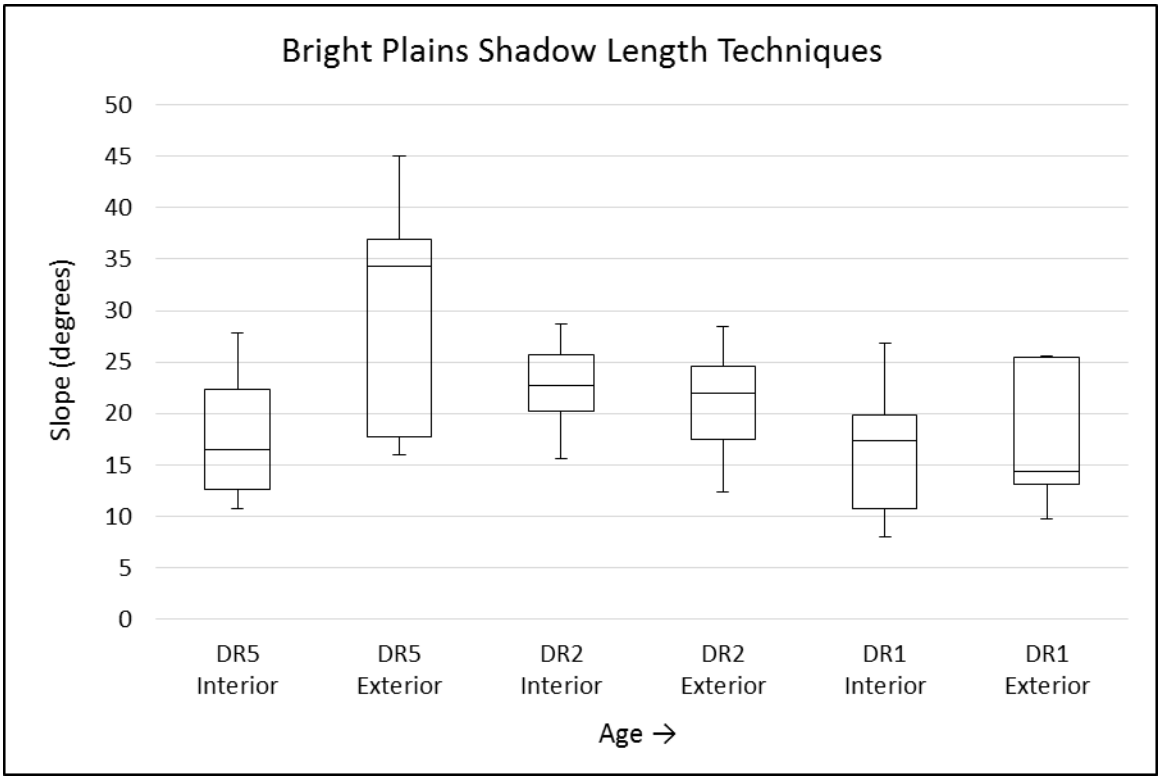

Figure 37. Box plot of Bright Plains region, showing both the interior shadow length (ISL) and exterior shadow length (ESL) distribution for each of the three age groups. This plot proceeds from youngest (DR5) to oldest (DR1) from left to right. The upper and lower whiskers represent the maximum and minimum values, while the median value for each age grouping is shown with the black bar in the center of each plot. The boxes represent one sigma (~68%) of the data centered on the mean..

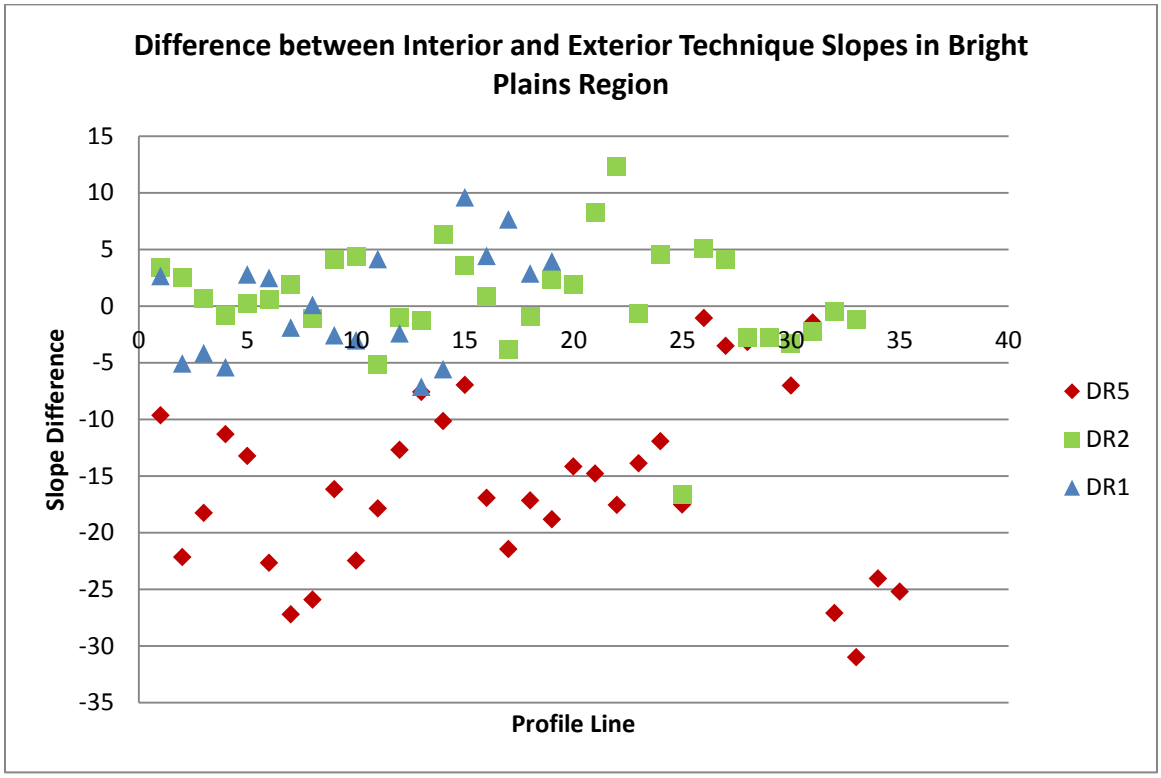

Figure 38. Difference between interior and exterior techniques in Bright Plains Region for three age groupings. Each data point represents the average of five individual slopes along the given profile. DR5 consistently plots below zero, indicating that these youngest ridge sets may be superimposed on one another in their center. Both DR2 and DR1 typically fall within ±5°, suggesting the ridge sets do not have a significant gap between them. .

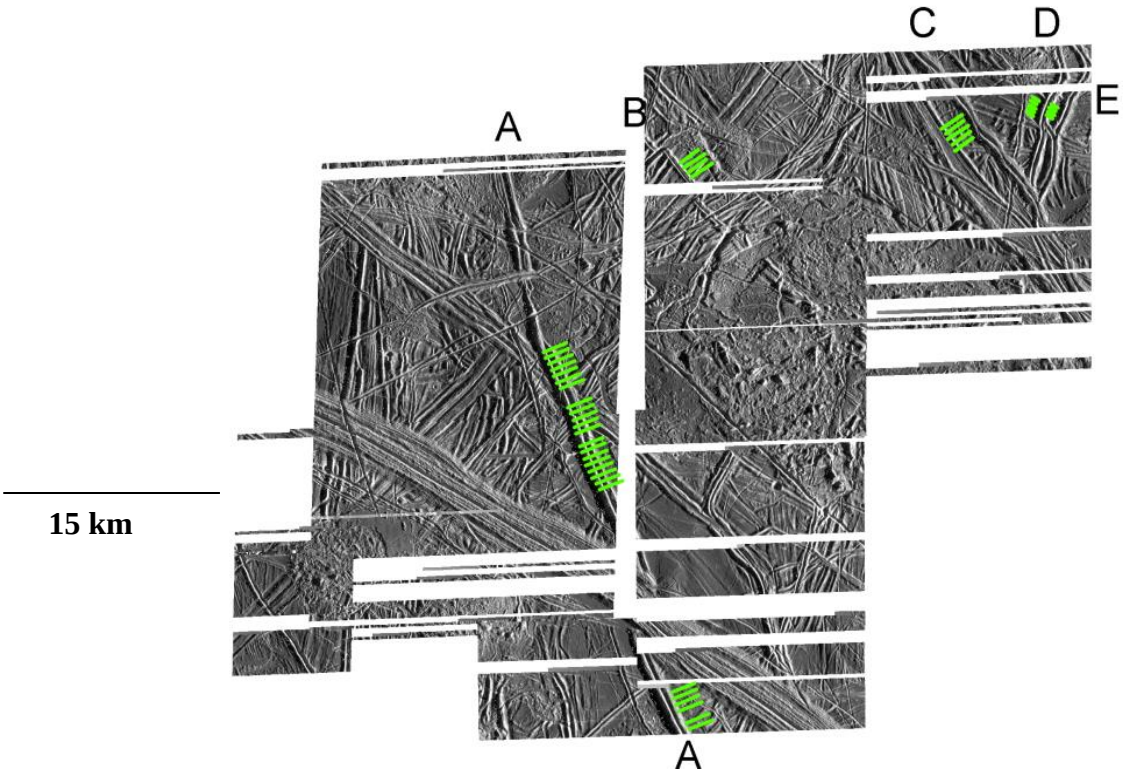

Figure 39. Five ridges located in southern Annwyn Regio, mapped in Spaun et al. (2003), with individual profile lines drawn. Five images are shown: 5413r.img, 5426r.img, 5427r.img, 5439r.img, 5452r.img. Ridge C is determined to be younger than Ridges A, B, D, and E via cross-cutting relationships in this region.

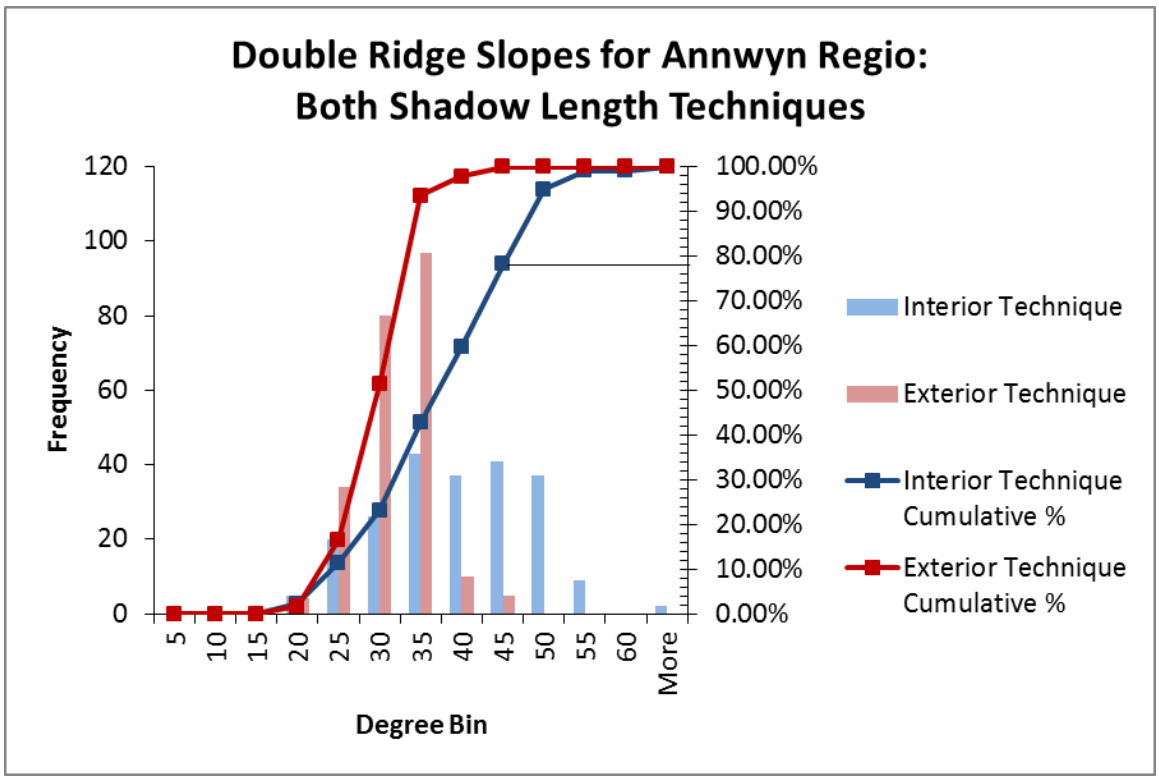

Figure 40. Histogram showing slope distribution of both exterior and interior techniques in southern Annwyn Regio, with 220 slopes derived from the interior shadow length technique and 230 slopes derived from the exterior shadow length technique. Slopes derived from the interior technique appear more normally distributed than those of the exterior shadow length technique, which are more centered around lower values. The cumulative frequency for both slope samples is also plotted, with all of the exterior slopes and ~78% of the interior slopes being at or below the AOR.

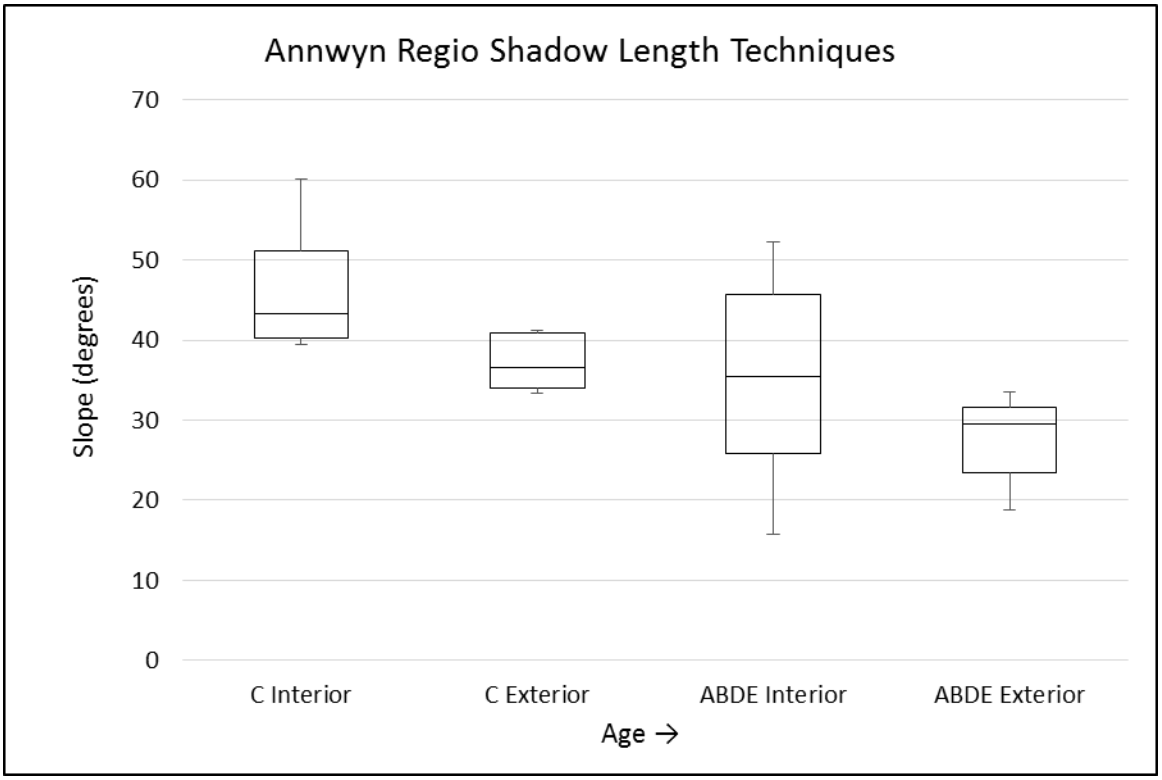

Figure 41. Box plot of southern Annwyn Regio, showing both the interior shadow length and exterior shadow length distribution for each of the three age group. This plot proceeds from youngest (Ridge C) to oldest (Ridges A, B, D, and E) from left to right. The upper and lower whiskers represent the maximum and minimum values, while the median value for each age grouping is shown with the black bar in the center of each plot. The boxes represent one sigma (~68%) of the data centered on the mean.

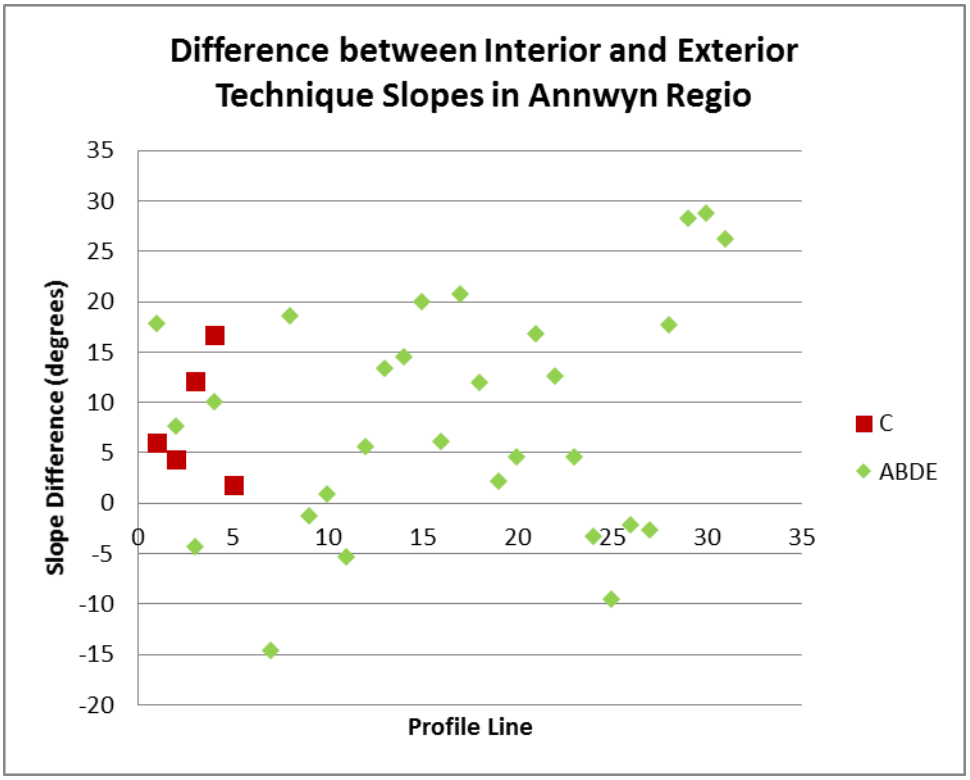

Figure 42. Difference between interior and exterior techniques in southern Annwyn Regio for two age groupings. Each data point represents the average of five individual slopes along the given profile. Fewer data points exist for ridge C for interpretation, the youngest ridge in this area. The majority of the values for both age groupings lie above zero. This indicates a gap existing between the double ridge sets.

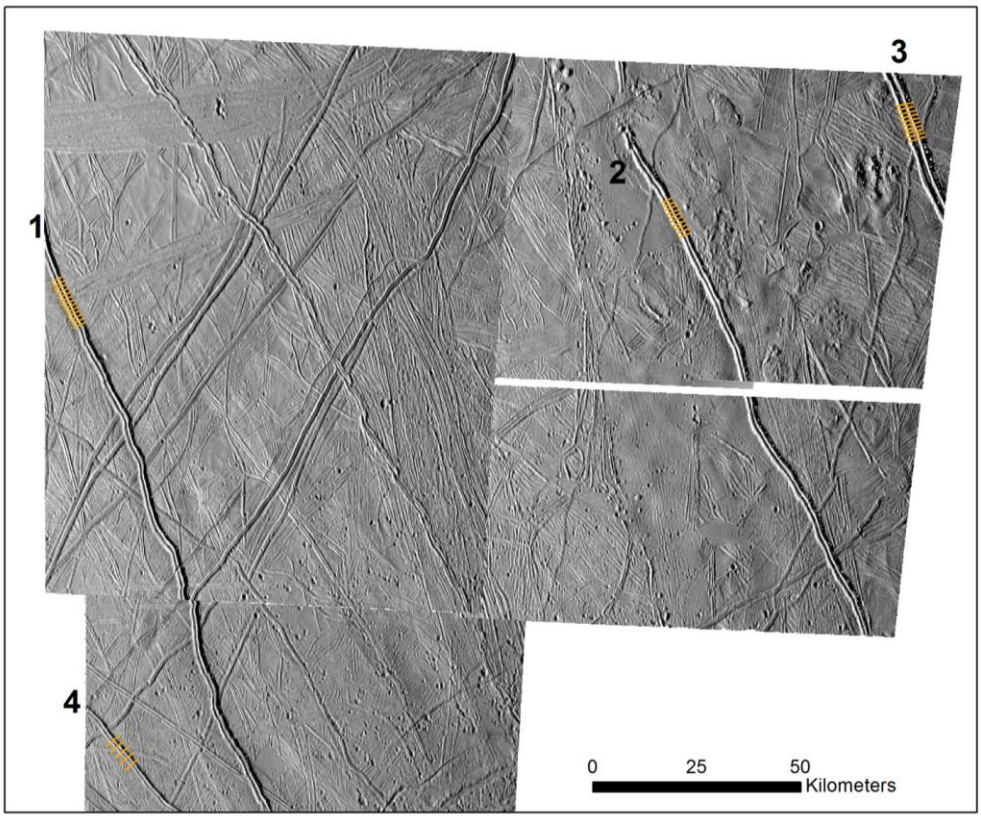

Figure 43. Four ridges in the northern hemisphere that are Pwyllian in age, located on images 3578r.img (upper left), 3600r.img (upper right), and 3626r.img (lower left). Individual profile lines for shadow measurements are drawn.

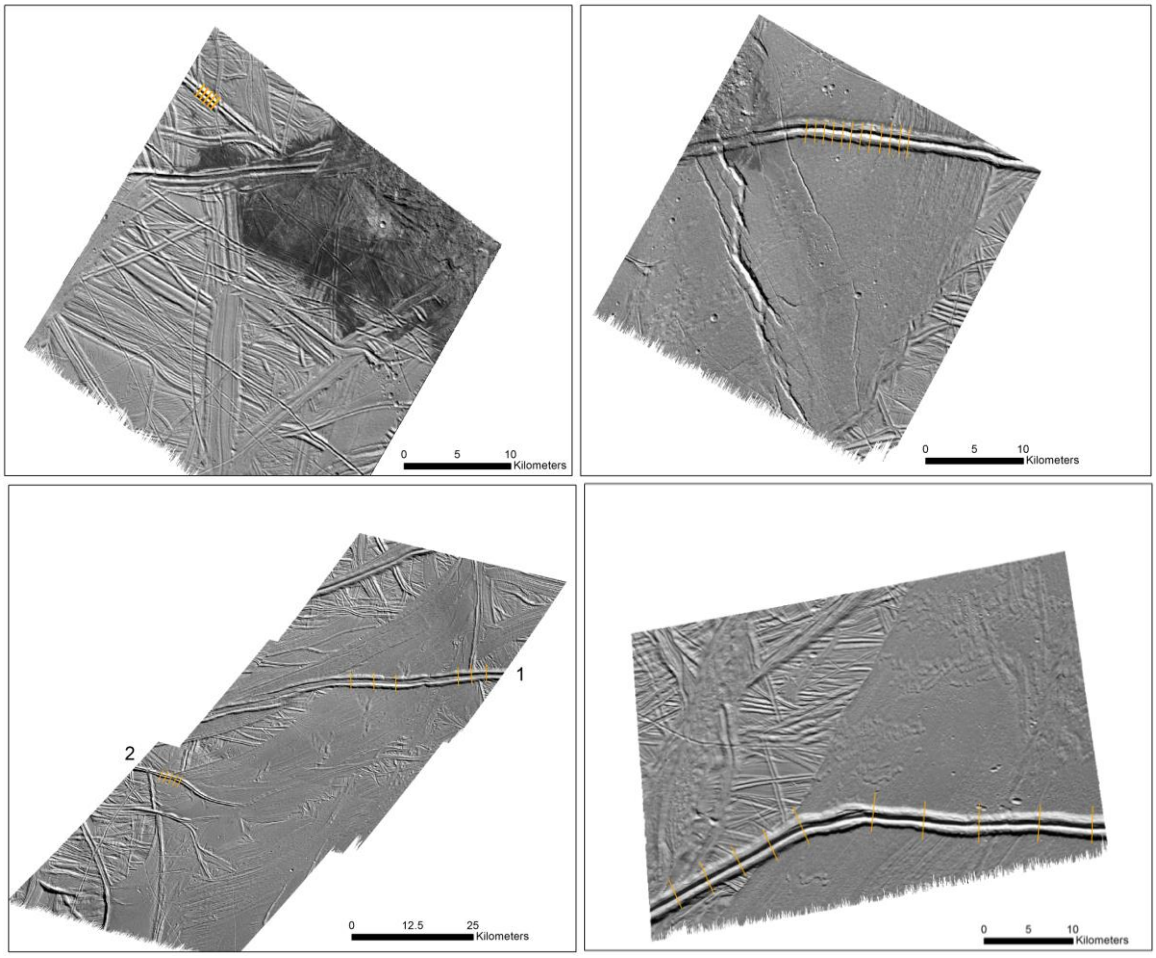

Figure 44. Five ridges in the southern hemisphere that are Pwyllian in age, located on images 9765r.img (upper left), 9939r.img (upper right), 0200r.img and 0178r.img (lower left), and 0526r.img (lower right). Individual profile lines for shadow measurements are drawn.

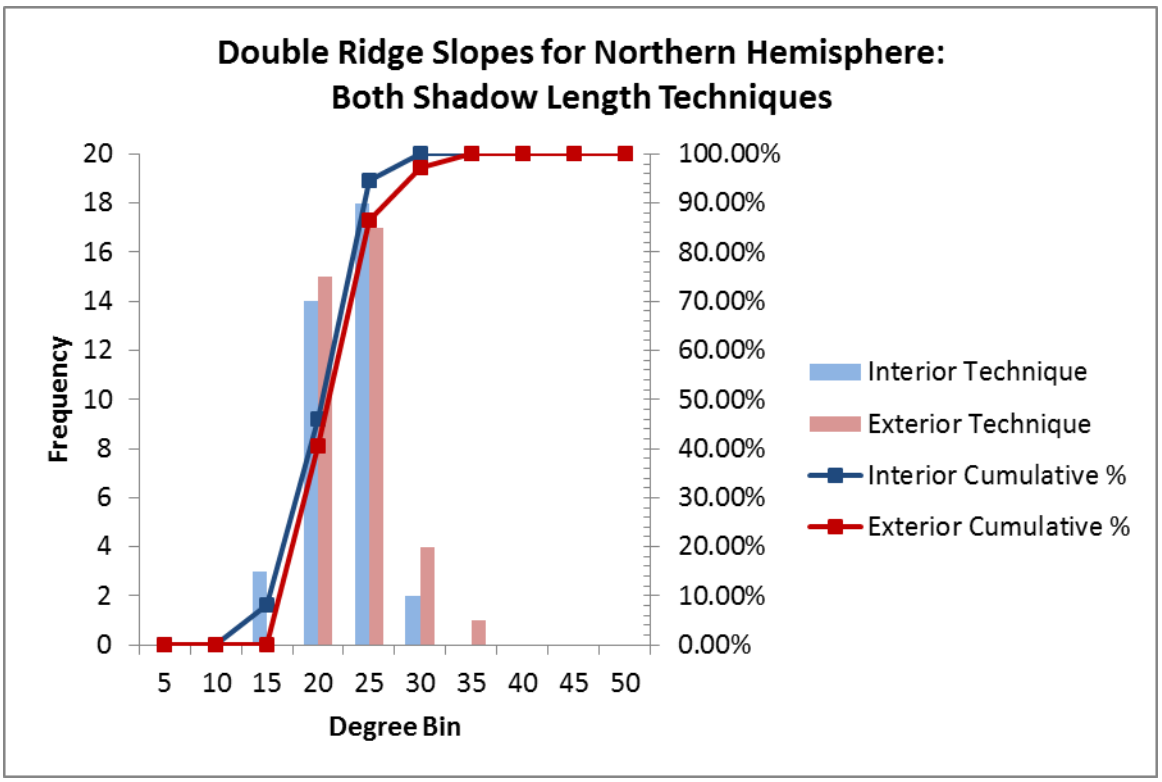

Figure 45. Histogram showing slope distribution of both exterior and interior techniques for Pwyllian ridges in the northern hemisphere, with 37 slopes derived from the interior shadow length technique and 37 slopes derived from the exterior shadow length technique. Slopes derived from the interior technique appear slightly more normally distributed than those of the exterior shadow length technique. The cumulative frequency for both slope samples is also plotted, with all of the interior and exterior slopes being at or below the AOR.

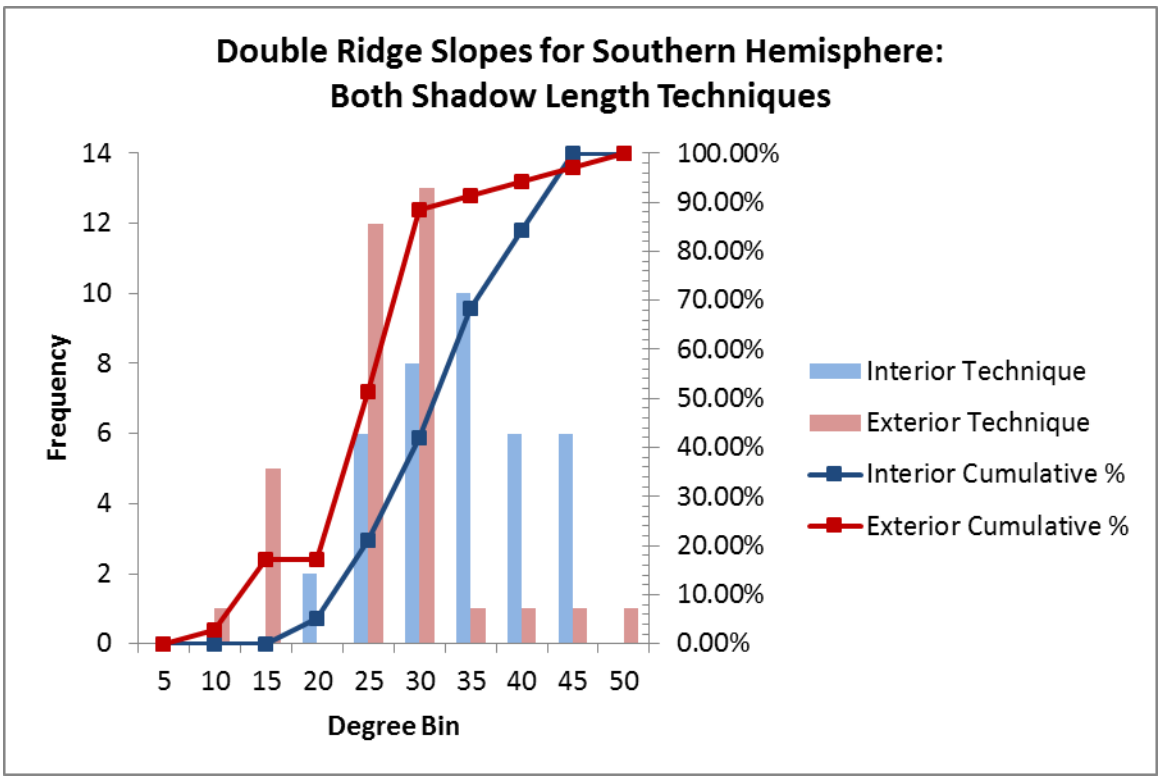

Figure 46. Histogram showing slope distribution of both exterior and interior techniques for Pwyllian ridges in the southern hemisphere, with 38 slopes derived from the interior shadow length technique and 35 slopes derived from the exterior shadow length technique. Slopes derived from the interior technique appear more normally distributed than those of the exterior shadow length technique, which are skewed to the right. The cumulative frequency for both slope samples is also plotted, with all of the interior slopes being at or below the AOR, and only one of the exterior slopes falling above the AOR.

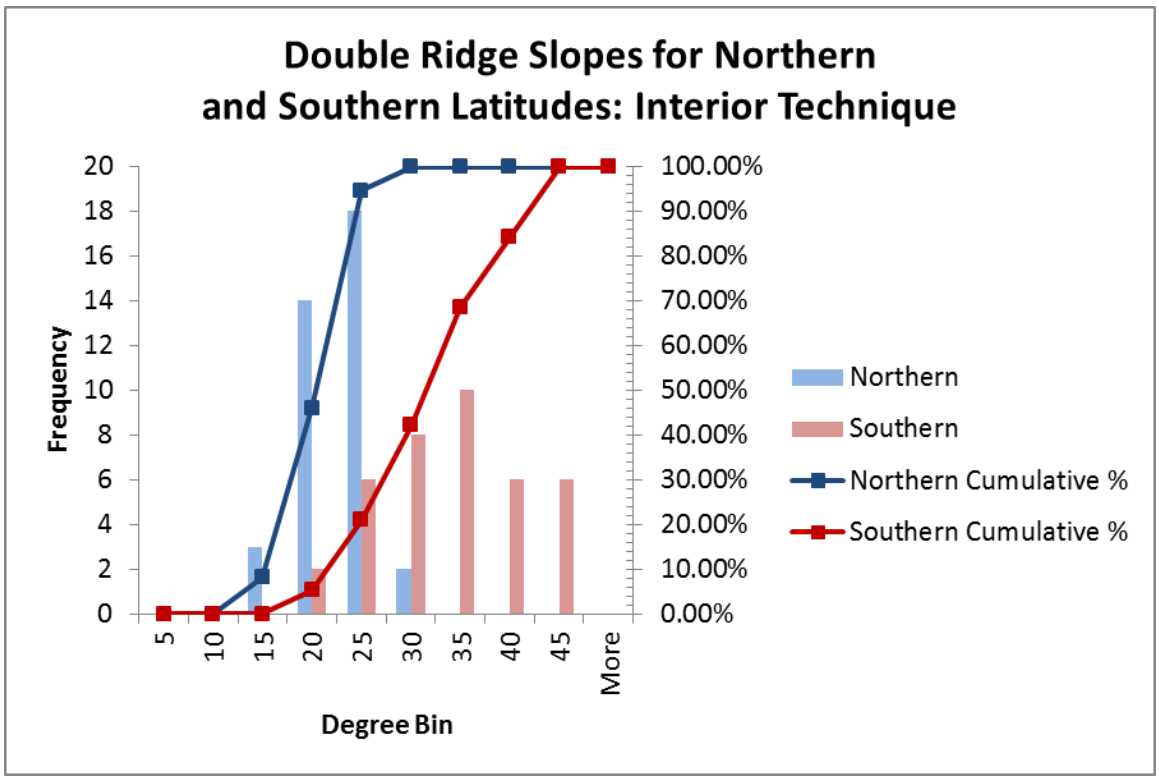

Figure 47. Histograms showing slope distribution of interior shadow length technique for Pwyllian ridges found in northern (N) and southern (S) latitudes. A total of 37 slopes in the north and 38 slopes in the south are plotted here. The slopes are centered around lower values for double ridges in the northern hemisphere compared to those in the south. Those in the southern hemisphere appear normally distributed, while those in the north appear slightly right skewed. The cumulative frequency for both slope samples is also plotted, with all of the interior slopes and exterior slopes being at or below the AOR

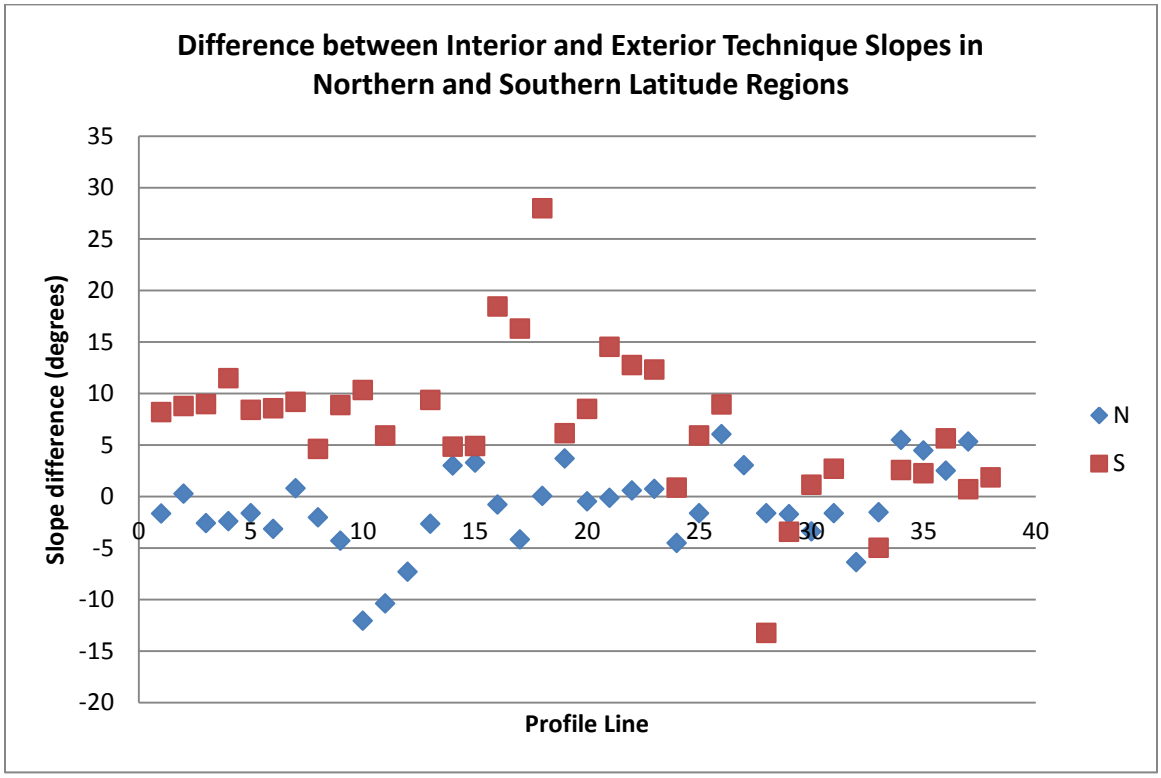

Figure 48. Difference between slope angles derived using the interior and exterior shadow length techniques in northern and southern latitudes. Each data point represents the average of five individual slopes along the given profile. The northern latitude values typically fall between ±5°, suggesting that the ridge sets touch, while the southern ridges plot above zero typically, suggesting the presence of a gap.

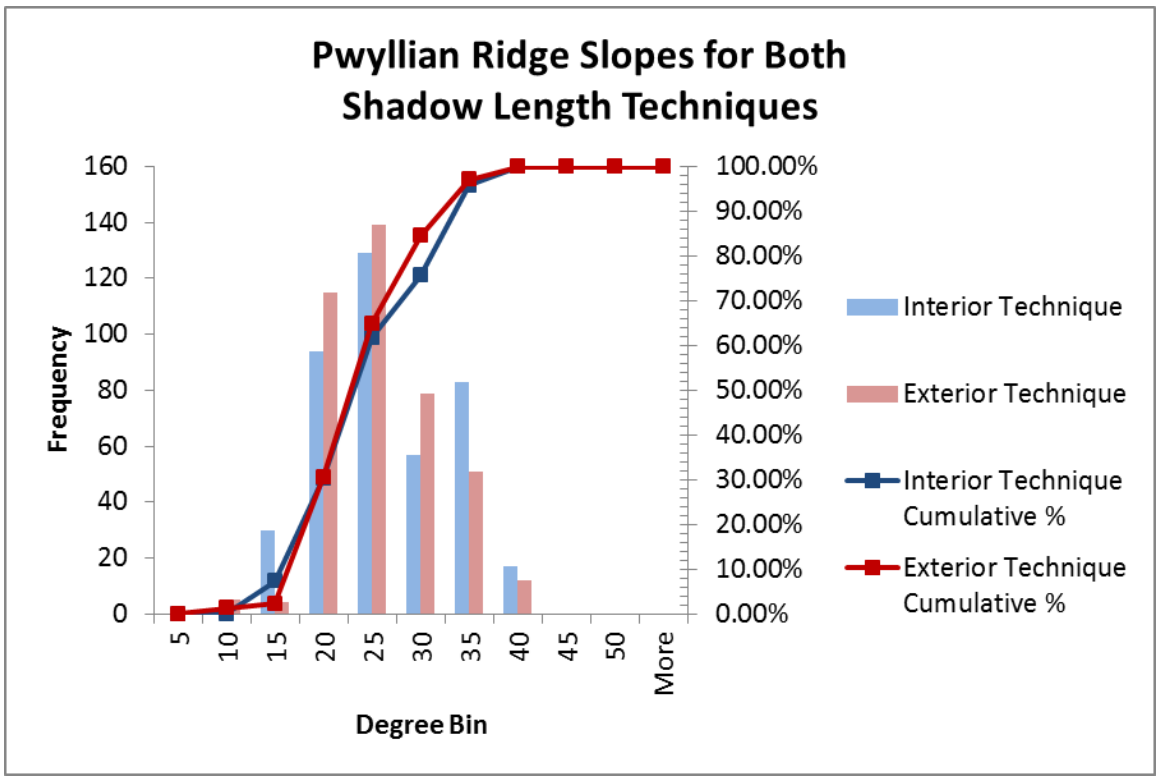

Figure 49. Overall distribution of Pwyllian slopes for both exterior and interior techniques. A total of 410 interior shadow length technique slopes and 405 exterior shadow length technique slopes are plotted here. The interior shadow length technique slopes appear to be more normally distributed than those of the exterior shadow length technique, which are slightly right skewed. The cumulative frequency for both slope samples is also plotted, with all of the interior slopes and exterior slopes being at or below the AOR.

Table 12. Summary of results from interior and exterior shadow measurement techniques for each region.

	All slopes less than AOR?		**Slope decreases with age?**		**Difference plot**
Region	Interior tech.	Exterior tech.	Interior tech.	Exterior tech.	Interior - Exterior is:
Argadnel Regio	Yes	Yes	Yes	Yes	≥ 0
Bright Plains	Yes	Yes	No[2]	Yes	≈ 0 [3]
Annwyn Regio	No[1]	Yes	Yes	Yes	> 0
N. Hemisphere	Yes	Yes	n/a	n/a	≈ 0
S. Hemisphere	Yes	Yes	n/a	n/a	> 0

[1]Along a single ridge, with two outliers being near 60°
[2]DR2, the middle time step, gives steepest slope values
[3]With the exception of DR5, which is typically < 0.

Vita

Ashley Dameron was born in Springfield, Missouri, to parents Jack and Carol Dameron. She is the youngest of four siblings: Troy, Jason, and Sarah. She attended Disney Elementary School, Cherokee Middle School, and Kickapoo High School in Springfield. Ashley first became interested in studying Europa after taking an Earth science class in high school. She then presented a science fair project investigating the thickness of Europa's icy crust at the Ozarks Science and Engineering Fair in April of 2008. Her research project was selected as the first alternate for the Intel International Science and Engineering Fair. After graduating high school, she continued her education at Missouri State University, where she obtained a Bachelor of Science degree in December of 2012, majoring in geology with a minor in mathematics. She graduated from Missouri State cum laude, in the Honors College. She accepted a graduate teaching assistantship at the University of Tennessee, Knoxville, in the Earth and Planetary Sciences Department. Ashley graduated with a Master of Science degree in geology in August of 2015. She plans to continue working with planetary images to investigate other interesting surface features of Earth and other solar system bodies.